

MODELING ATRIAL FIBRILLATION
EXPLORING THE KOIVUMÄKI
HUMAN ATRIAL CELL MODEL

by

Jonas van den Brink

THESIS
for the degree of
MASTER OF SCIENCE



Faculty of Mathematics and Natural Sciences
University of Oslo

May 2016

Abstract

In this thesis, we offer a detailed description of the Koivumäki model, a computational model for the electrophysiology of the human atrial cardiomyocyte. The model is examined to see to what extent it exhibits cardiac alternans, an important dynamical substrate for atrial fibrillation. We show that the Koivumäki model reproduces calcium-driven alternans through refractoriness of ryanodine receptor release channels. We observe large differences in alternans behavior between the 2014 and 2015 formulations of the model, and show that these differences can partly be attributed to different formulations of the L-type calcium current in the two model variants, especially so for the maximal L-type channel conductance.

In addition, we give a review of four proposed models for cardiac myofibroblasts. We use the Maleckar model for the human atrial fibroblast to extend the Koivumäki model to include fibroblast-myocyte coupling. The effects of the coupling on the virtual Koivumäki myocyte are examined as the coupling strength and number of fibroblasts are varied. We show that fibroblast-myocyte coupling leads to significant changes in the myocyte action potential, which we attribute mainly to a depolarization of myocyte resting membrane potential. Action potential amplitude and upstroke velocity are both reduced, following fibroblast-myocyte coupling. We show this to be caused by decreased availability of fast inward sodium current due to depolarized resting potential of the myocyte. We see a close-to-linear decrease in action potential amplitude and upstroke velocity of the action potential with increasing RMP, up until the point where the myocyte fails to excite entirely.

Having explored the cardiac alternans behavior of the model, as well as extending it to include fibroblast-myocyte coupling, will be helpful for further development and use of the model in atrial fibrillation research.

Acknowledgements

This thesis marks the end of six years at the University of Oslo for me. I have learned more here than I ever thought it was possible to know. And not only about math, informatics and physics, but more importantly about myself and everything else in life. I have made great friends here, and it will be with a heavy heart that I leave my office at the physics building of UiO.

During my undergraduate years, I spent much of my time at Lille Fysiske Lesesal, and I want to thank everyone who helped make it such a great place. I must especially mention, and thank, Anders Lauvland, for all the tip-top collaborations on coursework, fantastic discussions, and some exceptional parties in Tøyengata.

My last three years at UiO have been based at the Computational Physics group. My time at Comp Phys has been excellent thanks to wonderful students and professors. I especially want to thank my officemates, first Øydis Larsen and Mathilde Kamperud, and later Wilhelm Holmen and Marte Julie Sætra—you have all provided exceptional help and comradeship.

I want to express gratitude to everyone at Simula who I have worked with over the last five years, especially Molly Maleckar, who first introduced me to cardiac modeling and who has been the main advisor for this thesis. She has been encouraging, supportive and helpful from the very start. I also want to thank Lena Korsnes and Andy Edwards for all the assistance they have provided over the last couple of years, and for terrific times shared in both Oslo and San Diego.

A big thanks to Jussi Koivumäki for sharing his code and for first-class advice and feedback.

Outside of coursework and work, I want to thank my family for all the help they have provided and for all the work they have put into our brewery, while I have worked on this thesis. Also, a big appreciation to my team, Missed Trigger Gaming, who have provided a nice distraction from work when it all got a bit too much.

Finally, Emilie Fjørner, thank you for all your advice, support, and for always being there for me.

Oslo, May 2016
Jonas van den Brink

Contents

1	Introduction	1
2	Motivation	5
2.1	What is AF and Why Does it Matter?	5
2.2	Using Mathematical Models	8
2.3	Ethical Concerns	8
3	Cardiac Physiology	11
3.1	Structure and Function	11
3.2	Cardiac Myocytes	14
3.3	The Nernst-Planck Equation	15
3.4	The Action Potential	18
3.5	Intracellular Calcium Dynamics	19
3.6	Activation of the Myocardium	21
3.7	Reentry and Fibrillation	22
3.8	Cardiac Alternans	26
3.8.1	Restitution-driven Alternans	28
3.8.2	Calcium-driven Alternans	29
3.8.3	Bidirectional $V \leftrightarrow \text{Ca}^{2+}$ Coupling	30
4	Conductance-based Models	33
4.1	The Hodgkin-Huxley Model	33
4.2	Models for the Human Atrial Myocyte	37
4.3	Alternans in hAM Models	39
5	The Koivumäki Model	43
5.1	Cell Geometry	44
5.2	Membrane Currents	46
5.3	Intracellular calcium dynamics	58
5.3.1	The SERCA Pump	58
5.3.2	Ryanodine Receptor Release Channel	60
5.3.3	Calcium Buffering and Diffusion	62

5.3.4	Time Evolution of SR Calcium Concentration	65
5.3.5	Time Evolution of Bulk Cytosolic Calcium	67
5.4	Time Evolution of Ionic Concentrations	69
6	Modeling Fibroblast-Myocyte Coupling	71
6.1	Fibroblasts	71
6.2	The Gap Junction Current	72
6.3	Fibroblast Models	75
7	Solving the Model	83
7.1	Solving Initial Value Problems	83
7.2	Implementation	86
7.3	Verification	91
7.3.1	Test case: Exponential decay	91
7.3.2	Test case: Hodgkin-Huxley model	93
8	Simulation Protocols	95
8.1	Alternans in the Koivumäki model	95
8.1.1	Dynamic Restitution	95
8.1.2	Exploring Alternans Mechanisms	96
8.1.3	Model Differences	98
8.2	Fibroblast-Myocyte Coupling	99
9	Results	103
9.1	Alternans in the Koivumäki Model	103
9.1.1	Model Differences	111
9.2	Effects of Fibroblast-Myocyte Coupling	117
9.2.1	Action Potential Morphology	117
9.2.2	Reduced Sodium Channel Availability	117
9.2.3	Myocyte Excitability	120
10	Discussion	125
10.1	Alternans Behavior of the Koivumäki Model	125
10.1.1	Mechanisms of the K2015	125
10.1.2	Mechanisms of the K2014	127
10.1.3	Model differences	129
10.2	Fibroblast-Myocyte Coupling	130
10.3	Limitations of the Work	132
10.4	Possibilities of Further Work	133
11	Concluding Remarks	135
12	Bibliography	137

Chapter 1

Introduction

Atrial fibrillation is a common form of arrhythmia, which means an irregular heart rate. It is a highly complex condition and much research is devoted to understanding the underlying mechanisms and how to treat it. Atrial fibrillation has been identified as one of the biggest health problems in Western countries, leading to a significant increase in health care costs as well as deaths ([[Zoni-Berisso et al., 2014](#)]).

Research on atrial fibrillation, and cardiac research in general, is challenging and multidisciplinary. One of many important tools in the search for novel insight into cardiac systems is mathematical and computational modeling. Modeling of the human atria have progressed vastly over the last 15 years ([[Dössel et al., 2012](#)]), and different approaches have been used to both understand the underlying causes of atrial fibrillation, as well as aid in the development of new treatment, which is summarized in [[Trayanova, 2014](#)].

Modeling the heart is also a multi-scale problem. The fundamental functional unit of the heart is the myocyte, or muscle cell, which is roughly $100 \times 10 \times 10 \mu\text{m}$ in size. Understanding how individual myocytes work is important to seeing how they combine to form the cardiac tissue. Understanding how the tissue works is important to understanding how the heart functions as a complete organ. In this thesis we will work at the cell-level, meaning we try to model the behavior of a single cardiac muscle cell.

The long-term aim of this field of research is to further understanding of atrial fibrillation and develop novel treatment options. In this thesis we work with a model of a single human atrial myocyte, which is only a small piece of the big effort that is modelling atrial fibrillation. Currently there are five such computational models that are used in the literature. We select and work with one of these models, the model proposed in [[Koivumäki et al., 2011](#)]. Our aim is to explore and understand the model, with the goal of helping further development

and use of the model.

Cardiac cells feature a behavior known as alternans, where consecutive heartbeats varies between weak and strong, despite a constant heart rate. It is hypothesized that cardiac alternans are a functional substrate for atrial fibrillation ([[Narayan et al., 2011](#)]). We will look at the extent to which the model produces this behavior and the underlying mechanisms by which alternans arise. In addition, we will extend the model to include effects of myocytes coupling to neighboring support cells known as fibroblasts, which has also been hypothesized to be linked to atrial fibrillation ([[Nguyen et al., 2014](#)]).

Another aim of the thesis is to give the reader an overview of cardiac modeling and a review of modeling atrial fibrillation. We therefore start of by discussing cardiac modeling in the broader scope of atrial fibrillation before focusing more in detail specifically on our selected cell model.

Goals of the Work

We divide the goals of the work into three categories.

The first category is literature review, where we aim to give the reader a succinct overview of

- The current scientific understanding of atrial fibrillation
- How the electrophysiology of a cardiomyocyte is modeled
- Different models for the human atrial myocyte
- Different models for the human atrial fibroblast

In addition, we want to give a detailed description of the most recent formulation of the Koivumäki model, as this is not presented in a single location in the literature, but is rather spread out across a number of different articles and their supplementary materials.

The second category is implementation, where we aim to

- Implement both the 2014 and 2015 formulations of the Koivumäki model
- Extend the Koivumäki model to include the effects of fibroblast-myocyte coupling
- Create a framework for solving the model and efficiently defining and running simulations

Finally, we have computational studies, where we aim to

- Look at the extent to which the 2014/2015 variants of the Koivumäki model exhibit alternans
- Understand the underlying mechanism of alternans in the model
- Understand the difference between the two variants, if any
- Study the effects of fibroblast-myocyte coupling on the Koivumäki myocyte model

Chapter Outline

The structure of this thesis is set up so that someone with little to no experience with physiology or cardiac modeling can read it from cover to cover.

Chapter 2 covers the motivation of the research and gives a short introduction to what atrial fibrillation is and why it is important.

Chapter 3 gives a short introduction to the structure and physiology of the heart. While this thesis focuses mostly on single cardiomyocytes, having some working knowledge of both the tissue and organ as a whole is important to understand the larger context of the work. Mostly electrophysiological properties are covered, as these are the most important for the topic.

Chapter 4 gives an introduction to the Hodgkin-Huxley model, which was the first example of a conductance-based model of an excitable cell. This model is of a nerve cell and is much simpler than the model we will end up using—it is meant as a manageable introduction to readers not familiar with electrophysiology. Next we give a short review of the historic development of cell models moving from the Hodgkin-Huxley model in 1952 to the cardiac models of today. The Chapter is finished by discussing the five current models for the human atrial myocyte.

Chapter 5 goes into detail on the Koivumäki model and contains the entire mathematical formulation of the model, as well as tables of parameters.

Chapter 7 covers how the model has been implemented and solved computationally. We also cover how the implementation has been tested and verified.

Chapter 8 will outline how the model has been used in virtual experiments. Descriptions of the exact simulation protocols used are outlined.

Chapter 9 gives the results of our simulations, Chapter 10 discuss the results, and Chapter 11 contains concluding remarks.

Chapter 2

Motivation

2.1 What is AF and Why Does it Matter?

Atrial fibrillation (AF) is a form of cardiac arrhythmia, a medical condition leading to an irregular heart rate. Cardiac contraction is caused by an electrical impulse traveling through the tissue like a wave, leading the muscle fibers of a healthy heart to contract in a coordinated regular pattern. In AF, this wave of electrical impulse has become chaotic and turbulent. This means the contraction of individual muscle fibers have become uncoordinated, causing the atrial chambers to quiver more than contract: they *fibrillate*.

Atrial fibrillation rarely requires immediate medical attention and can in some cases be asymptomatic ([American Heart Association, 2016]). It is, however, associated with a clear risk over time. AF patients have been found to be at a five-fold higher risk of stroke than the general population, and at a two-fold higher risk of death ([Zoni-Berisso et al., 2014]).

Atrial fibrillation can be a sustained arrhythmia, meaning it is stable over longer periods in a patient. The duration of a specific AF episode can vary drastically between patients, medical practitioners therefore divide patients into three groups:

- **Paroxysmal fibrillation** is used for patients who experience episodes lasting less than 7 days. Within this time the heart rate usually returns to normal rhythm on its own.
- **Persistent fibrillation** is used for patients who experience episodes lasting more than 7 days. The heart rate will usually *not* return to normal without medical intervention in the form of medication or *electrical cardioversion*, the use of directed electrical shocks to reset the hearts' natural electric

activity.

- **Permanent fibrillation** is used for patients who experience episodes that last indefinitely. Medical intervention is usually unsuccessful in reverting the heart rhythm or the patient relapses shortly after intervention.

How often patients experience AF episodes also varies drastically—but it is a general trend that both the frequency and duration of AF episodes increase over time. Paroxysmal AF often leads to persistent and eventually permanent AF.

This progressive worsening of AF has been explained by the cardiac tissue undergoing remodeling and fundamentally changing as a result of AF, leading to a tissue that seems more vulnerable to new episodes of AF. This hypothesis was strongly supported by an experimental study by [Wijffels et al., 1995]. By artificially inducing episodes of AF in goats before reverting them to a normal heart rhythm, they found that both the ease of induction and duration of the episodes themselves increased as the goats experienced more AF. The article presenting their results was named: “*Atrial Fibrillation Begets Atrial Fibrillation.*”—which quickly became a much quoted truth in our understanding of AF and its treatment.

Prevalence of AF

[Zoni-Berisso et al., 2014] estimates that 2 % of the general population in Europe currently suffer from AF. They also predict that the proportion of the population with AF will grow towards 2050, primarily due to an aging population, but also a better ability to treat other chronic diseases. [Naghavi et al., 2015], reported that annual deaths due to AF and atrial flutter (a medical condition closely linked to AF) have increased drastically, estimating 29 000 deaths globally in 1990, while in 2013 it had risen to 112 000 deaths.

Treating AF

Current medical treatment of AF mainly seeks to prevent significant symptoms from occurring in patients, especially life-threatening circulatory collapse and stroke. Two main approaches are taken to AF medication called *ryhtm* and *rate* control. The first attempts to end episodes of AF or prevent them from occurring, and maintain a normal ryhtm in the atria. The second attempts only to reduce the fast heart rate often associated with AF, without ending the fibrillation itself. Anti-coagulant medication is also commonly used, to reduce stroke risk. Drug treatments are often expensive due to use over longer periods of time, which can also lead to side-effects in patients.

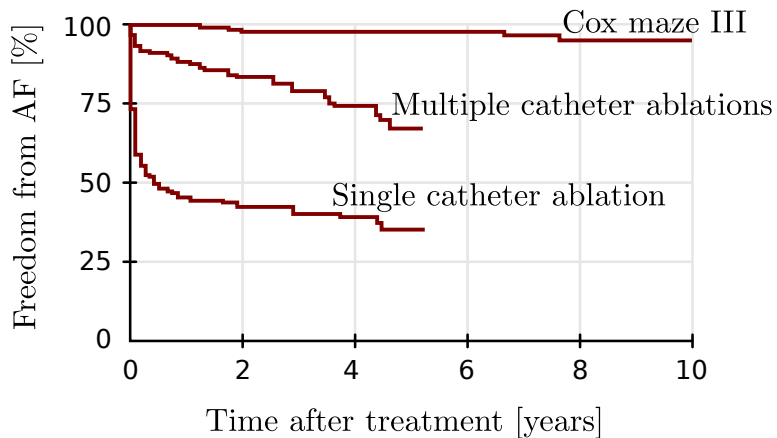


Figure 2.1: Kaplan-Meier estimator curves showing proportion of patients who are AF-free after treatment. The ‘multiple catheter ablation’ indicates follow-up after the final procedure. The data is taken from [Prasad et al., 2003] and [Weerasooriya et al., 2011] for the maze and ablation curves respectively.

Catheter ablation is a new surgical treatment that attempts to effectively treat AF at low cost and risk to the patient. In this procedure a catheter is inserted into the atrial chambers through one of the body’s larger veins. There it is used to burn or freeze areas of the tissue, altering its electrical conduction properties. Catheter ablation is minimally invasive and can provide quick, relatively inexpensive and effective treatment of AF. However, follow-up studies of patients, such as [Weerasooriya et al., 2011], show that about 50 % of patients relapse into AF within the first year of treatment, meaning several rounds of ablation might be necessary for it to be effective.

An older and more effective surgical treatment of AF exists, known as the Cox maze III procedure. First presented by [Cox et al., 1991], the treatment consists of making a series of incisions in the atrial tissue. Highly effective, the Cox maze is considered the gold standard in AF treatment. A study of 198 patients who underwent the Cox maze III, [Prasad et al., 2003], showed that 97 % of patients who were followed up after 5.4 years were still completely AF free—a very good success rate compared to catheter ablation, as shown in Figure 2.1. Even so, it is no longer widely used as it is highly invasive, requiring open heart surgery and incisions into the heart wall.

The current treatment options for AF are either highly invasive or relatively ineffective. This is the main motivation for the currently large effort on fundamental atrial fibrillation research. An important tool in this research is the use of mathematical models, which is the fundament of this thesis.

2.2 Using Mathematical Models

[[Sterratt et al., 2011](#)] defines a mathematical model as a specific set of mathematical equations that can be solved to produce a specific prediction from a given set of initial conditions. Mathematical models are needed to remove ambiguity from our scientific theories. By attempting to describe a given system with a mathematical model, one arrives at very specific predictions that can be compared to empirical experiment in detail—this forces the modeler to keep his or her underlying assumptions and hypotheses consistent with each other and with experimental results.

Such mathematical models become important tools in our search for understanding of a system, as they let the modeler make predictions following adjustments to the initial condition or model parameters. And while at the end of the day it is only empirical experiment that can be used to validate or reject an empirical theory, models can lead to deeper understanding of established theories and are often vital in finding what experiments to conduct.

In our case, the mathematical model in question is a model of the electrical behaviour of a human atrial myocyte. Cell models such as this are based on a large collection of experimental studies on atrial cells from both humans and other mammals. Once extracted from a live subject, these cells can be grown and studied in cell cultures. An important experimental technique that has enabled the formulation of precise mathematical electrophysiological cell models is the *patch clamp*. Following the formulation of a cell model based on experimental studies, the model can be explored to for example study the effects of cell remodeling or the effects of drug intervention on the cell.

2.3 Ethical Concerns

As the models we are working with in this thesis are based on medical experimentation, it is important to address the ethical concerns attached to such research.

To gain fundamental understanding of how the human heart works, medical data from real human hearts is needed. Such data can be obtained through medical experiments, but many ethical concerns arise. The *Nuremberg code* was written following World War 2 to protect the human rights of subjects in medical research. Along with the *Declaration of Helsinki*, first adopted in 1964, the code has been a cornerstone for modern regulations on clinical research ([\[Shuster, 1997\]](#)).

The use of human subjects raises ethical concerns, as with the exception of certain experimental treatments, the subjects themselves rarely have any self-interest in

attending. On the other hand, the research itself could lead to medical advancement, giving benefit to future patients. It is the balance of the rights of the patient and the humanitarian benefit of the research that leads to an ethical dilemma. In both the Nuremberg code and current regulations, informed consent from the subject is strictly necessary, but not sufficient, to carry out medical experiments. That is, even if a subject is providing complete informed consent, there are strict rules such experiments need to follow.

An alternative to experiments carried out on living humans are experiments on other live animals. Experiments on animals also raise difficult ethical questions, especially so because animals cannot give informed consent. Despite this, regulation on animal experiments is generally looser than that on humans. In fact, the third point of the Nuremberg code states that any experiment carried out on a human subject must be based on previous animal experiments. Both historically and today, most experimental cardiac research is carried out on animals, especially so on mammals due to their close-to-human physiology. Much of this thesis is based on work that would not exist were it not for experiments carried out on animals.

While it is clear that experimentation on both humans and animals produces ethical dilemmas, virtual experiments using computational models have no such ethical cost. And while all computational models are ultimately useless without empirical experiments to constrain them, they can serve as important tools to both explore specifically what real-life experiments are actually necessary—as well as making sure we extract the most out of the experiments we actually conduct.

Chapter 3

Cardiac Physiology

In this Chapter, we aim to give the reader a brief overview of the cardiac physiology underpinning the modeling work in this thesis, with the intention of making the work more accessible to those without a background in biology or physiology.

Most of this Chapter is based on [[Katz, 2010](#)], which is highly recommended to readers who want a more detailed introduction to cardiac physiology.

3.1 Structure and Function

The heart's main function is to drive the cardiovascular system, a crucial transport system distributing blood to the body. Together with the lymphatic system, the cardiovascular system forms the circulatory system of the body, responsible for supplying most of the body's cells with nutrients and oxygen, and collecting waste.

From a physiological viewpoint, the heart is a complex organ. It consists of four chambers, all filled with blood. Following an electrical activation, muscle cells in the cardiac tissue contract, causing the pressure to increase and blood to be ejected from the chamber. A system of cardiac valves open and close in phase with the contractions to make sure that blood flows in the correct direction and prevent backflow. From the reductionist viewpoint of a physicist, the heart can simply be viewed as an electromechanical pump—or more correctly, a collection of pumps coupled in series.

A diagram of the heart is shown in Figure 3.1. The two topmost chambers are the atria, while the bottom two are the ventricles. The atria and ventricles are distinguished by their lateral location in the body, being denoted either the left or right chamber. The left atrium and ventricle are connected by a valve and

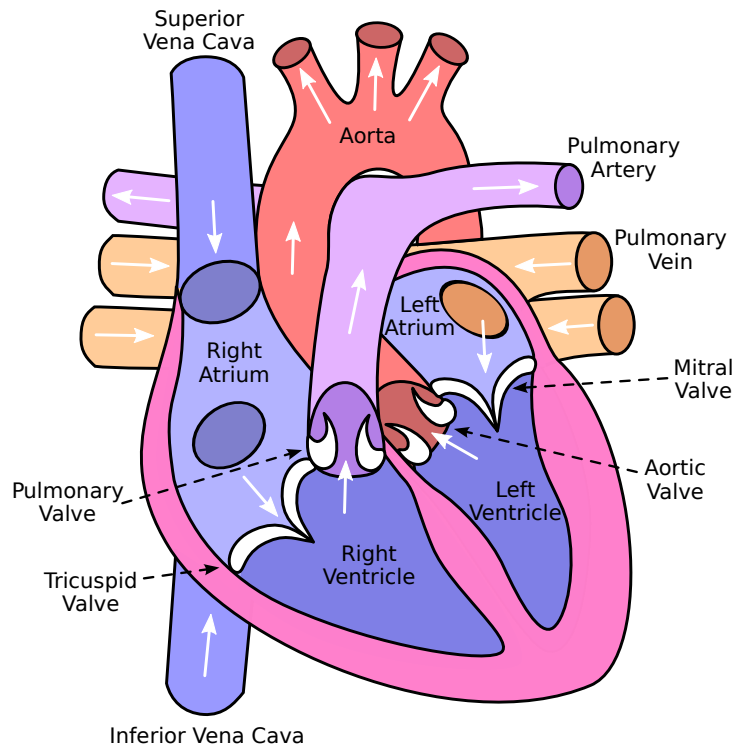


Figure 3.1: Schematic of the human heart with connected arteries and veins. Valves are indicated with dashed black arrows, while white arrows indicate direction of blow flow through the heart. Figure adapted from Wikimedia Commons and used under a CC by-sa 3.0 license, see [[Creative Commons, 2007](#)] for details.

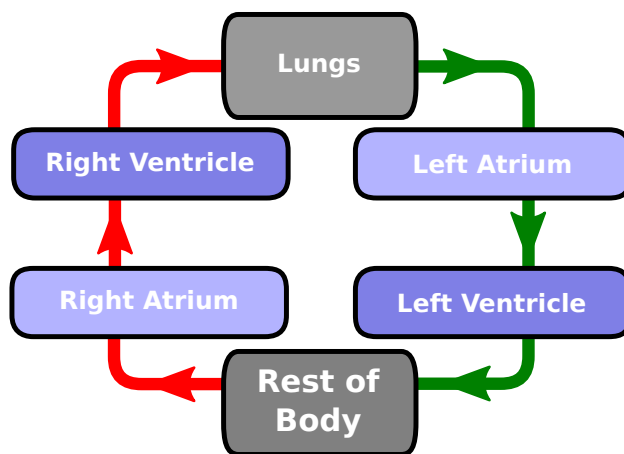


Figure 3.2: Flow of blood through the heart and body. The green arrows indicate that blood is oxygen-rich, while the red arrows indicate deoxygenated blood. Blood is carried away from the heart through *arteries*, and carried back to the heart through *veins*.

blood can flow between them; the same is true for the right atrium and ventricle. However, no blood can flow between the left and right chambers.

Blood enters the heart through the atria, and leaves through the ventricles. A simplified overview of the flow of blood through the heart is shown in Figure 3.2. The right pair of chambers receive deoxygenated blood from the body and send it to the lungs. The left pair of chambers receive freshly oxygenated blood from the lungs and drive it to the rest of the body. The atrial chambers' role is to receive blood from the body and lungs, while the ventricles pump it out into the body. Although the atria contract to pass blood along to the ventricles, this contraction is much weaker than that of the ventricles. The weaker atrial contraction occurs right before the ventricle contraction, increasing the volume of blood in the ventricles, leading to a higher volume of ejected blood. This process is known as the *atrial kick*. The main role of the ventricles in pumping blood to the entire body is reflected in their much larger size and thicker chamber walls.

From an engineering perspective, one can wonder if the atria are really needed. Two pumps in series can be replaced by a single, stronger pump. However, the two-pump system of the heart has some major advantages. The ventricles contract at a regular pace, leading to pulsatile outflow of blood from the heart. As blood is forced into the tissues of the body, blood already occupying these tissues is forced back into the heart. Valves between the atria and ventricles and between the ventricles and the arteries prevent backflow during the contraction and relaxation of the ventricles. In comparison, there are no valves between the veins and the atrial chambers. This enables continuous and uninterrupted flow from the veins into the heart throughout the heart cycle. In an atria-free design, inflow of blood would have to be pulsative. Blood being prevented from entering the heart would require negative work and pulsatile inflow would therefore be highly ineffective. In the study [Anderson et al., 1967] mechanical pumps were designed to simulate the heart. They found that the atrial chambers allowed for roughly a 75 % increase in total cardiac output by reducing circulatory inertia.

Ventricular contraction is crucial to drive the circulatory system. During ventricular fibrillation there isn't sufficient contraction to drive blood through the body and ventricular fibrillation therefore requires immediate medical attention. In comparison, if the atrial chambers are not contracting properly, but instead quiver or fibrillate, the atrial kick is diminished or gone. Even so, the atrial chambers still allow continuous venous inflow of blood, meaning the most important function of the atria is still preserved. This is why atrial fibrillation is not a life threatening condition on its own.

3.2 Cardiac Myocytes

The contraction of the cardiac tissue, called the myocardium, happens because the individual muscle cells, called myocytes, contract. These muscle cells are cylindrical in shape and are coupled longitudinally, creating long muscle fibers. The tissue is built up of many such fibers in parallel forming a sheet of fibers, and layers of such sheets form the heart walls. Contraction of individual myocytes leads to a shortening of muscle fibers and contraction of the heart wall.

Cardiac muscle cells are unique to the heart, and are different in composition and function from smooth and skeletal muscle, the two other types of muscle cells we find in the body. Like any other cell in the human body, they consist of a cytoplasm surrounded by a membrane, and immediately outside the cell we find the extracellular fluid.

The cytoplasm is the interior of the cell, which consists of different specialized substructures called organelles surrounded by the cytosol, a liquid full of dissolved ions and various molecules. Cardiomyocytes contain many different types of organelles, but we will not give most of them much thought, instead treating the myocyte as a black box. However, three types of organelles are especially of interest to note:

- *Mitochondria*, organelles that are often referred to as the ‘power plant’ of the cells. They specialize in producing adenosine triphosphate (ATP). ATP is a molecule that is used to store and transfer energy internally in the cell and can be thought of as small energy packet that is easily moved and consumed. Contraction means performing work and expends energy in the form of ATP. As cardiomyocytes have to be able to contract at a regular pace, they need to produce a lot of ATP and often have more mitochondria than other types of cells.
- *Myofibrils*, thin rod-like structures consisting of different types of long proteins. These structures enable the contraction of the cell. Free calcium ions in the cytosol can bind to the myofibrils, causing the different protein structures in the fibril to slide past each other, shortening the cell. This process is fueled by ATP. The *sliding filament model of contraction* explains how myofibrils contract in detail. The thesis will not cover this model, but urge the reader to note that it is intracellular calcium that causes contraction of the myocyte.
- *Sarcoplasmic reticulum (SR)*, a specialized calcium-storage spread evenly throughout the cell. As calcium causes contraction of the cell, it cannot remain in the cytosol as the muscle relaxes. To remove cytosolic calcium, it is pumped into the SR. At the onset of contraction, calcium will be released

from the SR, resulting in a larger intracellular calcium concentration and a stronger and more uniform contraction.

A diagram of a myocyte and some of its important organelles is shown in Figure 3.3.

The cell membrane, called the sarcolemma, consists of lipids, fat-like molecules. These lipids consist of a hydrophobic tail attached to a hydrophilic head and can therefore form a bilayer, with heads on the outside and tails on the inside. This lipid bilayer forms a continuous barrier that is impermeable to ions and most molecules. Because of the membrane, the cytosol inside the cell can have a very different chemical composition than the fluid surrounding the cell. Due to different concentrations of electrically charged ions inside and outside the cell, an electrical field can exist across the membrane, leading to a potential difference. This potential difference is referred to as the transmembrane potential or simply the membrane potential and in electrophysiology is defined with respect to the inside of the cell. The membrane potential of the cell can be expressed as

$$V = V_i - V_e, \quad (3.1)$$

where the subindexes denote the extracellular and intracellular voltages.

The membrane potential of a cardiomyocyte changes drastically throughout the cardiac cycle of excitation, contraction, and relaxation. How can the membrane voltage change? The lipid bilayer contains different kinds of large proteins that span the membrane. If these proteins have the right functional shape they create pores in the membrane and ions can pass through. Such proteins are called *ion channels*, and are usually ion specific due to a structure called a selectivity filter. Ion channels can change their shape based on various physical stimuli and therefore open and close—leading to a change in both intracellular ion concentrations and the membrane potential.

3.3 The Nernst-Planck Equation

Ion channels in the membrane of the cell simply makes it porous, and the transport of ions through the channel will be a spontaneous process. This spontaneous movement of ions is a combination of two underlying driving forces. First, there will be a diffusive flux of ions due to the concentration gradient across the channel. This diffusive flux is described by *Fick's law*, which states that the net flux is proportional to the concentration gradient

$$\mathbf{J}_{X,\text{diff}} = -D_X \nabla \phi_X, \quad (3.2)$$

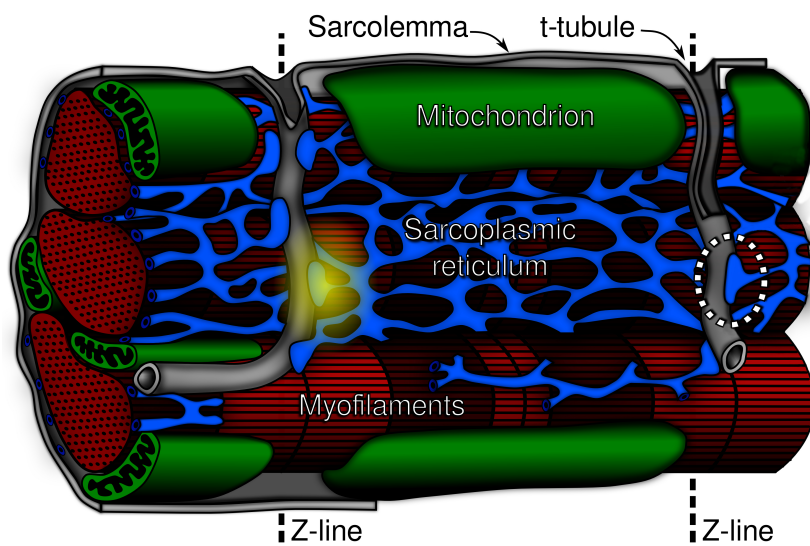


Figure 3.3: Cross-section of a cardiac myocyte. The sarcolemma is the membrane that separates the inside and outside of the cell. The sarcolemma occasionally burrows into the interior of the cell in tunnels called transverse-tubules (t-tubules). The mitochondria are the organelles that produce energy for the cell. The sarcoplasmic reticulum absorbs, stores, and releases calcium into the cytosol, with a calcium release shown with a yellow hue. Areas where the SR are close to the sarcolemma (including t-tubules) are called calcium release units (CRUs); an example is circled with a dashed line. Myofibrils are bundles of myofilaments that contract when calcium binds to them. The Z-lines are where two myocytes meet and are coupled longitudinally. Image taken from [Zipes and Jalife, 2000].

where X denotes a specific ion species, $\nabla\phi_x$ is the concentration gradient of the species and D_X the species-specific diffusivity.

In addition to the diffusive flux due to the concentration gradient, electrically charged ions will tend to drift due to the presence of an electrical field across the membrane. Net electric flux of ions due to electric drift is given by

$$\mathbf{J}_{X,\text{drift}} = -\frac{D_X F}{RT} z_X \phi_X \nabla V, \quad (3.3)$$

where ∇V is the gradient in the membrane potential, F is the Faraday constant, R is the gas constant, T is the system temperature in Kelvin, and z_X is the ion species valency, i.e., charge.

The electric drift can be in either the same or opposite direction of the diffusion, depending on the current membrane potential and concentration gradient. If the two point in opposite directions, the net movement of ions can be zero even when there is a concentration gradient and potential difference present. To describe this balance between the two driving forces we therefore combine the two fluxes, giving the *Nernst-Planck equation*

$$\mathbf{J}_X = \mathbf{J}_{X,\text{diff}} + \mathbf{J}_{X,\text{drift}} = -D_X (\nabla\phi_X - \frac{F}{RT} z_X \phi_X \nabla V). \quad (3.4)$$

The dynamical equilibrium where diffusion and drift are in balance across the membrane can be found from this equation. Assuming symmetry along the membrane we can set the net flux equal to zero and integrate the resulting equation across the cell membrane

$$\int_0^L \frac{\partial\phi_X}{\partial x} dx = - \int_0^L \frac{z_X F}{RT} \phi_x \frac{\partial V}{\partial x} dx, \quad (3.5)$$

where $x = 0$ is the inside and $x = L$ is the outside of the cell. Changing variables and denoting $\phi(0) = \phi_i$ and $\phi(L) = \phi_e$ gives the equilibrium potential of the passive ion transport

$$E_X = \frac{RT}{z_X F} \ln \frac{\phi_{X,e}}{\phi_{X,i}}. \quad (3.6)$$

This equilibrium potential is known as the *Nernst potential*. If the membrane potential is higher than the Nernst potential there will be a flux of ions through the membrane driving the Nernst potential up due to changing concentrations. The electrically charged ions also carry a current that will drive the membrane potential down toward the Nernst potential. If the membrane potential is lower, the situation is reversed, and the Nernst potential is therefore often referred to as simply the *reversal potential*.

In addition to ion channels in the membrane with a passive transport of ions, there are proteins known as ion exchangers and ion pumps. These also allow

ions to move across the cell membrane, but in this case the ions do not move spontaneously through the membrane due to their electrodiffusion gradient, but are instead forced in the opposite direction, against the gradient. This *active* transport of ions is accomplished by use of either ATP (ATPase) or the energy released by a cotransport of another ion species moving spontaneously.

3.4 The Action Potential

The Nernst potential is species-specific and will only be a true equilibrium if the membrane is permeable to only that species. For a membrane permeable to several types of ion, the Nernst potential will still give an indication of what way the different ionic species are pulling the current membrane potential.

The three ion species most important for the membrane potential of cardiomyocytes are sodium, Na^+ , potassium, K^+ , and calcium, Ca^{2+} . Using typical values for mammalian cardiomyocytes given in [Katz, 2010], the Nernst potential for these three ions will be

$$E_{\text{Na}} = \frac{RT}{F} \ln \frac{110 \text{ mM}}{8 \text{ mM}} = 70 \text{ mV}, \quad (3.7)$$

$$E_{\text{K}} = \frac{RT}{F} \ln \frac{4 \text{ mM}}{100 \text{ mM}} = -86 \text{ mV}, \quad (3.8)$$

$$E_{\text{Ca}} = \frac{RT}{F} \ln \frac{1 \text{ mM}}{0.2 \text{ } \mu\text{M}} = 114 \text{ mV}. \quad (3.9)$$

Sodium and calcium transport will tend to push the membrane potential up, while potassium transport will tend to pull it down. The balancing of these effects will depend on the permeability of the membrane to the different ion species. A higher permeability will lead to a larger transport of ions per time and a larger effect on the dynamical equilibrium.

A cardiomyocyte at rest has a membrane that is much more permeable to potassium than sodium or calcium and will therefore have a resting potential close to the equilibrium potential for potassium, around -80 mV. The membrane is thus very polarized at rest. If the membrane potential is increased slightly, sodium channels in the membrane will open, vastly increasing the sodium permeability and rapidly increasing the membrane potential to values of about 40 mV in a few milliseconds, *depolarizing* the cell.

Cardiomyocytes are called *excitable cells*, as it only takes a small perturbation of the membrane potential to trigger a large response. The cells' response to stimulus is called an *action potential* (AP). The rapid depolarization of the membrane is only the first phase, and the action potential is the whole response, including the return of the membrane potential to resting levels, *repolarization*. Ventricular

and atrial cardiomyocytes have quite different action potential shapes, Figure 3.4 on the following page shows these.

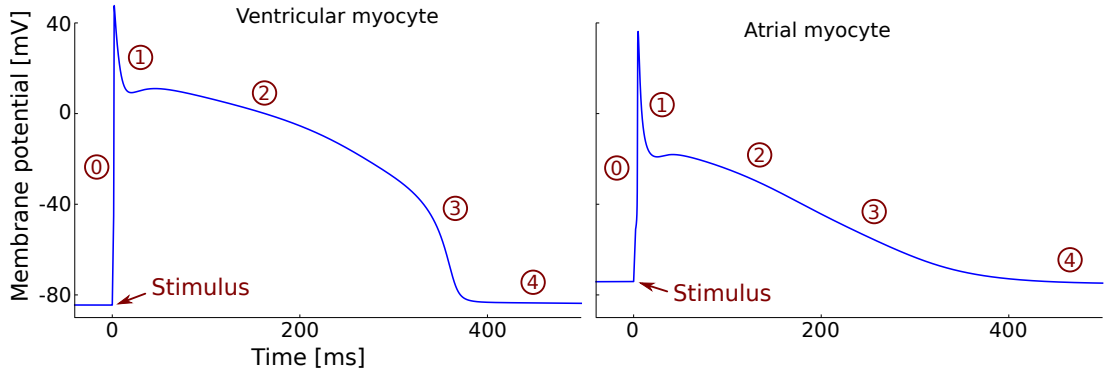


Figure 3.4: Action potentials for a ventricular myocyte (left) and atrial myocyte (right). The number-labels denote the different phases of the AP. Phase 0 is the *upstroke*, i.e., rapid depolarization of the membrane potential. Phase 1 is the *early repolarization* that leads to a notch in the AP. Phase 2 is the *plateau*, which is much more pronounced in the ventricular AP. Phase 3 is the *late repolarization* of the membrane potential. Phase 4 is return to the resting potential or *diasole*.

While a cell is firing an action potential, it is not sensitive to any new stimulus and is thus not excitable, instead the myocyte is *refractory* and incapable of firing another action potential. The refractory period is important to prevent continuous activation of the myocyte and guarantee that the heart walls relax for long enough to allow the heart to fill with blood before the next contraction occurs.

3.5 Intracellular Calcium Dynamics

Action potentials of cardiomyocytes look very different to those of other excitable cells such as skeletal myocytes and neurons. In these other cell types, the repolarization of the membrane potential is as fast as the upstroke, leading to a rapid and narrow AP often referred to as a spike. Cardiomyocytes have calcium channels that open when the membrane becomes depolarized, and close when it repolarizes. The longer the AP, the longer membrane calcium channels remain open and the more calcium is allowed to enter the cell, leading to a stronger contraction. The strength of contraction is thus strongly linked to the action potential duration, especially the plateau phase.

The sarcoplasmic reticulum (SR) inside the cytoplasm has its own lipid bilayer, much like the myocyte membrane. This allows the SR to contain very high con-

centrations of calcium compared to the cytosol. This calcium can be released through calcium release channels called ryanodine receptors (RyR) in the SR membrane. Calcium release from the SR is triggered by cytosolic calcium ions binding to RyR, causing it to open and release calcium. When the cell fires an action potential, calcium enters the cell through sarcolemmal calcium channels; some of this calcium will bind to RyR triggering a second intracellular calcium release. This phenomenon is known as calcium-induced calcium-release (CICR). As calcium released from the SR increases cytosolic calcium, it will further activate other RyR channels, triggering further calcium release. To prevent this feedback loop of calcium release from emptying the SR completely, the RyR shut off shortly after opening and become refractory, preventing further release.

Following excitation of the myocyte and calcium influx triggering CICR, the cytosolic calcium has increased significantly. Before the onset of the next contraction, calcium must be removed from the cytosol. Some of the cytosolic calcium is pumped back into the SR through ionic pumps known as sarcoplasmic/endoplasmic calcium ATPase (SERCA). The amount of calcium pumped by SERCA has to be roughly equivalent to the amount of calcium released through RyR, otherwise there would be an accumulation or depletion of calcium in the SR. The remaining cytosolic calcium, equivalent to the amount entering the cell through sarcolemmal calcium currents, is pumped back out of the cell by the sodium-calcium exchanger (NCX) and the plasma-membrane calcium ATPase (PMCA). The PMCA, or simply calcium pump, expends energy in the form of ATP to push calcium against its concentration gradient. The NCX on the other hand, lets sodium into the cell, using the energy released by sodium traveling along its electrodiffusion gradient to transport calcium out of the cell.

The influx of calcium through the sarcolemma and triggered calcium release from the SR both cause cytosolic calcium concentration to rapidly increase following the upstroke of the action potential. During the plateau phase of the AP, the cytosolic Ca^{2+} concentration peaks and starts to fall as it is removed from cytosol. The time-evolution of the cytosolic Ca^{2+} is known as the calcium transient (CaT) of the cell, and closely resembles the action potential in shape. As cytosolic Ca^{2+} causes contraction of the cell, CICR following an action potential is important to rapidly generate a sufficiently large CaT for contraction to occur.

Diffusion is a slow process, and if intracellular calcium had to diffuse from the outside of the cylindrically shaped cell into the center, activation of myofibrils would be unsynchronized. To spatially homogenize the calcium transient throughout the cell, the sarcolemma has tunnels reaching into the interior of the cells. These tunnels are known as transverse-tubules (t-tubules) and make sure all myofibrils are functionally close to the sarcolemma of the myocyte. The SR is spread throughout the cell but is often found wrapped around t-tubules to create a high-fidelity CICR coupling. Areas where the sarcolemma/t-tubule and

the SR are neighboring are called calcium release units (CRUs) and are the fundamental units of calcium release in the cell. After calcium has entered the cell and triggered calcium release from the CRUs, calcium diffuses out into the rest of the cytosol. The parts of the cytosol containing CRUs are referred to as the junctional cytosol, while the remaining is the non-junctional, or bulk, cytosol.

Big differences are found in the t-tubular structures of ventricular and atrial myocytes. Ventricular myocytes are larger in size and have a very regular and well developed t-tubular network. Atrial myocytes, on the other hand, are often seen to have a significantly less developed or even entirely absent t-tubular network. The extent of atrial myocyte t-tubular networks varies in different mammalian species, being more well-defined in larger mammals such as dogs, cows, horses and humans ([Richards et al., 2011]). Significant variations are also found within the atrial tissue of a single organism. The smaller presence of an organized t-tubular network leads to atrial myocytes having a more spatially heterogeneous calcium transient that also lasts longer than those found in ventricular myocytes. Figure 3.5 on the following page shows t-tubular structures in ventricular and atrial rat cells.

3.6 Activation of the Myocardium

We have discussed how cardiomyocytes are excitable and will fire a contraction-causing action potential following a small stimulus. Now we look at what this stimulus is in the cardiac tissue and how contraction is coordinated throughout the whole heart.

When two myocytes neighbor each other, *connexin* proteins can connect the two cell membranes forming *connexons*, pores linking the cytosol of the two cells directly. This leads to a gap junction forming between the two myocytes, a highly permeable channel where ions can flow directly from the cytosol of one cell to the other without going through the extracellular fluid. If a myocyte is triggered to fire an action potential, increased ionic concentrations will lead to a diffusion of ions to neighboring cells with lower concentrations, through gap junctions. This ionic flux causes a depolarization in the membrane potential of the neighbor cell, potentially triggering an action potential in that cell as well.

Cardiac tissue contains many gap junctions, effectively electrically coupling all myocytes together forming a functional *syncytium*, a network of cells acting together as a single unit. If a small part of the tissue is activated this will cause a chain reaction where neighboring cells are activated, who in turn depolarize their neighbors and so on. This domino effect will spread through the tissue like a wave, depolarizing the tissue and triggering contraction as it moves across it. Mathe-

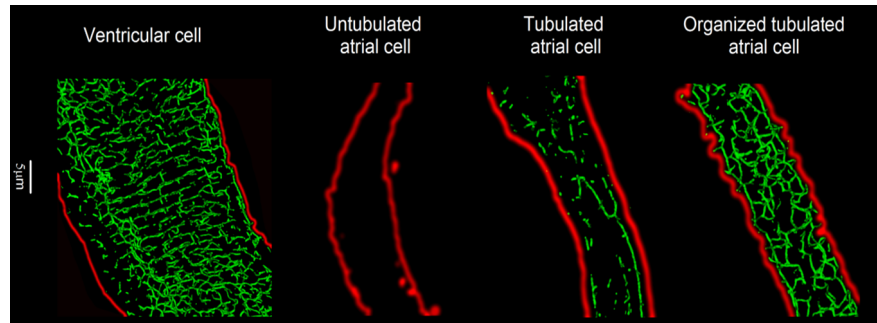


Figure 3.5: 3D reconstruction of t-tubular networks in isolated rat myocytes, the red lines shows the sarcolemma. The leftmost image is a ventricular myocyte showing a highly developed t-tubular network. The three other Figures shows three atrial myocytes with different levels of t-tubular networks. The rightmost atrial myocyte with a organized t-tubular network are at a minority in rat atrial myocardium. Figure taken from [Frisk et al., 2014].

matically, this wave of depolarization can be described with a reaction-diffusion model. For a one-dimensional strand of tissue, one can model the propagation of the depolarization using the *cabal equation*, while in two or three dimensions the *bidomain model* is usually used.

Normally, the wave of excitation starts at the top of the heart in the *sinoatrial node* (SA node), a specialized region of the atria. The SA node contains *pacemaker cells*, specialized cardiomyocytes that self-excite at a regular pace. As the atrial tissue is a well-connected syncytium, a wave of depolarization can therefore start at the SA node and spread throughout the atria. The ventricular tissue is another well-connected syncytium, but the atrial tissue and ventricular tissue are electrically separated. In a healthy heart, the only connection between the two is the *atrioventricular node* (AV node), a point in the middle of the heart where the electrical excitation can spread from the atrial to the ventricular syncytium.

The conduction through the atrial and ventricular myocardium is very rapid, propagating at roughly 1 m/s. The rapid conduction allows the tissue to contract as one, maximizing the effectiveness of the contraction. Conduction through the AV node, on the other hand, is about a hundred times slower, leading to a conduction delay between the two syncytia which makes sure the atrial chambers are allowed to contract fully before the ventricles contract.

3.7 Reentry and Fibrillation

Under normal conditions, the wave of excitation begins at the sinoatrial node, moves across the tissue, and then dissipates. As the tissue immediately behind

the wavefront will have just been activated, it will be refractory and there will be no way for the excitation to move back up the heart. This guarantees that it is the rate of pacemaker activity in the SA node that decides the heart rate. The rate of pacemaker activity of the SA node is, in turn, affected by the central nervous system with *sympathetic* stimulation increasing heart rate and *parasympathetic* stimulation decreasing it.

Under special conditions, however, there is the possibility for a wave of depolarization to be set up in the tissue in such a way that it loops back around the heart wall and re-enters tissue which has had enough time to recover and is excitable again. If such a reentrant wave moves slowly enough, it will never catch up to its ‘tail’ and therefore never die out. This is an example of a self-sustaining *spiral wave*. Such a self-sustaining reentrant wave will cause excitation of the tissue and contraction at a rate depending solely on the spiral wave period. The spiral wave thus ‘overrides’ the pacemaker activity of the SA node and leads to *reentrant arrhythmia*, an irregular heartbeat resulting from reentrant waves.

Due to rapid conduction in cardiac tissue, spiral wave periods are typically short, leading to a very fast heart rate referred to as a *tachycardia*. While the tachycardia is an abnormally high heart rate, it is still a fairly coordinated contraction of the tissue. Over time, a tachycardia will often develop into a fibrillation where the tissue is contracting in a chaotic and uncoordinated fashion. It is believed that the development from tachycardia to fibrillation is due to unstable spiral waves breaking up into chaotic and turbulent smaller waves in the tissue. These smaller wavefronts are still self-sustaining in the tissue, but they move around unsynchronously, combining and breaking up in chaotic ways. The complex electrical impulses in the tissue lead to asynchronous contraction, i.e., fibrillation.

Several explanations for how and why spiral wave breakup occurs have been proposed, but it still remains an important focus of research. Clinical research on the topic is difficult, due to easily available electrophysiological measurements, such as ECG, only capturing the averaged electrical activity at the surface of the heart and not throughout the myocardium. The phenomenon can, however, be studied using idealized mathematical models of excitable tissue. Figure 3.6 on the following page shows an example of spiral wave breakup in such a computational model.

For reentry to occur, there needs to be a triggering event, such as a premature stimulus, hitting a *vulnerable substrate*. The substrate can either be an anatomical structure or a functional dynamical property of the tissue. Anatomical reentry occurs because an anatomical pathway can conduct an electrical impulse back into excitable tissue. An example is AV node reentry tachycardia, which is the most common reentrant ventricular tachycardia. This reentry is caused by the AV node consisting of two pathways, one with a longer refractory time. Normally

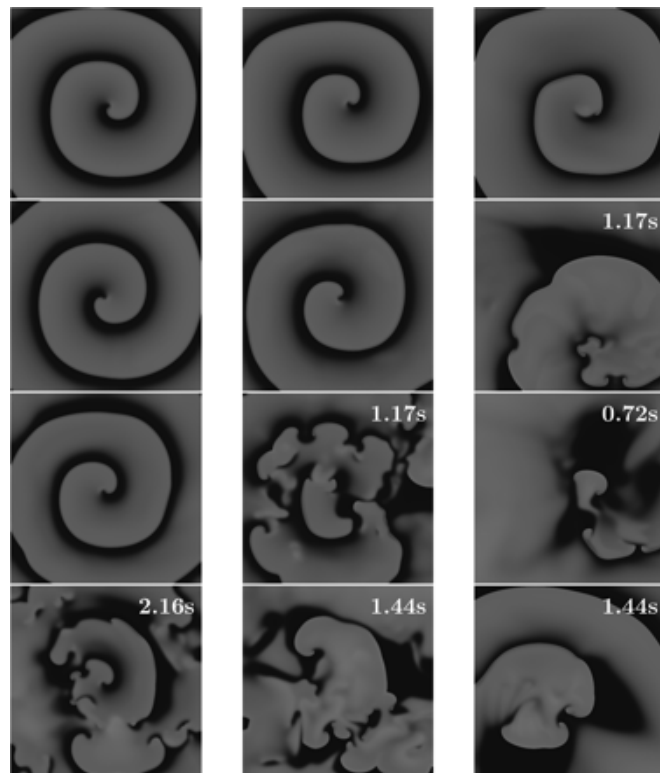


Figure 3.6: Spiral waves and spiral wave breakup in a computational model of excitable tissue. The different Figures correspond to different sets of model parameters leading some to feature stable spiral waves, while other feature break up after a short time. The numbers shown in the upper right indicate the time at which break up occurred after spiral wave initiation. Figure taken from [[ten Tusscher and Panfilov, 2006](#)].

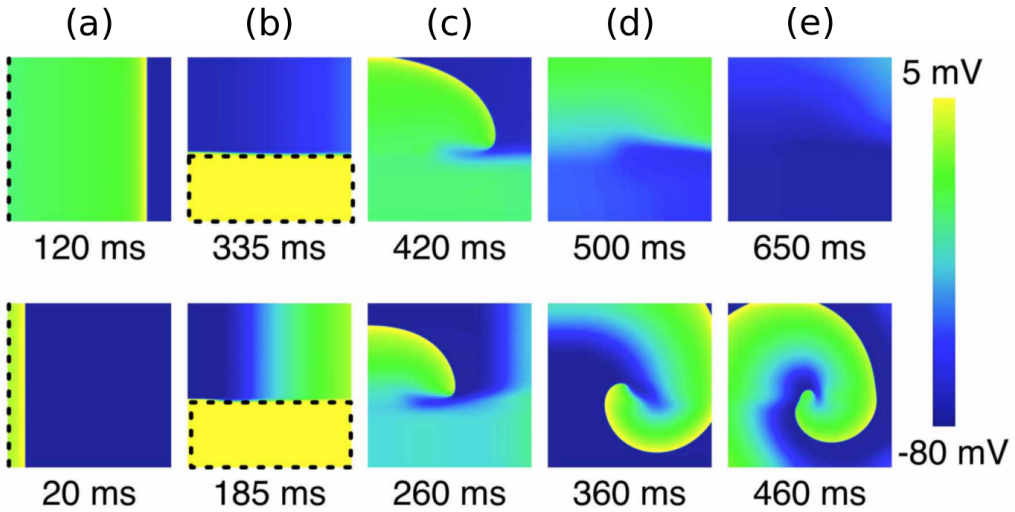


Figure 3.7: Induction of spiral waves due to a premature stimulus in a computational model of excitable tissue. The panels show the time evolution of the system running left to right, with the numbers below the panels denoting the system time. The top and bottom panels show two different simulations. The same model is used for the two simulations, but the timing of the premature stimulus is different. (a): The tissue square is initially paced at a regular pace on the left side of the tissue, creating planar waves that spread across the tissue from the left to the right. (b): A premature stimulus occurs in the bottom half of the tissue square. (c): Because of the planar wave, the right hand side of the tissue is refractory, but the left hand side is not. The premature stimulus therefore initiates a secondary wave that moves up the left hand side of the tissue. (d): Depending on the timing of the premature stimulus, the secondary wave can either run out of excitable tissue and dissipate (top), or wrap around the right hand side of the tissue (bottom) and *re-enter* the tissue. (e): In the top panel, reentry did not occur and no spiral wave has been initiated. In the bottom panel, reentry occurred and a stable spiral wave has formed in the system. Figure adapted from Figure 6 in [Wilhelms et al., 2012], and used under a CC by 3.0 license, see [Creative Commons, 2007] for details.

both pathways are activated at the same time, but if there is a premature stimulus from the atria one pathway can be refractory—the impulse can then travel up the other pathway in the reverse direction and a reentry is established. Functional reentry, on the other hand, requires no anatomical structure, but instead relies on a functional substrate in the form of heterogeneities in the tissue. One example would be a gradient in refractoriness in the tissue. An example of reentry due to a functional substrate is shown in Figure 3.7, where a premature stimulus initiates spiral waves in a tissue model due to a gradient of refractoriness in the system.

A more extensive review of reentry, spiral wave breakup, and their connection to arrhythmia can be found in [Fenton et al., 2008].

3.8 Cardiac Alternans

Many possible substrates for human AF have been discussed, but perhaps the most important functional substrates are cardiac alternans. Alternans are beat-to-beat variations in the action potential of the cardiomyocyte at a constant heart rate. Different types of alternans exist. Mechanical alternans are variations in the myocytes' strength of contraction. Electrical alternans are variations in the action potential duration (APD) or action potential amplitude (APA). Calcium alternans are variations in the peak of the calcium transient. All of these measurements are tightly connected in cardiomyocytes and if one type of alternans is present, the other types usually are as well. It can occasionally be important to distinguish the types though, as they have been found to occur separately in certain studies ([Gaeta and Christini, 2012]).

Cardiac alternans occur in individual cardiomyocytes. If groups of myocytes alternate simultaneously, tissue-level alternans arise. Tissue-level alternans can be spatially *concordant*, meaning all myocytes alternate in phase, or *discordant*, meaning they alternate out of phase. An illustration of these situations are shown in Figure 3.8. Two neighboring regions alternating out of phase will lead to significant heterogeneities, especially so at the border line between the two regions. This forms a functional substrate for the onset of functional reentry. For a more in-depth review of the arrhythmic properties of spatially discordant alternans see [Weiss et al., 2006].

To study spatially discordant APD alternans as a AF substrate, [Narayan et al., 2011] induced AF in patients by rapid pacing. A total of 33 patients were divided into three groups: 1. patients with persistent AF, 2. patients with paroxysmal AF and 3. a control group without AF. In all three groups, APD alternans were observed during rapid pacing, but patients with prior AF exhibited alternans at slower pacing than the control group. The reported cycle lengths required to trigger APD alternans were

- Persistent AF group developed APDa at cycle lengths of 411 ± 94 ms.
- Paroxysmal AF group developed APDa at cycle lengths of 372 ± 72 ms.
- Control group developed APDa at cycle lengths of 218 ± 33 ms.

The APD alternans provided a functional substrate for AF that could be triggered by ectopic beats, causing the alternans to dissolve into complex oscillations that eventually led to AF. Their observations point to spatially discordant alternans

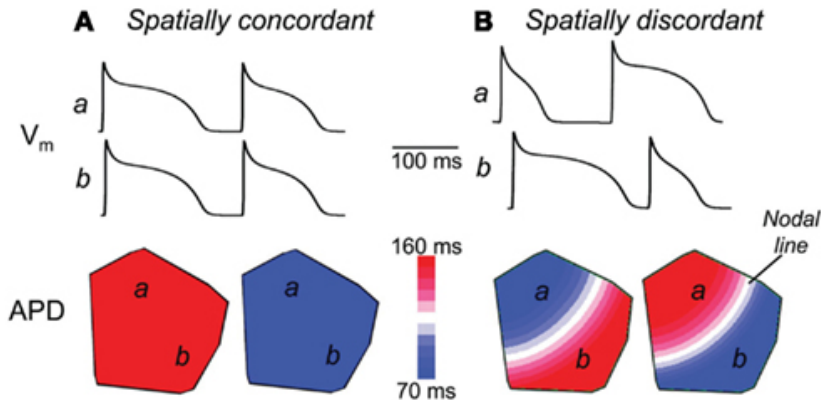


Figure 3.8: APD alternans seen in a computational tissue model. The two top panels show action potentials of myocytes in points **a** and **b**. The bottom panels show APD in different parts of the tissue. In the panels on the left, marked **A**, we see spatially concordant alternans, i.e., the entire tissue has a long or short action potential simultaneously. In the right panel, marked **B**, the alternans are spatially discordant. Roughly half the tissue has a short APD while the other half has a long APD. The situation will reverse from beat to beat. The spatially discordant alternans lead to tissue APD heterogeneity that is the greatest at the border between the two regions. Figure adapted from Figure 1 in [Weiss et al., 2006].

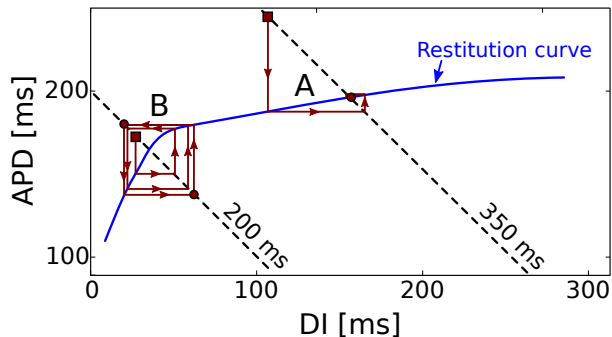


Figure 3.9: APD alternans in a myocyte arising from steep restitution. The curved blue line is the restitution curve of the myocyte and the diagonal black lines correspond to a constant cycle length (CL). When paced at a constant rate, all beats must land on the CL curve as $APD + DI = CL$. One can find where the next beat will land by tracing a vertical line from the current beat to the restitution, and then a horizontal line back to the cycle length. Drawn in red are hypothetical scenarios where the pacing rate is changed to the given cycle length starting from the initial beat (squares) to the steady-state beats (circles). **(A):** The cycle length intersects a shallow part of the RC and the myocyte quickly finds a steady cycle with a constant APD. **(B):** The cycle length intersects a steep part of the restitution and the myocyte now stabilizes in a pattern with an alternating APD. This Figure was inspired by Figure 3 in [Weiss et al., 2006].

being tightly linked to AF; in fact, they observed APD alternans preceding AF in *all* cases. And the patients where rapid pacing did not trigger AF, showed no APD alternans.

3.8.1 Restitution-driven Alternans

The duration of each cardiac cycle is known as the cycle length. As this is the time between each activation of the cardiomyocyte we also refer to it as the pacing cycle length (PCL). As the heart rate increases, cardiomyocytes are paced more frequently, meaning the cycle length shortens. Alternans occur when cardiomyocytes are paced rapidly ([[Gaeta and Christini, 2012](#)]). Historically this was attributed to APD restitution, a phenomenon wherein the action potential duration shortens as the myocyte is paced more quickly. To understand why this occurs, it is helpful to divide the cardiac cycle into two main phases: contraction and rest, or action potential the and diastolic interval (DI). Thus the PCL can be expressed as

$$\text{PCL} = \text{APD} + \text{DI}. \quad (3.10)$$

When the PCL is shortened, either the APD or DI has to drop. At long cycle lengths, the APD is of almost constant length and it is therefore the DI that is reduced as the rate of pacing increases. However, when the pacing starts to become more rapid it is important the diastolic interval remains sufficiently long to allow the heart to fill with blood between contractions, and the APD therefore has to begin to shorten as the PCL is shortened.

Restitution is mainly a result of the slow inactivation gates of depolarizing ion channels in the sarcolemma. A longer diastolic interval allows the ion channels to fully ‘reset’, leading to larger current in the following action potential, and a longer action potential duration. During a short diastolic interval on the other hand, the ion channels will still be partially inactivated at the onset of the next cycle leading to a weaker current and shorter APD.

A first order approximation to model restitution is to state that the APD of the current beat can be found as a function of the preceding diastolic interval

$$\text{APD}_{n+1} = f(\text{DI}_n), \quad (3.11)$$

where n denotes the cardiac cycle and f is the restitution curve of the myocyte. From this first order approximation of the restitution properties of the myocyte, it can be shown mathematically that there exists a single stable APD value as long as the steepness of the restitution curve is smaller than one, but that it can alternate between two values if the curve is steeper than one ([[Nolasco and Dahlen, 1968](#)]). A graphical representation of this is shown in Figure 3.9.

APD alternans arising from steep restitution are known as restitution- or voltage-driven alternans and were first proposed by Nolesco and Dahlen. It became the first widely accepted theory on the origin of alternans, and provides a convenient way to study the phenomenon of alternans in computational models. An example is [[Qu et al., 2000](#)], where the authors used restitution-driven alternans to study reentry in a tissue with spatially discordant alternans.

However, while the theory is an elegant explanation of many experimental findings, it is far from perfect. The approximation that the APD is a function of the preceding DI alone will in many cases be too simplistic, as the cardiomyocyte system has a significantly longer memory than a single cardiac cycle. For instance, alternans are often seen at pacing rates where the slope of the restitution curve is considerably less than 1, or they are not present when the slope is steeper than 1 ([\[Gaeta and Christini, 2012\]](#)), which is at odds with the theory of restitution-driven alternans.

3.8.2 Calcium-driven Alternans

An alternative hypothesis for the origin of cardiac alternans is that they are primarily caused by intracellular calcium dynamics. If these dynamics are unstable, they can lead to calcium transient (CaT) alternans that will lead to secondary APD alternans. This hypothesis was strengthened by experiments, such as [[Chudin et al., 1999](#)], that showed CaT-alternans in cardiomyocytes that were clamped and forced to have stable action potential duration. Due to the AP clamp, the observed CaT-alternans could not just be a consequence of APD-alternans, but had to have their own origin. Several mechanisms for calcium-driven alternans have been proposed.

One possible mechanism is an instability in Ca^{2+} -cycling in and out of the sarcoplasmic reticulum (SR). During excitation, calcium is released from the SR and during diastole this calcium is pumped back into the SR through SERCA pumps. The hypothesis is that this cycling of calcium is not quick enough to facilitate rapid pacing. If SERCA is not given enough time to refill the SR, diastolic SR load will be low in the following cardiac cycle. This leads to a smaller SR release. As the release is lower, SERCA will have more time to refill the SR, restoring the diastolic SR calcium load. Thus CaT-alternans and diastolic SR load fluctuations arise. The steeper the dependence of the release flux on the SR load, the easier it will be for diastolic SR fluctuations to grow into stable alternans. This is much like a steeper dependence of APD on the preceding DI being the mechanism of restitution-driven alternans.

much like a steeper APDthe mechanism of restitution-driven alternans.

[Picht et al., 2006] experimentally tested the hypothesis that alternating diastolic SR calcium concentrations are required for calcium alternans and found that they were not. They observed cases where the SR fluctuations were too small to account for the calcium alternans, as well as cases where clear calcium alternans occurred with no fluctuations in the SR concentration. The authors instead suggested refractoriness of the ryanodine receptors (RyR) responsible for calcium release as a primary mechanism of alternans. This mechanism suggests that RyR will be partially refractory at rapid pacing, leading to a smaller release flux, by the next cycle the refractory RyR will have recovered sufficiently to have a larger release. [Qu et al., 2013] proposes a theory linking calcium alternans to subcellular models of calcium release. Their theory attributes cell-level cardiac alternans to subcellular instabilities in CRUs called *calcium sparks*. Their theory is called the ‘3R’ theory, as it states that it is the inherent randomness in the CRU, the recruitment of neighboring CRUs following a spark, and the refractoriness of CRUs combined, that leads to alternans.

3.8.3 Bidirectional Voltage-Calcium Coupling

Sarcolemmal ion channels and the intracellular calcium dynamics of the cell communicate through the cytosolic calcium concentration, which they both affect and are affected by. Thus there is a bidirectional coupling between membrane dynamics and intracellular calcium handling. Both voltage and calcium driven alternans will therefore in most cases lead to both APD- and CaT-alternans.

Membrane currents affect the intracellular calcium through $V \rightarrow \text{Ca}^{2+}$ coupling. This coupling occurs primarily through the magnitude of the L-type calcium current (LTCC) flux, which scales with the action potential duration. A larger LTCC flux leads to a larger cytosolic calcium concentration, which triggers a larger SR release through ryanodine receptors. The scaling of SR release on LTCC flux is known as *graded release*. The coupling $V \rightarrow \text{Ca}^{2+}$ is positive in the sense that a longer action potential yields a larger calcium transient.

Coupling in the opposite direction, $\text{Ca}^{2+} \rightarrow V$, consists primarily of two competing effects. Larger calcium release leads to higher cytosolic calcium concentration, which both inactivates L-type calcium channels (LTCC) and leads to larger sodium-calcium exchanger (NCX) activity. Inactivation of LTCC leads to a shorter action potential, and this coupling is therefore negative. The NCX, on the other hand, carries a net inward current. Increased activity due to a large CaT will prolong APD via sodium influx, giving positive coupling.

As voltage to calcium coupling is always positive, we expect voltage-driven alternans to always be electromechanically concordant, meaning APD and CaT alternate in phase with each other. Calcium to voltage coupling, on the other

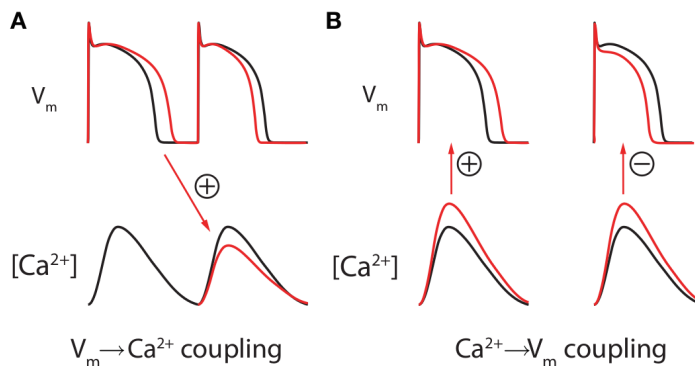


Figure 3.10: Coupling between sarcolemmal channel dynamics and intracellular calcium. **(A):** $V \rightarrow Ca^{2+}$ coupling is caused by longer APD leading to larger influx of calcium through L-type calcium channels, and subsequently larger calcium-induced calcium-release. **(B):** $Ca^{2+} \rightarrow V$ coupling. Higher cytosolic calcium concentrations lead to both larger NCX current and stronger calcium-inactivation of L-type calcium channels. The first effect prolongs APD, while the second shortens it, meaning this coupling can be both positive and negative. Figure taken from Figure 9 in [Gaeta and Christini, 2012].

hand, can be both positive and negative, depending on which underlying mechanism, LTCC or NCX, is stronger (See Figure 3.10). Calcium-driven alternans can therefore be electromechanically concordant or discordant, depending on cell type, ionic concentrations and so forth. This argument is supported by experiment, where only concordant voltage-driven alternans have been observed, while both concordant and discordant calcium-driven alternans have been observed ([Gaeta and Christini, 2012]).

While bidirectional coupling leads to simultaneous alternans in both APD and calcium, there is much dispute in which of the two systems the alternans ‘arise’. This is meant in the sense that alternans in one system precedes the other, and if stabilized will remove alternans in the other. This ‘chicken and egg’ dilemma of alternans have been important in the literature for the last 20 years. Historically, the restitution hypothesis of Nolesco and Dahlen was regarded the primary mechanism, while today more seem to regard calcium dynamics the primary cause of alternans ([Valdivia, 2015]). [Gaeta and Christini, 2012] argue that the dilemma itself is probably a false dichotomy *in situ*, and that there is no singular driving mechanism of cardiac alternans, instead invoking instabilities of the complete cellular system, involving continuous complex interplays between the two domains. The origin of cardiac alternans remains an open, and much debated, question in the scientific community.

Chapter 4

Conductance-based Models

To describe the time evolution of the membrane potential when a myocyte fires an action potential, we can use a mathematical model that describes how the conductances of sarcolemmal ion channels change over time. Such a model was first proposed by [Hodgkin and Huxley, 1952]. The model of Hodgkin and Huxley was based on a squid giant axon, a type of nerve cell. For their work, they received the *Nobel Prize in Physiology or Medicine* in 1963.

Although the Hodgkin-Huxley model describes a neuron and not a myocyte, the model is useful for describing any type of excitable cell. In this Chapter, we therefore present the Hodgkin-Huxley model as an example of a fairly simple conductance-based model. Next, we give a short review of the history of cardiac myocyte models, finishing with models for human atrial myocytes.

4.1 The Hodgkin-Huxley Model

The basis of the Hodgkin-Huxley (HH) model is to view the cell membrane as an electric circuit. The lipid bilayer can be seen as a capacitor, while the ion channels can be seen as resistors coupled in parallel with the capacitor. A circuit equivalent diagram of the cell membrane as described by the HH model is shown in Figure 4.1. From this circuit, the governing equation for the change in membrane potential can be written

$$C_m \frac{dV}{dt} = -(I_{Na} + I_K + I_L), \quad (4.1)$$

where C_m is the capacitance of the membrane, V the transmembrane potential, I_{Na} the current carried by Na^+ -ions passing through sodium channels in the membrane, I_K the current carried by K^+ -ions through potassium channels in the

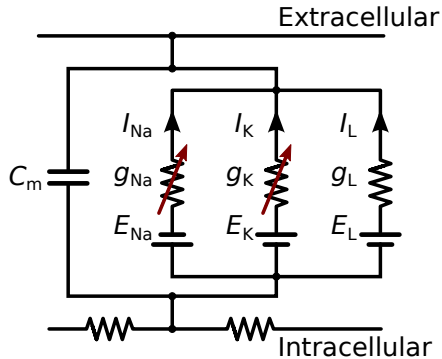


Figure 4.1: The circuit equivalent diagram of the Hodgkin-Huxley model, describing the time-evolution of the transmembrane potential. The sarcolemma is represented as a capacitor with capacitance C_m , the ion channels are represented as resistances coupled in parallel to the sarcolemma, with a conductance g_X and a driving potential E_X , given by the Nernst potential, this results in a current of ions I_X . In the HH model there are three currents included, $X = \text{Na}, \text{K}, \text{L}$, denoting a sodium, potassium and a non-specific leak current. The conductances of the Na^+ and K^+ currents change over time in response to the membrane potential, but the leak conductance is constant.

membrane, and I_L a non-ion specific leak current. The three currents are found using Ohm's law

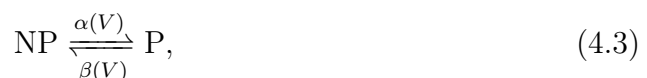
$$I_x = g_x(V - E_x), \quad \text{for } x = \text{Na}, \text{K}, \text{L}. \quad (4.2)$$

Where g_x is the conductance of the ion channel, and E_x the reversal potential of the current which is equivalent to the Nernst potential for the ion-specific channels.

So far, this is a fairly standard RC circuit. The essential component missing is the conductances' change over time to account for the opening and closing of the ion channels in the membrane. From the circuit equivalent diagram, we see that the leak conductance is assumed to be constant—but the sodium and potassium channel conductances are expected to change over time.

Gating Particles

To model the changing conductances of the channels, Hodgkin and Huxley introduced the concept of *gates* that could be in either a permissive (P) or a non-permissive (NP) state. A single channel could consist of several such gates, and would be considered open when all its gates were in the permissive state. The change of a gate between the two states can be described by a reaction equation



where the rate coefficients α and β are voltage dependent. If we let p denote the probability of a gate being in the permissive state, the first order kinetic equation gives its time evolution as

$$\frac{dp}{dt} = \alpha(V)(1 - p) - \beta(V)p. \quad (4.4)$$

The membrane of a single cell will contain a large number of individual ion channels, each with their own set of gates— p can therefore also be thought of as the *proportion* of all gates in the membrane being in the permissive state.

To make the behavior of individual gates more explicit, it can be useful to rewrite Equation 4.4. Writing it out gives

$$\frac{dp}{dt} = \alpha - (\alpha + \beta)p. \quad (4.5)$$

For any values of α and β , p has a steady-state value p_∞ where the system is in equilibrium, given by

$$\frac{dp}{dt} = \alpha - (\alpha + \beta)p_\infty = 0 \Rightarrow p_\infty = \frac{\alpha}{\alpha + \beta}. \quad (4.6)$$

Defining $\tau = (\alpha + \beta)^{-1}$ lets us write Equation 4.5 as

$$\frac{dp}{dt} = \frac{p_\infty - p}{\tau}. \quad (4.7)$$

Under *voltage-clamp* conditions, meaning the voltage V is kept constant, α and β (and by extension p_∞ and τ) are constant in time, meaning this differential equation has a simple solution

$$p(t) = p_\infty - (p_\infty - p_0)e^{-t/\tau}. \quad (4.8)$$

Under voltage clamp conditions, p will decay exponentially to its equilibrium, or steady-state, value with a time constant τ . Normally, the membrane voltage changes over time, giving changes in the rate coefficients and consequently in the steady-states and time constants of the gates. The steady-state and time constants are therefore best defined as functions of V , which we can call the “activation parameters” of the gates.

Different ion channels will have different types of gates, and some channels will be built up of gates of different types, with each type having its own activation parameters. In the HH model, three types of gates are included, called m , n and h . The proportion of each type of gate that is permissive will change independently of the other gates, therefore three differential equations are needed to describe their change over time

$$\frac{dx}{dt} = \frac{x_\infty - x}{\tau_x}, \quad \text{for } x = m, n, h. \quad (4.9)$$

The activation parameters of the three gate types are shown in Figure 4.2. From the steady-state values shown in Figure 4.2a, we see that the m and n gates become more likely to be permissive as V increases, while the h gate becomes less likely to be permissive. Due to this it is common to refer to m and n as *activation* gates, and h as an *inactivation* gate, as this describes their behavior in response to the depolarization of the membrane following an action potential.

A single sodium channel uses three m gates and single h gate, all of which need to be in the permissive state for the channel to be open. If we assume all gates to act independently, the total membrane sodium conductance will be given as

$$g_{\text{Na}} = \bar{g}_{\text{Na}} m^3 h, \quad (4.10)$$

where \bar{g}_{Na} is the theoretical maximal conductance of the membrane if all sodium channels were open simultaneously. As m and h are both numbers in the range $[0, 1]$, the membrane sodium conductance will be in the range $[0, \bar{g}_{\text{Na}}]$, depending on how many gates are open. The potassium channel is built up of four independent n gates, meaning the conductance is given by

$$g_{\text{K}} = \bar{g}_{\text{K}} n^4. \quad (4.11)$$

It is the interplay between the steady-state values and time constants that allow the HH model to generate action potentials. At rest V is around -80 mV and so the steady-state of the m gate is almost 0 (see Fig. 4.2a). Following a small external stimulus, V is increased slightly, causing an increase in the steady-state of the m gate. This allows the sodium conductance to increase and a sodium current through the membrane is established. This sodium current further depolarizes the membrane potential, pushing the steady-state of the m gate and the sodium conductance even further. This positive feedback loop rapidly causes a large sodium flux into the cell leading to the upstroke of the action potential. As the membrane potential depolarizes, the h gate will start to become non-permissive, leading to inactivation of the sodium channel, cutting off the sodium current. The peak of the action potential in the HH model is around 40 mV, high above the range where the h gate becomes non-permissive. This can be understood from the time constants of the two gates (see Fig. 4.2b). The h gate has a higher time constant than the m gate, meaning the channel activates faster than it inactivates. This allows the sodium channel to overshoot the potential where the steady-state inactivates, as it takes a few milliseconds for the h gate to kick in.

In summary, the Hodgkin-Huxley model treats the cell membrane as a simple electric circuit where ion channels are coupled in parallel with a capacitor. The change in ion channel conductances over time is described by the change in states of underlying channel gates. The HH model is a set of four coupled ordinary

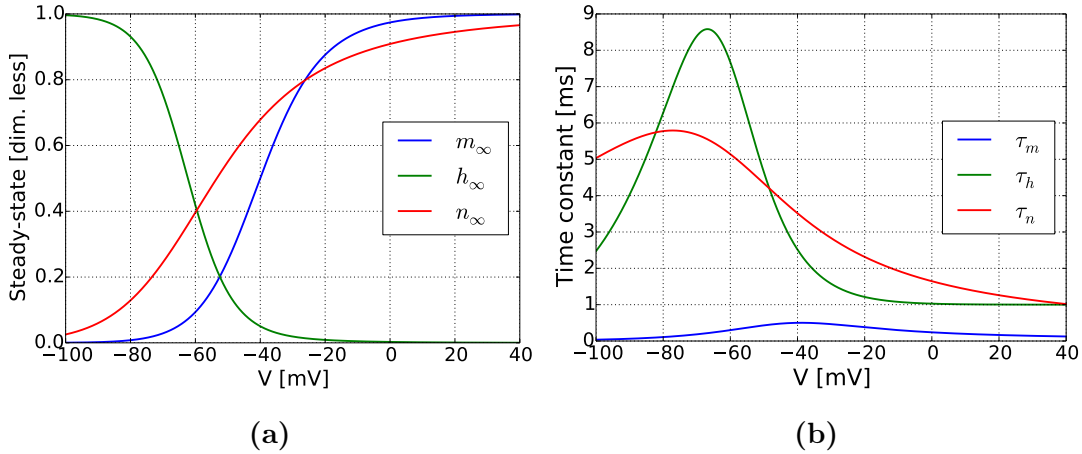


Figure 4.2: Activation parameters of the gating particles in the Hodgkin-Huxley model. At a given membrane potential, the proportion of permissive gates will decay exponentially towards its steady-state value (a) with a given time constant (b), both changing as functions of the membrane potential.

differential equations, one for the evolution of the membrane potential, and three for the evolution of the gates. The model is the first, and a classic example of a *conductance-based model*, as most of the work goes into describing how the ion channel conductances change over time.

4.2 Models for the Human Atrial Myocyte

The Hodgkin-Huxley model describes a nerve cell and still sees frequent use in neuroscience, often in modified or extended forms. The formalism of conductance-based models is, however, extremely useful in describing all excitable cells, including cardiomyocytes.

The first model to explicitly focus on cardiac cells followed ten years after HH, in [Noble, 1962], with the title “*A modification to the Hodgkin-Huxley equations*”. Noble showed that conductance-based models could also describe the longer-lasting action potentials and self-excitatory activity of Purkinje fibers, specialized cardiac cells. Fifteen years after Noble, the first mathematical model of a mammalian ventricular cardiomyocyte was proposed in [Beeler and Reuter, 1977]. The Beeler-Reuter model consists of 8 differential equations, twice that of the HH model.

Due to lack of experimental data, most of the early cell models are based on data gathered from mammals other than humans, such as guinea pigs, rabbits and dogs. The first model for the *human* ventricular myocyte wasn’t published until

1998, in [Priebe and Beuckelmann, 1998]. The model of Priebe and Beuckelmann was based on the earlier Luo-Rudy II model, which was again based on guinea pig. The first models of the *human atrial myocyte* (hAM) were published in the same year. Two models were proposed in [Nygren et al., 1998] and [Courtemanche et al., 1998]. The Courtemanche model was, like the Priebe-Beuckelmann, based on the Luo-Rudy II for the guinea pig ventricular myocyte. The Nygren model was instead based on an earlier model for the rabbit atrial myocyte, developed by the same group.

In more recent years, three more models for the hAM have been proposed. In 2008 and 2011 two models based on the Nygren model were published—[Maleckar et al., 2009b] and [Koivumäki et al., 2011]. In 2011 another model was proposed, this one not based on any of the preceding, [Grandi et al., 2011]. At the time of writing of this thesis, there are thus mainly five different proposed conductance-based models for the hAM:

- The Courtemanche Model
- The Nygren Model
- The Maleckar Model
- The Koivumäki Model
- The Grandi Model

All of these models are used in conjunction with experiments to study atrial myocytes and are found regularly in the literature. They have also all been adjusted since their original publications.

All five models listed here are significantly more complex than the Hodgkin-Huxley model presented in the last Section, but they are based on the same conductance-based formalism. The higher complexity is mainly due to inclusion of more types of ion channels as well as ion channels being dependent on ion concentrations in addition to the membrane potential—necessitating keeping track of different ion concentrations.

Table 4.1 is adapted from [Dössel et al., 2012] and gives an overview of what ion channels are included in the models, as well as what calcium compartments are used, important for the internal calcium dynamics of the cell model. From the Table, we see that all models have a common set of nine sarcolemmal ion channels and three exchangers and pumps. These twelve common currents are the ones known to be most important for the action potential morphology of human atrial myocytes, but there are many other channels known to be present in lesser extent or known to be present, but not highly active. While these smaller channels are less important for the action potential morphology, they can be very impactful under conditions in certain specific studies—this explains why

the different models each include different currents in addition to the common set.

The Grandi and Koivumäki models include the largest number of ion channels. In addition, to the common currents, both models include the acetylcholine activated potassium channel I_{KACh} , important for parasympathetic regulation of the heart rate from the central nervous system. In addition the Grandi model contains two chloride channels, which none of the other models include, while the Koivumäki model includes the small-conductance calcium-activated potassium (SK) channel and the hyperpolarization-activated funny current.

In addition to the differences in sarcolemmal currents, there are large differences in the number of different spatial calcium compartments used. The Courtemanche model only has a single compartment for intracellular calcium, while the Koivumäki model includes a subsarcolemmal space in addition to four spatial intracellular compartments. Each of these compartments have their own portion of the SR, and the amount of calcium bound to SERCA is also tracked for each compartment, leading to a total of 13 state variables for calcium.

The Koivumäki model was first produced to study the effects of intracellular calcium release on the action potential shape ([[Koivumäki et al., 2011](#)]), and its detailed description of intracellular calcium dynamics is the main reason we have chosen to work with this model. As we are interested in studying the bidirectional coupling of membrane and intracellular dynamics important for alternans the Koivumäki model seems like the best choice of the five, due to its detailed representation of intracellular calcium.

For a more thorough review of what the different hAM models are based on and how they are formulated, the original five papers are extremely useful. For comparisons between the five models the benchmarking paper [[Wilhelms et al., 2012](#)] gives a detailed description, while [[Dössel et al., 2012](#)] gives a more succinct review.

4.3 Alternans in hAM Models

The benchmarking paper [[Wilhelms et al., 2012](#)] compared the five hAM models on their ability to produce different electrophysiological phenomena, like alternans. To see if the models exhibited action potential duration (APD)-alternans they produced restitution curves for the five models showing how the APD changed as the pacing rate was increased. If APD alternans arise as the pacing rate is increased, the restitution curve for that model will split into two to reflect the different APDs measured at the same cycle length. Figure 4.3a shows the APD restitution plot of the models from the paper. They also looked at how

Table 4.1: Overview of membrane currents and spatial calcium compartments included in the different hAM models. Table adapted from table 2 in [Dössel et al., 2012].

Model	Included Currents	Calcium compartments
Courtemanche	Common currents	Intracellular, extracellular
Nygren	Common currents	Intracellular, extracellular, dyadic cleft, cleft space
Maleckar	Common currents + I_{KAch}	Intracellular, extracellular, dyadic cleft, cleft space
Grandi	Common currents + I_{KAch} + $I_{Cl,b}$ + $I_{Cl,Ca}$	Intracellular, extracellular, dyadic cleft, subsarcolemmal
Koivumäki	Common currents + I_f + I_{KAch} + I_{KCa}	4 intracellular compartments, extracellular, subsarcolemmal

The currents common to all models are: Fast sodium current I_{Na} . L-type calcium channel, I_{CaL} . Transient outward current, I_{to} . Slow, rapid, and ultrarapid delayed rectifier potassium currents, I_{Ks} , I_{Kr} and I_{Kur} . Inward rectifier potassium current, I_{K1} . Sodium and calcium background currents, $I_{Na,b}$ and $I_{Ca,b}$. Sodium-calcium exchanger, I_{NaCa} . Sodium-potassium pump, I_{NaK} . Calcium pump, $I_{Ca,p}$.

The cleft space is a small region of the extracellular space where depletion and accumulation of ions takes place, it communicates diffusively with the extracellular space, where all concentrations are constant—for details see [Nygren et al., 1998]. The subsarcolemmal space or simply subspace is a small space just beneath the cell membrane where concentrations change more drastically. The dyadic cleft is the portion of the subspace where L-type calcium channels face opposing ryanodine receptors, forming effective couplon units responsible for CICR. Only the Grandi model distinguishes between the dyadic cleft and the subspace, while the Nygren-lineage models (N, M, K) do not make any distinction between the two.

the calcium transients of the model differed by plotting the intracellular calcium concentrations over 1 second at a cycle length of 250 ms, i.e., for four cardiac cycles. Figure 4.3b shows the calcium transients of the five models from the paper.

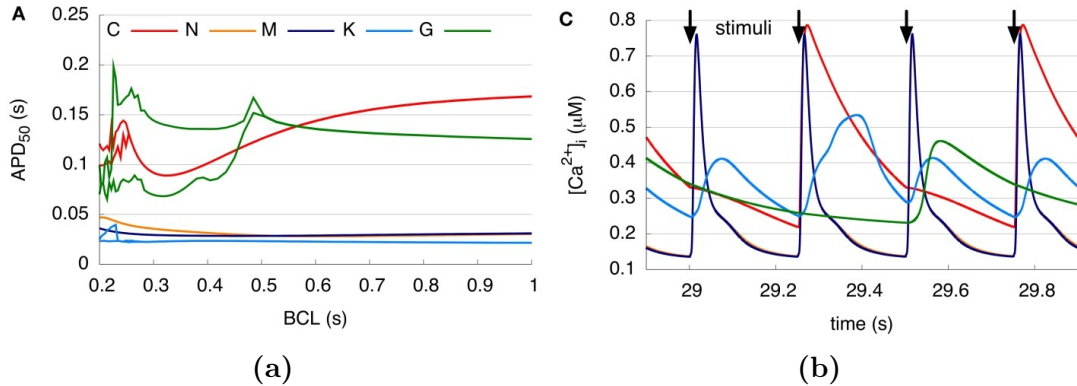


Figure 4.3: Alternans in the five models of the hAM. (a) APD₅₀ is the duration from the upstroke of the action potential to it is 50 % repolarized, i.e., half-way back to rest. The APD is measured after 30 seconds of pacing at cycle lengths between 200 and 1000 ms. (b) Calcium transients for four consecutive beats of the models when paced at 250 ms, the measured calcium transients are of the final second of the 30 second pacing period at a given cycle length before the APD₅₀ was measured. Figures taken from Figure 3 in [Wilhelms et al., 2012], and used under a CC by 3.0 license, see [Creative Commons, 2007] for details.

From the results of Wilhelms et al we see that the Nygren (N) and Maleckar (M) models don't exhibit any APD-alternans for any cycle length with the pacing regime used. The Koivumäki (K) and Courtemanche (C) models exhibits relatively small APD-alternans for cycle length of below roughly 250 ms. The Grandi (G) model shows much larger APD-alternans at a cycle lengths below 500 ms, roughly double that of the K and C models.

For CaT-transients, the Nygren and Maleckar models again exhibit no alternans. The Koivumäki model has a period-3 alternating pattern in its CaT-transient with peaks of about double amplitude every third beat. The Courtemanche model has large beat-to-beat variations, as every other beat has a very rapid and large increase in calcium, combined with no increase the other beat, leading to a very long decay time for the calcium. The Nygren model has a similar behavior, having a spike every third beat and then a gradual decay back with no calcium release for the next two cycles. Overall the Koivumäki and Grandi models are seen to have considerably lower amplitudes and peaks in their calcium transients compared to the Courtemanche, Nygren and Maleckar models.

As the work of Wilhelms et al was published in 2012, it is the original formulation

of the Koivumäki model which has been benchmarked. However, the model has been reformulated in both 2014 and 2015. The alternans behavior of these model variations have not been examined in the literature. We will look at the alternans behavior of both these model variants, using the same approach as Wilhelms et al, which we will return to and outline in Chapter 8.

Chapter 5

The Koivumäki Model

The Koivumäki model (K model) was first presented in [Koivumäki et al., 2011] and is based mostly on the Nygren model, presented in [Nygren et al., 1998]. The Koivumäki paper refers much to the Nygren paper on which it is based, so starting at the Nygren model is recommended for those who want to understand the Koivumäki model in detail. The model received modifications in [Koivumäki et al., 2014] and underwent further alterations in 2015. The newest model formulation has yet to be included in publication, instead we have received them directly from the original authors of the model.

In this Chapter, we will go through the most recent model formulation, the 2015 variant, in detail. We show both the mathematical expressions used in the model, as well as tabulate the parameters used. Although it surely would be helpful to the reader to understand both the differences between the model variants as well as the origin of all expressions, we are working with limited space.

The reason we focus on the 2015 variant is twofold. Firstly, the 2015 variant is the most up-to-date formulation, relying on the most recent experimental data. Secondly, as this formulation is unpublished, this thesis can hopefully act as documentation for anyone aiming to use the Koivumäki model for computational studies.

This Chapter is divided into three main sections. First, we look at the geometry of the system and the general assumptions about the myocyte and its surroundings. Next, we go through the different sarcolemmal ion channels included in the model. Finally, we turn to the intracellular dynamics of the cell, which are mainly related to calcium. To describe the intracellular dynamics, we cover how buffering and diffusion of ions are modeled, as well as the time evolution of different ionic species in the model.

Unless a source is otherwise stated, any mathematical formulation of parameter

is taken from either [Nygren et al., 1998], which presents the Nygren model, [Koivumäki et al., 2011]/[Koivumäki et al., 2014], which present the 2011/2014 formulations of the Koivumäki model or directly from the authors' original MATLAB implementation of the model, for the 2015 model formulation. Please note that both Koivumäki papers have supplementary material that goes into detail on the mathematical formulation of the model.

Note that physiological myocyte models, such as the Koivumäki model, include a large number of state variables and parameters. The formulation of each individual component of the model, such as the different ion channels, will be constrained by their own set of experiments. It is therefore helpful to think of these models as being built of modular components. These components are often adapted from different sources and models, as will become apparent when we go through the model.

A diagram of the model and its different currents is shown in Figure 5.1 on the following page.

5.1 Cell Geometry

The atrial myocyte is modeled as a cylinder of length l_{cell} . Just beneath the cell membrane is the junctional cytosol or subsarcolemmal space (ss); beyond the subsarcolemmal space is the non-junctional or bulk cytosol. The radius of the bulk cytosol is r_{junct} , and the volume of the bulk cytosol is

$$V_{\text{bulk}} = \pi r_{\text{junct}}^2 \cdot l_{\text{cell}}, \quad (5.1)$$

and the total cytosolic volume is given as

$$V_{\text{cytosol}} = V_{\text{ss}} + V_{\text{bulk}}, \quad (5.2)$$

where V_{ss} is the total volume of the subspace.

For potassium, the whole cytosol is considered isoconcentrational and no compartmental distinction is made. For sodium, we only distinguish between the subspace concentration and the bulk cytosol concentration. For calcium, a higher spatial resolution is used, dividing the bulk cytosol into four compartments in the shape of cylindrical shells wrapped around each other. The sarcoplasmic reticulum (SR) is spread evenly throughout the bulk cytosol, and each compartment will contain part of the SR, with its own set of SR membrane currents.

Dividing the non-junctional cytosol into N cylindrical shells of equal width means the compartments have outer radii of

$$r_n = n\Delta r, \quad \text{for } n = 1, \dots, N, \quad \Delta r = \frac{r_{\text{junct}}}{N}. \quad (5.3)$$

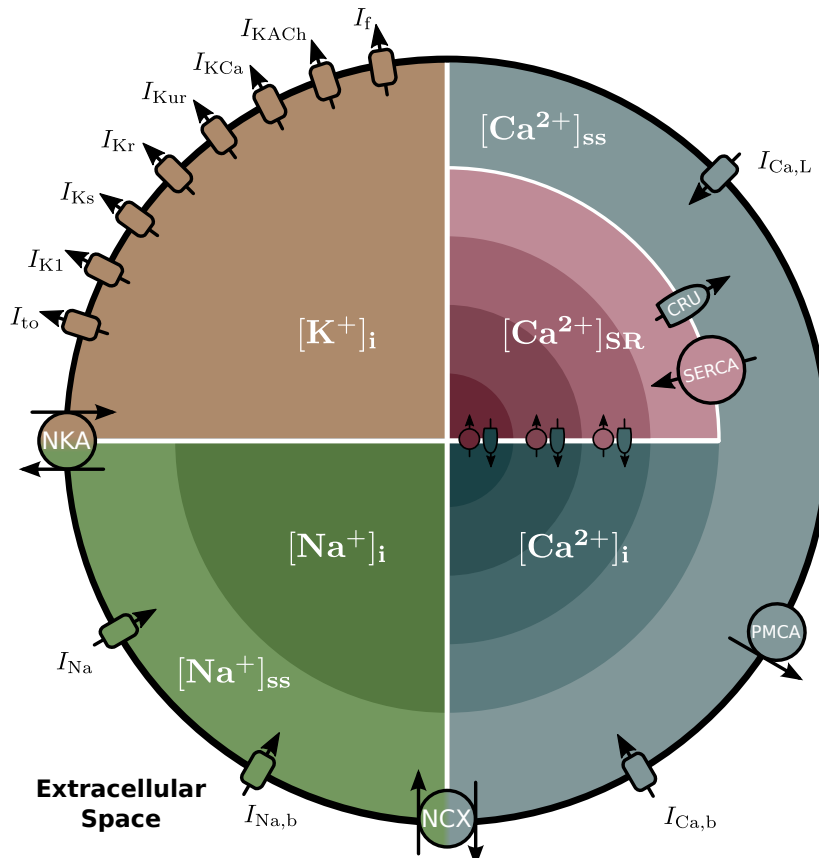


Figure 5.1: Overview of compartments and currents included in the 2015 Koivumäki model. Concentrations of three specific ionic species are tracked inside the cell: potassium, calcium and sodium. The cell contains a single compartment for potassium and two compartments for sodium. There are in total 9 compartments for calcium, excluding calcium bound to the four SERCA pumps. Calcium can freely diffuse between compartments within the sarcoplasmic reticulum and cytosol, but cannot cross between the two. Sodium also diffuses freely between the junctional and non-junctional cytosolic compartments. Sizes of compartments and currents in the Figure are for illustration only and do not reflect their volume or magnitude in the model. Figure inspired by Fig. 1A in [Koivumäki et al., 2014].

Where the numbering of compartments starts at the center and increases outward. Each compartment has a volume of

$$V_n = \pi r_n^2 l_{\text{cell}} - \pi r_{n-1}^2 l_{\text{cell}} = (2n - 1)\pi \Delta r^2 l_{\text{cell}} = (2n - 1)V_1. \quad (5.4)$$

The SR is assumed to occupy 2.25 % of the total cytosolic volume, evenly distributed among the cytosolic compartments. This gives the SR compartments' volumes:

$$V_{\text{SR},n} = 0.225V_n. \quad (5.5)$$

As the cytosol contains many structures and organelles, we consider only 50 % of the total volume to be transport-available; the same is assumed of the SR volume.

Table 5.1: Cell geometry parameters

Parameter	Description	Value
r_{junct}	Radius of bulk cytosol	6.5 μm
l_{cell}	Length of cell	122.051 μm
N	Number of bulk cytosol Ca compartments	4
Δr	Width of bulk cytosol compartments	1.625 μm
V_{ss}	Volume of subspace	$4.99232 \cdot 10^{-5}$ nL

5.2 Membrane Currents

As in the Hodgkin-Huxley model, the membrane is modeled as a capacitor coupled in parallel with conductances representing the membrane ion channels,

$$C_m \frac{dV}{dt} = -(I_{\text{ion}} + I_{\text{stim}}). \quad (5.6)$$

Here I_{ion} is the sum of all the different membrane ion currents shown in Figure 5.1 and I_{stim} is an external stimulus current.

Passive transport of ions through membrane channels are found through the species Nernst-Potential, defined as

$$E_X = \frac{RT}{Fz_X} \ln \frac{[X]_o}{[X]_i}, \quad \text{for } X = \text{Na, K, Ca.} \quad (5.7)$$

The extracellular concentrations $[X]_o$ are assumed to be constant in time, while the intracellular concentrations change over time and are therefore state variables, rather than parameters. For sodium and calcium, it is the subsarcolemmal

concentration that will decide the Nernst potential, rather than the concentration in the bulk cytosol.

The temperature of the Nygren model is 33°C. The Koivumäki model used this temperature for its 2011 and 2014 formulations but temperature scaling has been used to increase the 2015 model variant temperature to human body temperature, i.e., 37°C.

Table 5.2: General membrane current parameters

Parameter	Definition	Value
C_m	Cell membrane capacitance	0.05 nF
F	Faraday constant	96478 C/mol
R	Ideal gas constant	8314 mJ/(mol K)
T	System temperature	310.15 K
$[Na^+]_o$	Extracellular Na ⁺ concentration	130 mM
$[K^+]_o$	Extracellular K ⁺ concentration	5.4 mM
$[Ca^{2+}]_o$	Extracellular Ca ²⁺ concentration	1.8 mM

The Sodium Channel

The sodium channel, I_{Na} , quickly activates in response to an increase in membrane potential, leading to a large influx of sodium, responsible for the upstroke of the action potential. The channel quickly becomes inactivated and the I_{Na} current therefore mainly consists of a high-amplitude, narrow spike. However, the channel doesn't inactivate completely and there is therefore a much smaller 'late' component to the sodium current that remains active for most of the action potential. The total sodium current can be expressed as the sum of the fast and late components,

$$I_{\text{Na}} = I_{\text{Na,F}} + I_{\text{Na,L}}. \quad (5.8)$$

The Nygren model accounted for these components of the sodium current by letting the main inactivation gate be the sum of two subgates

$$h = \frac{9}{10}h_1 + \frac{1}{10}h_2, \quad (5.9)$$

where the mainly contributing gate, h_1 , has a much shorter time constant than the smaller contributing h_2 -gate. The late component therefore has a magnitude that is 10 % of the magnitude of the fast component.

The K model originally used the Nygren sodium channel implementation, but one of the biggest modifications of the 2015 variant is a complete reformulation of this channel, based on new experimental results. In the newer model, the current itself is explicitly split into two contributions. The two components are formulated as

$$I_{\text{Na,F}} = \bar{g}_{\text{Na}} \cdot m^3 \cdot h_1 \cdot h_2 \cdot (V - E_{\text{Na}}), \quad (5.10)$$

$$I_{\text{Na,L}} = \bar{g}_{\text{Na,L}} \cdot m^3 \cdot f_1 \cdot (V - E_{\text{Na}}), \quad (5.11)$$

where $\bar{g}_{\text{Na}} \gg \bar{g}_{\text{Na,L}}$. Here m is the activation gate responsible for both current components, while h_1 and h_2 are inactivation gates for the fast component, while f_1 an inactivation gate for the late component. Most voltage-dependent gates in the model are sigmoid functions of V in their steady-states, which for a general gate x can be expressed as

$$x_\infty = \left(1 + \exp\left[-\frac{V-V_{1/2}}{s}\right]\right)^{-1}. \quad (5.12)$$

Here $V_{1/2}$ is the time where the steady-state of the gate is 0.5, which is often referred to as the *center*, or *time of maximum growth*, for a sigmoid function. The parameter s is the *scale* of the sigmoid function, and decides the growth rate. If s is positive, the sigmoid function is an increasing function in V and corresponds to an activation gate. If s is negative, the sigmoid function is decreasing in V and the gate is an inactivation gate.

For the gates of the sodium channel, the steady-states are expressed as

$$m_\infty = \left(1 + \exp\left[-\frac{V+39 \text{ mV}}{7.2 \text{ mV}}\right]\right)^{-1}, \quad (5.13)$$

$$h_\infty = \left(1 + \exp\left[\frac{V+67 \text{ mV}}{6.0 \text{ mV}}\right]\right)^{-1}, \quad (5.14)$$

$$f_{1,\infty} = \left(1 + \exp\left[\frac{V+72 \text{ mV}}{5.1 \text{ mV}}\right]\right)^{-1}, \quad (5.15)$$

where h_∞ describes both h_1 and h_2 . The time constants are

$$\tau_m [\text{ms}] = 0.01 + 0.13 \exp\left[-\left(\frac{V+48 \text{ mV}}{15 \text{ mV}}\right)^2\right] + 0.045 \left(1 + \exp\left[-\frac{V+42 \text{ mV}}{5 \text{ mV}}\right]\right)^{-1} \quad (5.16)$$

$$\begin{aligned} \tau_{h_1} [\text{ms}] = 0.07 + 34 & \left(1 + \exp\left[\frac{V+41 \text{ mV}}{5.5 \text{ mV}}\right]\right)^{-1} + 0.2 \left(1 + \exp\left[-\frac{V+79 \text{ mV}}{14 \text{ mV}}\right]\right)^{-1} \\ & + \exp\left[-\frac{V+41 \text{ mV}}{14 \text{ mV}}\right] \end{aligned} \quad (5.17)$$

$$\begin{aligned} \tau_{h_2} [\text{ms}] = 0.7 + 150 & \left(1 + \exp\left[\frac{V+41}{5.5}\right]\right)^{-1} + 2 \left(1 + \exp\left[-\frac{V+79}{14}\right]\right)^{-1} \\ & + \exp\left[-\frac{V+41}{14}\right] \end{aligned} \quad (5.18)$$

$$\tau_{f_1} [\text{ms}] = 200 \quad (5.19)$$

The new sodium channel formulation increases the excitability of the cell by lowering the threshold for firing an action potential. This means a smaller stimulus current is needed to trigger an action potential in the 2015 formulation than in the earlier models, reflecting newly available experimental data.

Background currents

Background currents are currents with a small and constant conductance, much like the leak current of the Hodgkin-Huxley model. Due to their low conductances, they are more impactful during diastole than during the action potential and will affect the resting membrane potential of the cell. The Nygren model includes two background currents, one for sodium and one for calcium. Both are modeled as Ohmic currents. The Koivumäki model include these Ohmic background currents, with the conductance of $I_{\text{Ca,b}}$ slightly upregulated, to increase SR load. The currents are given as

$$I_{\text{Na,b}} = \bar{g}_{\text{Na,b}} \cdot (V - E_{\text{Na}}), \quad (5.20)$$

$$I_{\text{Ca,b}} = \bar{g}_{\text{Ca,b}} \cdot (V - E_{\text{Ca}}). \quad (5.21)$$

The L-type Calcium Channel

The long-lasting calcium channel (L-type, LTCC) opens at higher rates of depolarization than the sodium current and will therefore activate after the sodium

Table 5.3: Membrane sodium channel parameters

Parameter	Definition	Value
\bar{g}_{Na}	Max I_{Na} conductance	0.558 μS
$\bar{g}_{\text{Na,L}}$	Max conductance of late Na^+ current	0.423 nS
$\bar{g}_{\text{Na,b}}$	Max $I_{\text{Na,b}}$ conductance	0.060599 nS

current has created the upstroke of the action potential. The LTCC current, $I_{\text{Ca,L}}$, is therefore also known as the slow inward current. The calcium influx through the LTCC is crucial in triggering calcium-induced calcium-release from the SR and is the main connection between the sarcolemmal ion channels of the cell and its internal calcium dynamics.

Experiments have shown that the reversal potential of the L-type Ca^{2+} current is lower than predicted by the Nernst potential. Based on [Campbell et al., 1988], the *apparent* reversal potential of $I_{\text{Ca,L}}$ is formulated as

$$E_{\text{Ca,app}} \text{ [mV]} = 60 + 29.2 \log_{10} \frac{[\text{Ca}^{2+}]_o}{1.8 \text{ mM}}. \quad (5.22)$$

The different hAM models have different L-type calcium channel formulations. Experimental measures have shown the LTCC to become more inactivated when the cytosolic calcium levels are higher. In the Nygren model, this calcium-inactivation is modeled through two separate voltage-dependent inactivation gates, one fast and one slow. Because $I_{\text{Ca,L}}$ becomes inactivated at voltages slightly higher than 0 mV, Nygren et al let a fraction of all L-type channels depend on the fast voltage-inactivation gating. This fraction, denoted f_{Ca} , was a monotonic function of the subsarcolemmal calcium concentration. The L-type Ca^{2+} current in the Nygren model is given as

$$I_{\text{Ca,L}} = \bar{g}_{\text{Ca,L}} \cdot d_L \cdot [f_{\text{Ca}} f_{L,1} + (1 - f_{\text{Ca}}) f_{L,2}] (V - E_{\text{Ca,app}}), \quad (5.23)$$

where d_L is a voltage-activated gate, while $f_{L,1}$ and $f_{L,2}$ are the fast and slow voltage-inactivation gates respectively.

The 2011 Koivumäki model used the Nygren formulation for the LTCC, but reformulated it in the 2014 variant. The fast inactivation gate was removed completely, and the dependence on cytosolic calcium concentration modeled directly. This leads to a tighter Ca^{2+} -vs.-voltage dependent inactivation that is more similar to the L-type current formulation used in the Courtemanche model. The remaining voltage-inactivated gate has been sped up, based on new *in vitro* experimental data, and the activation time constant has been reduced to one fourth of the original. For a detailed description of these changes see the supplementary

material of [Koivumäki et al., 2014]. In the K model, the L-type Ca^{2+} current is formulated as

$$I_{\text{Ca,L}} = \bar{g}_{\text{Ca,L}} \cdot d_L \cdot f_L \cdot f_{\text{Ca}} \cdot (V - E_{\text{Ca,app}}), \quad (5.24)$$

where f_{Ca} is now a calcium-dependent inactivation gate, which is governed by an ODE as for voltage-dependent gates.

The steady-states are given by

$$d_{L,\infty} = \left(1 + \exp\left[-\frac{V+9.5 \text{ mV}}{6.9 \text{ mV}}\right]\right)^{-1}, \quad (5.25)$$

$$f_{L,\infty} = 0.04 + 0.96\left(1 + \exp\left[\frac{V+25.5 \text{ mV}}{8.4 \text{ mV}}\right]\right)^{-1} + \left(1 + \exp\left[-\frac{V-60 \text{ mV}}{8 \text{ mV}}\right]\right)^{-1}, \quad (5.26)$$

$$f_{\text{Ca},\infty} = \left(1 + \frac{[\text{Ca}^{2+}]_{\text{ss}}}{k_{\text{Ca}}}\right)^{-1}. \quad (5.27)$$

Here the last equation is known as the *Hill equation*, which describes the binding of ligands to receptors, in this case the binding of Ca^{2+} to the LTCC to inactivate it. In this case, the Hill coefficient is one, indicating *independent binding* of Ca^{2+} to the LTCC to inactivate it, meaning the binding ratio is independent of how much calcium is already bound to the receptor. The parameter k_{Ca} is the dissociation constant of the binding reaction, corresponding to the calcium concentration for which the fraction of calcium inactivated gates will be 0.5.

The time constants are

$$\tau_d [\text{ms}] = 0.5 + 0.65 \exp\left[-\left(\frac{V+35 \text{ mV}}{30 \text{ mV}}\right)^2\right], \quad (5.28)$$

$$\tau_f [\text{ms}] = 40 + 1340 \exp\left[-\left(\frac{V+40 \text{ mV}}{14.2 \text{ mV}}\right)^2\right], \quad (5.29)$$

$$\tau_{f_{\text{Ca}}} [\text{ms}] = 2. \quad (5.30)$$

Transient Outward Current

The transient outward current, I_{to} , activates rapidly at high voltages and is responsible for the early repolarization leading to the ‘notch’ of the action potential. The reason for the name is that the *transient* outward current is short-lasting and quickly deactivates. The Koivumäki model follows the Nygren formulation of I_{to} where it is modeled as a single potassium current with a single activation

Table 5.4: Membrane calcium channel parameters

Parameter	Definition	Value
$\bar{g}_{\text{Ca,L}}$	Max $I_{\text{Ca,L}}$ conductance	0.007 μS
$\bar{g}_{\text{Ca,b}}$	Max $I_{\text{Ca,b}}$ conductance	0.084 nS
k_{Ca}	Half-max binding conc. of V inactivation	0.6 μM

and a single inactivation gate. The I_{to} conductance has been upregulated in the 2015, leading to a stronger notch in the AP. The current is given by

$$I_{\text{to}} = \bar{g}_t \cdot r_t \cdot s_t \cdot (V - E_K), \quad (5.31)$$

where r_t and s_t is an activation and inactivation gate.

The steady-states of the channel are as in the Nygren formulation, but have been scaled with the temperature of the system. This scaling is done using a *Q10 temperature coefficient* of 2.6, meaning the transition rates of the channel are scaled by 2.6 for every 10 K the temperature of the system is increased. Such temperature scaling is commonly used in cell models, as much of the experimental channel data come from *in vitro* studies carried out at temperatures lower than those found *in vivo*. After temperature scaling, the steady-states are:

$$r_{t,\infty} = \left(1 + \exp\left[-\frac{V-1 \text{ mV}}{11 \text{ mV}}\right]\right)^{-1}, \quad (5.32)$$

$$s_{t,\infty} = \left(1 + \exp\left[\frac{V+40.5 \text{ mV}}{11.5 \text{ mV}}\right]\right)^{-1}. \quad (5.33)$$

The time constant for the activation gate is as in Nygren, but for the inactivation gate it has been altered to follow the changes made in the Maleckar model ([Maleckar et al., 2009b]), which is also based on the Nygren model. The I_{to} formulation of Nygren et al was based on experimental data from rabbit atrial cells, which have a much longer time of recovery from inactivation in the I_{to} than humans. The formulation of Maleckar et. al. better catches the rapid recovery from inactivation found in humans. The time constants are

$$\tau_{r_t} [\text{ms}] = 1 + 2.4 \exp\left[-\left(\frac{V}{30 \text{ mV}}\right)^2\right], \quad (5.34)$$

$$\tau_{s_t} [\text{ms}] = 9.6 + 18 \exp\left[-\left(\frac{V+52.45 \text{ mV}}{15.88 \text{ mV}}\right)^2\right]. \quad (5.35)$$

Delayed Outward Rectifier Potassium Currents

There are three potassium currents that are mainly responsible for the late repolarization of the action potential. These are known as the delayed outward rectifier currents as their activation is *delayed*, relative to the upstroke of the AP. The three channels are separated by their speed of activation and called the slow, rapid and ultrarapid delayed rectifier currents, denoted I_{Ks} , I_{Kr} , and I_{Kur} . The ultrarapid rectifier current is not present in ventricular myocytes and is the main reason for the large differences in ventricular and atrial action potential duration and shape.

When the Nygren model was developed, the ultrarapid rectifier current wasn't well-known and the effects of the channel was included through a sustained outward K^+ current called I_{sus} . The sustained outward current included a partial

inactivation. Newer experimental results revealed the sustained outward current to be carried by the ultrarapid rectifier current. Using these results, Maleckar et al formulated a model for I_{Kur} , which is also used in the K model.

The three delayed rectifier K^+ currents are given as

$$I_{\text{Kr}} = \bar{g}_{\text{Kr}} \cdot \sqrt{\frac{[\text{K}^+]_o}{5.4 \text{ mM}}} \cdot p_a \cdot p_i \cdot (V - E_K), \quad (5.36)$$

$$I_{\text{Ks}} = \bar{g}_{\text{Ks}} \cdot n^2 \cdot (V - E_K), \quad (5.37)$$

$$I_{\text{Kur}} = \bar{g}_{\text{Kur}} \cdot r \cdot s \cdot (V - E_K). \quad (5.38)$$

Here n , p_a and r are activation gates, while p_i and s are inactivation gates—however, unlike the other gates p_i is assumed to always be at its equilibrium value and thus is not represented by an ODE, but is simply an explicit function of V . Here the expressions for I_{Kr} and I_{Ks} are as in the Nygren model, but both the conductances and the activation parameters of the gates have been changed to mimic [Grandi et al., 2011].

The steady-states are

$$p_{a,\infty} = \left(1 + \exp\left[-\frac{V+10 \text{ mV}}{5 \text{ mV}}\right]\right)^{-1}, \quad (5.39)$$

$$p_i = \left(1 + \exp\left[\frac{V+74 \text{ mV}}{24 \text{ mV}}\right]\right)^{-1}, \quad (5.40)$$

$$n_\infty = \left(1 + \exp\left[-\frac{V+3.8 \text{ mV}}{14.25 \text{ mV}}\right]\right)^{-1}, \quad (5.41)$$

$$r_\infty = \left(1 + \exp\left[-\frac{V+6 \text{ mV}}{8.6 \text{ mV}}\right]\right)^{-1}, \quad (5.42)$$

$$s_\infty = \left(1 + \exp\left[\frac{V+7.5 \text{ mV}}{10 \text{ mV}}\right]\right)^{-1}. \quad (5.43)$$

The time constants are

$$\tau_{p_a} [\text{ms}] = 550 \left(1 + \exp\left[-\frac{V+22 \text{ mV}}{9 \text{ mV}}\right]\right)^{-1} + 230 \left(1 + \exp\left[\frac{V+40 \text{ mV}}{20 \text{ mV}}\right]\right)^{-1} + 6 \left(1 + \exp\left[\frac{V+11 \text{ mV}}{9 \text{ mV}}\right]\right)^{-1}, \quad (5.44)$$

$$\tau_n [\text{ms}] = 990.1 \left(1 + \exp\left[-\frac{V+2.436 \text{ mV}}{14.12 \text{ mV}}\right]\right)^{-1}, \quad (5.45)$$

$$\tau_r [\text{ms}] = 0.36 + 6.6 \left(1 + \exp\left[\frac{V+5 \text{ mV}}{12 \text{ mV}}\right]\right)^{-1}, \quad (5.46)$$

$$\tau_s [\text{ms}] = 2200 + 430 \left(1 + \exp\left[\frac{V+60 \text{ mV}}{10 \text{ mV}}\right]\right)^{-1}. \quad (5.47)$$

Inward Rectifying Potassium Currents

The most important inwardly rectifying potassium current in human atrial myocytes is the voltage-regulated inward K^+ rectifier, I_{K1} . This current is active at diastole and inactivates following depolarization of the membrane; it is therefore mostly impactful for the resting membrane potential of the cell. There are two

smaller inwardly rectifying potassium currents known to be present in atrial myocytes: the acetylcholine-activated channel, $I_{K,Ach}$, and ATP-inhibited channel, $I_{K,ATP}$ ([[Katz, 2010](#)]). The acetylcholine-activated channel is important if modeling the effects of heart rate modulation from the central nervous system, while the ATP-inhibited channel activates in energy-starved hearts with low access to ATP. The acetylcholine-activated channel is included in the Nygren, Maleckar and Koivumäki models, but as we are not modeling parasympathetic stimulation from the nervous system we will ignore this channel. None of the hAM models include the ATP-inhibited channel.

The I_{K1} current is given exactly as in the Nygren formulation, which is

$$I_{K1} = \bar{g}_{K1} \cdot [K]_o^{0.4457} \cdot \frac{V - E_K}{1 + \exp \left[\frac{3F}{2RT} (V - E_K + 3.6 \text{ mV}) \right]}. \quad (5.48)$$

Exchanger and Pump Currents

Exchangers and pumps are different from ion channels in that they move ions against their concentration gradients. There are three sarcolemmal exchanger and pump currents in the Koivumäki model: the sodium-potassium pump (Na^+/K^+ -ATPase or NKA), I_{NaK} , the sodium-calcium exchanger ($\text{Na}^+/\text{Ca}^{2+}$ exchanger or NCX), I_{NaCa} , and the calcium pump (plasma-membrane Ca^{2+} ATPase or PMCA), I_{CaP} . The two pumps use energy from ATP to move ions against their concentration gradients, while the NCX moves sodium along its concentration gradient, using the energy released in this process to move calcium against its gradient.

The NCX and PMCA implementations mirror the Nygren formulation, but with

Table 5.5: Membrane potassium channel parameters

Parameter	Definition	Value
\bar{g}_{to}	Max I_{to} conductance	1.1 nS
\bar{g}_{Kr}	Max I_{Kr} conductance	3.4 nS
\bar{g}_{Ks}	Max I_{Ks} conductance	0.175 nS
\bar{g}_{Kur}	Max I_{Kur} conductance	2.25 nS
\bar{g}_{K1}	Max I_{K1} conductance	2.9 nS

altered parameters. These currents are formulated as

$$I_{\text{NaCa}} = \bar{I}_{\text{NaCa}} \cdot k_{\text{NaCa}} \frac{[\text{Na}^+]_{\text{ss}}^3 [\text{Ca}^{2+}]_{\text{o}} \exp \left[\frac{\gamma VF}{RT} \right] - [\text{Na}^+]_{\text{o}}^3 [\text{Ca}^{2+}]_{\text{ss}} \exp \left[\frac{(\gamma-1)VF}{RT} \right]}{1 + d_{\text{NaCa}} ([\text{Na}^+]_{\text{ss}}^3 [\text{Ca}^{2+}]_{\text{o}} + [\text{Na}^+]_{\text{o}}^3 [\text{Ca}^{2+}]_{\text{ss}})}, \quad (5.49)$$

$$I_{\text{CaP}} = \bar{I}_{\text{CaP}} \cdot \frac{[\text{Ca}^{2+}]_{\text{ss}}}{[\text{Ca}^{2+}]_{\text{ss}} + k_{\text{CaP}}}, \quad (5.50)$$

where \bar{I}_{NaCa} and \bar{I}_{CaP} is the maximal NCX current and maximal PMCA current, respectively; k_{NaCa} is a scaling factor, γ is the relative position of the energy barrier controlling the dependence of the current on V , d_{NaCa} is a denominator constant and k_{CaP} is the half-maximum Ca^{2+} binding concentration of the PMCA.

The NKA is not formulated as in the Nygren model, but follows the formulation given in [Grandi et al., 2011]. The current is given as

$$I_{\text{NaK}} = \bar{I}_{\text{NaK}} \cdot f_{\text{NaK}} \cdot \frac{[\text{K}^+]_{\text{o}}}{[\text{K}^+]_{\text{o}} + K_{m_{\text{Ko}}}} \cdot \frac{[\text{Na}^+]_{\text{ss}}^4}{[\text{Na}^+]_{\text{ss}}^4 + K_{m_{\text{Nass}}}^4}, \quad (5.51)$$

where \bar{I}_{NaK} is the maximum current, $K_{m_{\text{Ko}}}$ and $K_{m_{\text{Nass}}}$ are the half-maximum K^+ and Na^+ binding concentrations. The fraction of active NKA, f_{NaK} , is a monotonically increasing function in V

$$f_{\text{NaK}} = \left(1 + 0.1245 \exp \left[-\frac{VF}{10RT} \right] + 0.0365 \cdot \sigma \cdot \exp \left[-\frac{VF}{RT} \right] \right)^{-1}, \quad (5.52)$$

$$\sigma = \left(\exp \left[\frac{[\text{Na}^+]_{\text{o}}}{67.3 \text{ mM}} \right] - 1 \right) / 7. \quad (5.53)$$

Although these functions are quite complex, note that f_{NaK} decreases monotonically with increasing σ , which again increases monotonically with $[\text{Na}^+]_{\text{o}}$. Put simply—the NKA is less active at higher extracellular Na^+ concentrations.

Funny Current

The funny current, I_f , is also known as the pacemaker current for its role in promoting ectopy and for its suggested prominence in myocytes located in the SA node. It is a hyperpolarization-activated current carrying both Na^+ and K^+ ions. The exact role of the funny current in atrial tissue is not known, but it has been hypothesized that it might be important in the study of abnormal ectopy in the myocardium. The current is small and only active at potentials below the resting potential of the cell, consequently, it is not a crucial influence on action potential morphology. The Koivumäki model is the only hAM model which includes the funny current, and uses the formulation given in [Zorn-Pauly et al., 2004], which was based on experimental data from human atrial myocytes.

Table 5.6: Exchanger and pump parameters

Parameter	Definition	Value
\bar{I}_{NaK}	Max I_{NaK} current	0.113 nA
\bar{I}_{CaP}	Max I_{CaP} current	2 pA
\bar{I}_{NaCa}	Max I_{NaCa} current	1 pA
$K_{m_{\text{Ko}}}$	Half-max K^+ binding conc. of I_{NaK}	1.5 mM
$K_{m_{\text{Nass}}}$	Half-max Na^+ binding conc. of I_{NaK}	11 mM
k_{CaP}	Half-max Ca^{2+} binding conc. of I_{CaP}	0.5 μM
k_{NaCa}	Scaling factor for I_{NaCa}	8.8 pA mM^{-4}
γ	I_{NaCa} dependence on V	0.45
d_{NaCa}	Denominator constant of I_{NaCa}	0.0003 mM^{-4}

The current is given as

$$I_{\text{f,Na}} = \bar{g}_{\text{f}} \cdot y \cdot \delta_{\text{Na}} \cdot (V - E_{\text{Na}}), \quad (5.54)$$

$$I_{\text{f,K}} = \bar{g}_{\text{f}} \cdot y \cdot (1 - \delta_{\text{Na}}) \cdot (V - E_{\text{K}}), \quad (5.55)$$

where $I_{\text{f,Na}}$ and $I_{\text{f,K}}$ are the sodium and potassium currents through the channel, δ_{Na} the ratio of the total current that is carried by Na^+ , \bar{g}_{f} the non-specific maximum conductance of the channel and y the activation variable of the channel; there is no inactivation variable.

The steady state of the channel is

$$y_{\infty} = \left(1 + \exp\left[\frac{V+97.83 \text{ mV}}{12.48 \text{ mV}}\right]\right)^{-1}. \quad (5.56)$$

Note that the activation is centered around -98 mV, which as mentioned means it is active when the membrane potential is lower than the resting potential, which is roughly -80 mV. The time constant of the channel is

$$\tau_y [\text{ms}] = \left(3.32 \cdot 10^{-6} \cdot \exp\left[-\frac{V}{16.54 \text{ mV}}\right] + 2.37 \cdot 10^{-2} \cdot \exp\left[\frac{V}{16.54 \text{ mV}}\right]\right)^{-1} \quad (5.57)$$

Small-conductance Calcium-activated Potassium Channel

The small potassium (SK) channel, I_{KCa} , is a low conductance calcium activated potassium channel. This channel is not included in the other hAM models, and the formulation of the channel is a novel implementation. The current is given as

$$I_{\text{KCa}} = \bar{g}_{\text{KCa}} \cdot O \cdot \left(1 + \exp\left[\frac{V-E_{\text{K}}+120 \text{ mV}}{45 \text{ mV}}\right]\right)^{-1} \cdot (V - E_{\text{K}}), \quad (5.58)$$

where the activation gate O is Ca^{2+} and not V dependent. It is modeled as a two-state Markov model

$$\frac{dO}{dt} = (1 - O)\alpha_{\text{KCa}}[\text{Ca}^{2+}]_{\text{ss}}^2 + O\beta_{\text{KCa}}[\text{Ca}^{2+}]_{\text{ss}}, \quad (5.59)$$

where the activation rate is proportional to the square of the subspace calcium concentration and the inactivation rate is constant.

External Stimulus Current

The external stimulus current used to excite the cell is not constrained by myocyte physiology and can have any shape desired; what shape is practical will depend on what the model is used for. In this thesis, unless otherwise stated, we use the stimulus current defined in the supplementary material of [Koivumäki et al., 2011], which is box-shaped current pulse. We formulate this current as

$$I_{\text{stim}} = \begin{cases} A_{\text{stim}} & \text{if } [(t \bmod \text{PCL}) - t_{\text{offset}}] < T_{\text{stim}}, \\ 0 & \text{else.} \end{cases} \quad (5.60)$$

Where the modulus operator is used to map the global time, $t \in \mathbb{R}$, to a cardiac cycle, $t \bmod \text{PCL} \in [0, \text{PCL})$, and t_{offset} then defines where in the cycle the stimulus, and subsequently action potential, occurs. Also adjustable are the amplitude and width of the pulse, A_{stim} and T_{stim} . The PCL is the pacing cycle length, i.e., the time between stimulus pulses.

[Hund et al., 2001] used the Luo Rudy ventricular myocyte model to show that the for ionic charge conservation and long-term stability of the model, the stimulus current should be implemented as a potassium current, to prevent model drift over time. This is mirrored in the Koivumäki model, I_{stim} will therefore not only affect the membrane potential of the myocyte, but also the potassium concentration.

Table 5.7: Parameters for funny and SK channels

Parameter	Definition	Value
\bar{g}_f	Non-selective max conductance of I_f	1 pA
δ_{Na}	Na^+ -ratio of I_f	0.2677
\bar{g}_{KCa}	Max conductance of I_{KCa}	3.7 pA
α_{KCa}	Activation rate of I_{KCa}	$47 \cdot 10^3 \text{ ms}^{-1}/\text{mM}^2$
β_{KCa}	Inactivation rate of I_{KCa}	$13 \cdot 10^{-3} \text{ ms}^{-1}$

Table 5.8: Standard stimulus parameters

Parameter	Definition	Value
A_{stim}	Stimulus amplitude	-575 pA
PCL	Pacing cycle length	Variable
T_{stim}	Stimulus duration	2 ms
t_{offset}	Stimulus timing offset	0 ms

5.3 Intracellular calcium dynamics

As described in Section 5.1, the bulk cytosol has been divided into four equal width compartments, each with its own percentage of the total sarcoplasmic reticulum (SR). Each compartment is modeled as isoconcentrational, meaning we have a total of eight state variables tracking the calcium in the bulk cytosol and SR. We denote these

$$[\text{Ca}^{2+}]_i \quad \text{and} \quad [\text{Ca}^{2+}]_{\text{SR},i} \quad \text{for } i = 1, 2, 3, 4, \quad (5.61)$$

where $i = 1$ denotes the innermost compartment. Calcium diffuses within the cytosol and SR, but not between the two. Calcium exits the SR through large calcium-activated release currents from ryanodine receptor (RyR) channels and smaller SR leak currents. Calcium enters the SR only through the sarco/endoplasmic reticulum Ca^{2+} -ATPase (SERCA pump). A sketch of the calcium dynamics of the Koivumäki model is shown in Figure 5.2. The intracellular calcium dynamics are novel formulations in the K model and can be found in [Koivumäki et al., 2011], with the equations listed in the supplementary material. In this Section, we first cover the formulation of the three SR calcium currents before detailing how diffusion and buffering of calcium is handled.

5.3.1 The SERCA Pump

SERCA pumps Ca^{2+} from the cytosol into the SR at the expense of ATP to ensure a low cytosolic calcium level at the onset of the next cardiac cycle. As the SR calcium concentration in myocytes is normally several thousand times higher than the cytosolic calcium concentration, SERCA is working against a very large concentration gradient. To make this process easier, the SR contains much calsequestrin (CSQN), a protein that binds to calcium and thereby sequesters or ‘hides’ it, reducing the apparent calcium concentration the SERCA has to work against.

The activity of the SERCA pump can be modeled as a binding of cytosolic

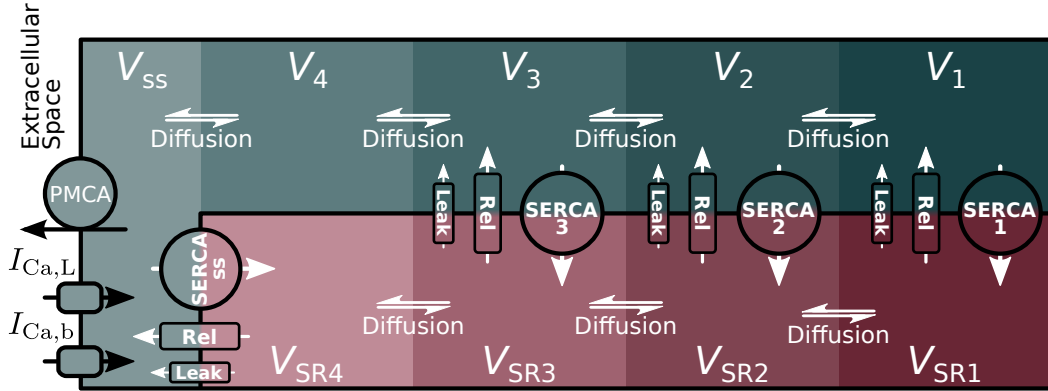
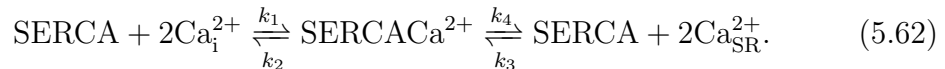


Figure 5.2: Calcium dynamics of the Koivumäki model. The sarcolemmal currents communicate with the subspace compartment. From the subspace calcium can diffuse into four progressively deeper bulk cytosolic Ca^{2+} compartments. The sarcoplasmic reticulum is also divided into four compartments, the biggest calcium release will occur from the SR connected to the subspace, but a smaller release occurs deeper into the cell.

calcium to free SERCA, and the unbinding of calcium from SERCA into the SR



Note that the reaction can occur in reverse. To model this reaction we introduce state variables for the SERCA-bound calcium. We can then express the current through the SERCA pump as a current from the cytosol into the SERCA, and another current from the SERCA into the SR. From the binding reactions these currents can be expressed as:

$$J_{x \rightarrow \text{SERCA}} = 2(k_1 \cdot [\text{Ca}^{2+}]_x^2 \cdot [\text{SERCA}]_x - k_2[\text{SERCACa}^{2+}]_x)V_x, \quad (5.63)$$

$$J_{\text{SERCA} \rightarrow \text{SR}_x} = 2(k_4[\text{SERCACa}^{2+}]_x - k_3[\text{Ca}^{2+}]_{\text{SR}_x}^2 \cdot [\text{SERCA}]_x)V_x. \quad (5.64)$$

where x is 1,2,3 and 4 for the SR compartments and 1, 2, 3 and ss for the cytosolic compartments (See Fig. 5.2). To avoid keeping track of the amount of unbound SERCA, we can express it as

$$[\text{SERCA}]_x = [\text{SERCA}]_{\text{tot}} - [\text{SERCACa}^{2+}]_x, \quad (5.65)$$

where the concentration of bound and unbound SERCA combined is assumed constant throughout the cytosol. The change in calcium-bound SERCA concentrations will then be

$$\frac{d[\text{SERCACa}^{2+}]_x}{dt} = \frac{J_{x \rightarrow \text{SERCA}} - J_{\text{SERCA} \rightarrow \text{SR}_x}}{2V_x}, \quad (5.66)$$

The rate constants of the SERCA pump is modulated by two regulatory proteins called phospholamban (PLB) and sarcolipin (SLN), the effects of these proteins have been explicitly included in the formulation of the rate constants. The net binding affinities are given as

$$K_{\text{mf}_{\text{SERCA}}} = K_{\text{mf}_{\text{PLBKO}}} + K_{\text{mf}_{\text{PLB}}}(1 - p) + K_{\text{mf}_{\text{SLN}}}(1 - p), \quad (5.67)$$

$$K_{\text{mr}_{\text{SERCA}}} = K_{\text{mr}_{\text{PLBKO}}} - K_{\text{mr}_{\text{PLB}}}(1 - p) - K_{\text{mr}_{\text{SLN}}}(1 - p), \quad (5.68)$$

where p is the baseline phosphorylation in the system, and PLBKO denotes *phospholamban knockout*, see [Koivumäki et al., 2011] for details. The binding affinities affect the rate constants k_2 and k_4 , which are given as

$$k_2 = k_1 \cdot K_{\text{mf}_{\text{SERCA}}}^2, \quad (5.69)$$

$$k_3 = k_4 / K_{\text{mr}_{\text{SERCA}}}^2. \quad (5.70)$$

Table 5.9: SERCA pump parameters

Parameter	Definition	Value
$[\text{SERCA}]_{\text{tot}}$	Cytosolic SERCA concentration	30 μM
k_1	Rate of cyt Ca to SERCA binding	0.017 $\text{ms}^{-1}\text{M}^{-2}$
k_4	Rate of SERCA to SR Ca unbinding	0.017 ms^{-1}
$K_{\text{mf}_{\text{PLBKO}}}$	Phospholamban Knockout forward	0.15 μM
$K_{\text{mr}_{\text{PLBKO}}}$	Phospholamban Knockout reverse	2.5 mM
$K_{\text{mf}_{\text{PLB}}}$	Phospholamban forward	0.12 μM
$K_{\text{mr}_{\text{PLB}}}$	Phospholamban reverse	0.88 mM
$K_{\text{mf}_{\text{SLN}}}$	Sarcolipin forward	0.07 μM
$K_{\text{mr}_{\text{SLN}}}$	Sarcolipin reverse	0.5 mM
p	Baseline phosphorylation	0.1

5.3.2 Ryanodine Receptor Release Channel

Ryanodine receptors respond to increasing cytosolic calcium concentrations and cause a large release of calcium from the SR. As the calcium release further increases cytosolic calcium concentration, the RyR release is a positive feedback loop. The formulation of the current therefore includes both calcium-dependent activation and inactivation gates. The current is given as

$$J_{\text{rel},x} = \nu_x \cdot o_x \cdot c_x \cdot \gamma_{\text{CaSR}} \cdot ([\text{Ca}^{2+}]_{\text{SR},x} - [\text{Ca}^{2+}]_{\text{Ca},x}), \quad (5.71)$$

where $x = 1, 2, 3$ and ss for the cytosolic compartments and 1, 2, 3 and 4 for the SR respectively. Here ν_x has units of nL/ms and can be expressed as the product

$$\nu_x = R_x \cdot V_x, \quad (5.72)$$

where R_x is the compartment release rate and V_x the compartment volume. The model distinguishes between the release rate of the junctional and non-junctional SR, given by $\bar{R}_{\max,ss}$ and $\bar{R}_{\max,bulk}$. rate of release, which is defined by a constant rate density in the junctional and bulk cytosol therefore scales by the compartment volume.

The factor γ_{CaSR} is a dimensionless scaling factor to account for increased release current with increased SR load. It is given as an increasing sigmoidal function in SR calcium load

$$\gamma_{CaSR} = 1 - (1 + \exp \left[\frac{[Ca^{2+}]_{SR,x} - 0.3 \text{ mM}}{0.1 \text{ mM}} \right])^{-1}. \quad (5.73)$$

The gating variables o_x and c_x represent the activation and inactivation of the channel respectively, and are independent for each compartment. The steady state values depend on cytosolic calcium, but also an adaptation gating variable, a_x . The steady states are formulated as

$$o_{x,\infty} = 1 - (1 + \exp \left[\frac{[Ca^{2+}]_{ix} - a_x + 0.22 \mu M}{0.03 \mu M} \right])^{-1}, \quad (5.74)$$

$$c_{x,\infty} = (1 + \exp \left[\frac{[Ca^{2+}]_{ix} - a_x + 0.02 \mu M}{0.01 \mu M} \right])^{-1}. \quad (5.75)$$

The adaptation variable, a_x , is a time-delayed variable that shifts the steady states of both gates. It can be thought of as a calcium-dependent gate, and its time evolution is found in the same manner as other gates in the model. However, note that a has units of concentration and fluctuates in a range narrower than $[0, 1]$. The steady state of the adaptation variable is dependent on cytosolic calcium concentration

$$a_{x,\infty} [\mu M] = 0.505 - 0.427(1 + \exp \left[\frac{[Ca^{2+}]_{ix} - 0.29 \mu M}{0.082 \mu M} \right])^{-1}. \quad (5.76)$$

The time constants of all three gating variables are modeled as constant over time, and therefore not dependent on any calcium concentrations. Activation and inactivation are modeled as more rapid for junctional RyR than for bulk RyR, while the adaptation time constant is the same for the two.

SR Leak flux

A constant-conductance SR leak flux is included in the model, given by

$$J_{SRleak,x} = \nu_{SRleak,x} \cdot ([Ca^{2+}]_{SR,x} - [Ca^{2+}]_{Ca,x}), \quad (5.77)$$

where as before, $\nu_{SRleak,x}$ is proportional to the compartment size

$$\nu_{SRleak,x} = R_{SRleak} \cdot V_x. \quad (5.78)$$

Table 5.10: SR Ca^{2+} release parameters

Parameter	Definition	Value
$\bar{R}_{\max,ss}$	Junctional release rate density	0.9 ms^{-1}
$\bar{R}_{\max,bulk}$	Non-junctional release rate density	0.0016 ms^{-1}
R_{SRleak}	SR release rate density	$6 \cdot 10^{-6} \text{ ms}^{-1}$
$\tau_{o,ss}$	Time constant for junc. RyR act.	4.3 ms
$\tau_{o,bulk}$	Time constant for non-junc. RyR act.	16 ms
$\tau_{c,ss}$	Time constant for junc. RyR inact.	13 ms
$\tau_{c,bulk}$	Time constant for non-junc. RyR inact.	74 ms
τ_a	Time constant for RyR adaptation	850 ms

5.3.3 Calcium Buffering and Diffusion

Calcium buffers are molecules that can bind to free calcium ions, forming a combined calcium-buffer complex, which can later break up again. This buffering sequesters free calcium, changing the effective calcium concentrations and gradients. It also affects diffusion of calcium, as buffer-bound calcium will have a lower diffusion rate due to the combined calcium-buffer complexes being larger. Some calcium buffers are *stationary*, meaning calcium bound to it will have an effective diffusion rate of zero. To have realistic calcium dynamics in the model it is important to account for buffering.

The theory on calcium buffering presented is mostly based on [Sterratt et al., 2011], which is a good source for a more detailed introduction.

Modeling Calcium Buffering

The binding and release of calcium from a calcium buffer can be described as a *binding reaction*



where Ca, B and CaB denotes a single Ca^{2+} ion, an unbound buffer molecule, and a calcium-bound buffer molecule. The k^+ and k^- are the forward and backward rate coefficients. In a macroscopic system, this binding reaction is governed by the *law of mass action*, which states that the rate of action is proportional to the

product of the concentrations. We have the differential equations

$$\frac{d[Ca^{2+}]}{dt} = \frac{d[B]}{dt} = -k^+[Ca][B] + k^-[CaB], \quad (5.80)$$

$$\frac{d[CaB]}{dt} = -k^-[CaB] + k^+[Ca][B]. \quad (5.81)$$

To find the dynamic equilibrium of this binding reaction, we equate the forward and backward actions

$$k^+[Ca]_\infty[B]_\infty = k^-[CaB]_\infty, \quad (5.82)$$

where the ∞ subindex denotes the steady state concentration. This again gives the *dissociation constant*

$$K_B = \frac{[Ca]_\infty[B]_\infty}{[CaB]_\infty} = \frac{k^-}{k^+}. \quad (5.83)$$

To model the calcium buffering in a cardiac myocyte, one could use equations 5.80 and 5.81 directly. This would require keeping track of both the concentrations of free calcium and buffer, as well as the concentration of calcium-bound buffer. This would involve a system of $2n + 1$ coupled ODEs per compartment, where n is the number of species of buffers explicitly included. We would also have to keep track of diffusion of both free and calcium-bound buffer, in addition to the free calcium diffusion.

The Rapid Buffer Approximation

If we are modeling whole cell electrophysiology, modeling the calcium buffering in this excruiting detail might often not be necessary, and the system can be simplified with little loss in accuracy. An important approximation here is to assume the calcium-buffer system to always be at dynamical equilibrium. This is a reasonable approximation, because the binding reactions are very quick compared to both calcium flux through the membrane and calcium diffusion in the system. Under this assumption, we can use equation 5.83 to express the amount of free and bound buffer in the system as

$$[B] = \frac{K_B[B]_{tot}}{K_B + [Ca^{2+}]}, \quad [CaB] = \frac{[Ca^{2+}][B]_{tot}}{K_B + [Ca^{2+}]}, \quad (5.84)$$

where we have introduced the total buffer concentration $[B]_{tot} = [B] + [CaB]$.

Equation 5.84 can now be used to define the *calcium binding ratio*, γ , which is expressed as

$$\gamma = \frac{d[CaB]}{d[Ca^{2+}]} = \frac{K_B[B]_{tot}}{(K_B + [Ca^{2+}])^2}. \quad (5.85)$$

The calcium binding ratio describes how much more calcium becomes bound when the calcium concentration increases and how much calcium is released when the calcium concentration sinks. The change in bound calcium can then be expressed as proportional to the change in free calcium in the system

$$\frac{d[CaB]}{dt} = \frac{d[CaB]}{d[Ca^{2+}]} \frac{d[Ca^{2+}]}{dt} = \gamma \frac{d[Ca^{2+}]}{dt}. \quad (5.86)$$

An external calcium flux, J_{Ca} , into or out of the system will change the concentration in the system directly, but also indirectly due to a change in the amount of buffer-bound calcium. The total change in the free calcium concentration is

$$\frac{d[Ca^{2+}]}{dt} = J_{Ca} - \frac{d[CaB]}{dt}. \quad (5.87)$$

Inserting Equation 5.86 yields

$$\frac{d[Ca^{2+}]}{dt} = \frac{J_{Ca}}{1 + \gamma} = \beta J_{Ca}. \quad (5.88)$$

Here, we have introduced the *buffer coefficient*, defined as $\beta = 1/(1 + \gamma)$. As $\gamma > 0$ we see that $\beta < 1$. This means that the buffering of the system will reduce the effects of any external flux into the compartment. This also leads to a lower diffusion rate in the system, which is apparent from Fick's law. Denoting the free calcium concentration, ϕ , Fick's law for free diffusion can be written

$$J_{\text{diff}} = -D_{Ca}\nabla\phi, \quad (5.89)$$

but with the presence of buffer we have to scale this calcium flux by β , yielding

$$J_{\text{diff,eff}} = \beta J_{\text{diff}} = -\beta D_{Ca}\nabla\phi = -D_{\text{eff}}\nabla\phi. \quad (5.90)$$

The presence of buffer leads to an effective change in the diffusivity of calcium. For a mobile buffer, there will also be a diffusion of calcium-bound buffer, which we have not accounted for. It can be shown, see for example [Wagner and Keizer, 1994], that in this case the effective diffusion constant becomes

$$D_{\text{eff}} = \beta(D_{Ca} + \gamma D_{CaB}). \quad (5.91)$$

For a stationary buffer, D_{CaB} is effectively zero, Equation 5.91 therefore simplifies to only the first term.

Here D_{eff} denotes the proportionality factor entering into Fick's law. However, care should be taken not to treat it like any other diffusivity; it can *not*, for example, be applied directly to the diffusion equation. To understand this, remember that the diffusion equation is derived by combining the continuity equation with

Fick's law. This means that neither of the nabla-operators will work on the diffusion coefficient β , despite it being a spatially dependent variable. The diffusion equation becomes

$$\frac{d\phi}{dt} = \beta \nabla(D_{Ca} + \gamma D_{CaB}) \nabla \phi. \quad (5.92)$$

Because γ is spatially dependent through the calcium concentration, another term will be introduced

$$\frac{d\phi}{dt} = \beta [(D_{Ca} + \gamma D_{CaB}) \nabla^2 \phi + (D_{CaB} \nabla \gamma) \nabla \phi] \quad (5.93)$$

Where the gradient of γ is

$$\nabla \gamma = -\frac{2\gamma}{K_B + \phi} \nabla \phi. \quad (5.94)$$

Giving the diffusion equation for the buffered system,

$$\frac{d\phi}{dt} = \beta (D_{Ca} + \gamma D_{CaB}) \nabla^2 \phi - \frac{2\beta\gamma D_{CaB}}{K_B + \phi} (\nabla \phi)^2. \quad (5.95)$$

For a stationary buffer this reduces to

$$\frac{d\phi}{dt} = \beta D_{Ca} \nabla^2 \phi. \quad (5.96)$$

Equations 5.95 and 5.96 describe the diffusion of calcium in a buffered system, such as the cytosol. Here ϕ is the calcium concentration, β and γ are spatially dependent buffer coefficients, D_{Ca} and D_{CaB} the diffusivities of free and buffer-bound calcium, and K_B the dissociation constant of the buffer.

5.3.4 Time Evolution of SR Calcium Concentration

The sarcoplasmic reticulum has three types of calcium fluxes through its membrane communicating with the cytosol, these are J_{rel} , J_{SERCA} and J_{SRleak} . The SERCA current is defined in the opposite direction of the other two, so the total calcium entering the SR can be written as

$$J_{SRCa} = J_{SERCA \rightarrow SR} - J_{rel} - J_{SRleak}. \quad (5.97)$$

Calsequestrin in the SR is a stationary calcium buffer, so flux of calcium in the SR will be scaled by the buffering coefficient β_{SR} . From equation 5.85 this is given from

$$\beta_{SR} = \left[1 + \frac{[CSQN]K_{CSQN}}{([Ca^{2+}]_{SR} + K_{CSQN})^2} \right]^{-1}. \quad (5.98)$$

In addition to the SR membrane fluxes, there is diffusion of calcium throughout the SR. Using the diffusion equation for a system with stationary buffer (equation 5.96) yields the governing equation for the SR calcium concentration

$$\frac{\partial \phi_{\text{SR}}}{\partial t} = \beta_{\text{SR}} D_{\text{CaSR}} \nabla^2 \phi_{\text{SR}} + \beta_{\text{SR}} j_{\text{SRCa}}. \quad (5.99)$$

Note that we have included the membrane currents as a flux of concentration and not flux of substance. The diffusivity D_{CaSR} is the effective diffusion of free calcium in the SR, meaning diffusion not affected by buffering, but affected by the porosity, constrictivity and tortuosity of the SR geometry.

Discretizing the Governing Equation

To apply equation 5.99 to our compartmentalized SR description, we have to discretize the equation in space. The flux of concentration for each compartment will simply be the flux of substance diluted into the compartments' volume

$$j_{\text{SRCa},i} = \frac{J_{\text{SRCa}_i}}{V_{\text{SR}_i}}, \quad (5.100)$$

where the index i denotes the specific SR compartment.

To discretize the diffusion component we first write out the Laplace operator in cylindrical coordinates and invoke symmetry in the azimuthal and longitudinal coordinates, giving

$$\nabla^2 \phi_{\text{SR}} = \frac{\partial^2 \phi_{\text{SR}}}{\partial r^2} - \frac{1}{r} \frac{\partial \phi_{\text{SR}}}{\partial r}. \quad (5.101)$$

Evaluating this equation in r_i and replacing both partial derivatives with central differences gives

$$\nabla^2 \phi_{\text{SR}}|_{r_i} = \frac{\phi_{\text{SR}_{i+1}} - 2\phi_{\text{SR}_i} + \phi_{\text{SR}_{i-1}}}{\Delta r^2} - \frac{1}{r_i} \frac{\phi_{\text{SR}_{i+1}} - \phi_{\text{SR}_{i-1}}}{2\Delta r} + \mathcal{O}(\Delta r^2). \quad (5.102)$$

We truncating higher order terms, insert $r_i \equiv i\Delta r$ and collect the fractions

$$\nabla^2 \phi_{\text{SR}}|_{r_i} \approx \frac{(2i+1)\phi_{\text{SR}_{i+1}} - 4i\phi_{\text{SR}_i} + (2i-1)\phi_{\text{SR}_{i-1}}}{2i\Delta r^2}. \quad (5.103)$$

To handle the end points we apply no-flux boundary conditions. This is mathematically equivalent to including ghost cells

$$\phi_{\text{SR}_0} = \phi_{\text{SR}_1}, \quad \phi_{\text{SR}_{N+1}} = \phi_{\text{SR}_N}. \quad (5.104)$$

Combining the results, we can model the time-evolution of the SR calcium concentration in each compartment from the equation

$$\frac{d}{dt}\phi_{SR_i} = \beta_{SR_i} D_{CaSR} \frac{(2i+1)\phi_{SR_{i+1}} - 4i\phi_{SR_i} + (2i-1)\phi_{SR_{i-1}}}{2i\Delta r^2} + \beta_{SR_i} J_{SRCa_i}, \quad (5.105)$$

for $i = 1, \dots, N$, denotes the different SR compartments.

The concentration of CSQN is assumed to be constant throughout the SR, and the buffer coefficient will be spatially dependent through only the SR calcium concentration

$$\beta_{SR_i} = \left[1 + \frac{[CSQN]K_{CSQN}}{([Ca^{2+}]_{SR_i} + K_{CSQN})^2} \right]^{-1}. \quad (5.106)$$

Table 5.11: Calcium diffusion and buffering parameters

Parameter	Description	Value
[CSQN]	Total concentration of calsequestrin in SR	6.7 mM
K_{CSQN}	Dissociation constant for calsequestrin	0.8 mM
D_{CaSR}	Free diffusivity of calcium in SR	50.7 $\mu\text{m}/\text{s}$

5.3.5 Time Evolution of Bulk Cytosolic Calcium

The bulk cytosolic calcium compartments have three calcium currents communicating with the SR

$$J_{Ca} = J_{SR\text{leak}} + J_{rel} - J_{Cyt \rightarrow SERCA}, \quad (5.107)$$

Calcium buffering in the cytosol of atrial myocytes has not been studied to the same degree as in ventricular myocytes, but several types of calcium buffering are believed to be present. To account for this, Koivumäki et al include a single arbitrary cytosolic mobile buffer, giving a buffer coefficient

$$\beta_{Ca} = \left[1 + \frac{[B_{Ca}]K_{BCa}}{([Ca^+]_i + K_{BCa})^2} \right]^{-1}. \quad (5.108)$$

To include the effects of a mobile buffer we use Equation 5.95, giving the time evolution

$$\frac{d\phi}{dt} = \beta(D_{Ca} + \gamma D_{CaBm})\nabla^2\phi - \frac{2\beta\gamma D_{CaBm}}{K_{BCa} + \phi}(\nabla\phi)^2 + \beta j_{Ca}. \quad (5.109)$$

The first term can be approximated in the same manner as the SR Ca²⁺ diffusion. For the second term we use a first order central difference,

$$(\nabla\phi_i)^2 \simeq \left(\frac{\phi_{i+1} - \phi_{i-1}}{2\Delta r} \right)^2, \quad (5.110)$$

giving the governing equation for the bulk cytosolic calcium concentrations

$$\begin{aligned} \frac{d\phi_{i_x}}{dt} = & \beta_i(D_{Ca} + \gamma_i D_{CaBm}) \frac{(2i+1)\phi_{i+1} - 4i\phi_i + (2i-1)\phi_{i-1}}{2i\Delta r^2} \\ & - \frac{2\beta_i\gamma_i D_{CaBm}}{\phi_i + K_{BCa}} \left(\frac{\phi_{i+1} - \phi_{i-1}}{2\Delta r} \right)^2 + \beta_i \frac{J_{Ca,i}}{V_i}, \end{aligned} \quad (5.111)$$

For compartment 4, there are no SR Ca²⁺ currents; $J_{Ca,4} = 0$ (See Fig. 5.2 on p. 59). Instead, this compartment communicates with the subspace. The diffusion current between the subspace and compartment 4 is modeled using a finite difference approximation to Fick's law,

$$J_{diff,ss} = D_{Ca} \cdot \frac{A_{j-nj}}{x_{j-nj}} \cdot ([Ca^{2+}]_{ss} - [Ca^{2+}]_4). \quad (5.112)$$

Here A_{j-nj} is the transport-available surface interface between the two compartments. It can be found as the surface area of a cylinder

$$A_{j-nj} = \pi r_{junct} \cdot l_{cell}, \quad (5.113)$$

where we have assumed only 50 % of the total interface area is transport-available. Similarly x_{j-nj} is the distance from the middle of the subspace to the middle of the first non-junctional cytosolic compartment, which can be expressed as

$$x_{j-nj} = 0.01 \text{ } \mu\text{m} + \frac{1}{2}\Delta r. \quad (5.114)$$

Table 5.12: Calcium diffusion and buffering parameters

Parameter	Description	Value
D_{Ca}	Free diffusivity of sodium in cytosol	833 $\mu\text{m}/\text{s}$
$[B_{Ca}]$	Concentration of cytosolic calcium buffer	24 μM
K_{BCa}	Diss. constant for cytosolic Ca ²⁺ buffer	2.38 μM

Sodium diffusion

There are two Na⁺ compartments in the K model, the subspace and cytosolic sodium. The only current into or out of the cytosolic compartment is the diffusion

from the subspace, which is given by the same expression as the calcium subspace diffusion

$$J_{\text{diff,Na}} = D_{\text{Na}} \cdot \frac{A_{j-\text{nj}}}{x_{j-\text{nj},\text{Na}}} \cdot ([\text{Na}^+]_{\text{ss}} - [\text{Na}^+]_{\text{bulk}}), \quad (5.115)$$

but $x_{j-\text{nj},\text{Na}}$ is now the distance from the middle of the subspace to the middle of the entire bulk space, which is

$$x_{j-\text{nj}} = 0.01 \text{ } \mu\text{m} + 2\Delta r. \quad (5.116)$$

The only changes in the bulk cytosol sodium is through the subspace flux, so the bulk sodium is governed by

$$\frac{d[\text{Na}^+]_{\text{bulk}}}{dt} = \frac{J_{\text{diff,Na}}}{V_{\text{bulk}}}. \quad (5.117)$$

5.4 Time Evolution of Ionic Concentrations

The sarcolemmal currents responsible for changing the membrane potential are carried by charged ions, which will also lead to change in the concentrations of the cell. To go from an electric currents to concentrations, we use the Faraday constant, which is the charge of one mole of electrons or monovalent ions, so for a general current

$$J_x = \frac{I_x}{zFV_x}, \quad (5.118)$$

where z is the valence of the charge-carrying ion.

The subspace compartments have different buffering from the bulk cytosol. For sodium, an arbitrary sodium buffer is included

$$\beta_{\text{Na,ss}} = \left[1 + \frac{[B_{\text{Na}}]K_{\text{BNa}}}{([Na^+]_{\text{ss}} + K_{\text{BNa}})^2} \right]^{-1}. \quad (5.119)$$

For calcium, however, the sarcolemma acts as a calcium buffer in addition to the general cytosolic buffer, because calcium can bind to the sarcolemma. Sarcolemmal calcium buffering is modeled as combination of two buffer types, corresponding to sites with high and low affinity for binding. The total buffering coefficient becomes

$$\beta_{\text{Ca,ss}} = \left[1 + \frac{[\text{SL}_{\text{low}}]K_{\text{SL}_{\text{low}}}}{([\text{Ca}^{2+}]_{\text{ss}} + K_{\text{SL}_{\text{low}}})^2} + \frac{[\text{SL}_{\text{high}}]K_{\text{SL}_{\text{high}}}}{([\text{Ca}^{2+}]_{\text{ss}} + K_{\text{SL}_{\text{high}}})^2} + \frac{[B_{\text{Ca}}]K_{\text{BCa}}}{([\text{Ca}^{2+}]_{\text{i}} + K_{\text{BCa}})^2} \right]^{-1}. \quad (5.120)$$

The time-derivatives of the subspace ionic concentrations will then be given by

$$\frac{d[Na^+]_{ss}}{dt} = -\beta_{Na,ss} \left(\frac{J_{Na}}{V_{ss}} + \frac{(I_{Na} + I_{Na,b} + 3I_{NaK} + 3I_{NaCa} + I_{f,Na})}{FV_{ss}} \right), \quad (5.121)$$

$$\frac{d[K^+]_i}{dt} = - \left(\frac{(I_t + I_{Kur} + I_{Kr} + I_{Ks} - 2I_{NaK} + I_{f,K}) + I_{KCa} + I_{stim}}{FV_{bulk}} \right), \quad (5.122)$$

$$\frac{d[Ca^+]_{ss}}{dt} = -\beta_{Ca,ss} \left(-\frac{J_{Ca,ss}}{V_{ss}} + \frac{(I_{Ca,L} + I_{Ca,b} + I_{CaP} - 2I_{NaCa})}{2FV_{ss}} \right). \quad (5.123)$$

where the extra numerical factors for the exchanger current comes from the fact that the NKA exchanger carries a unit of charge by exchanging three Na^+ ions for two K^+ potassium current; similiarly the NCX carries a unit of charge by exchanging three Na^+ for a single Ca^{2+} .

That concludes the mathematical description of the Koivumäki model. The model uses 44 state variables, i.e., it is a system of 44 coupled ordinary differential equations (ODEs). Of these 44, 16 are used to keep track of concentrations, 27 are used for gating variables and 1 is used for the membrane potential. The sheer number of state variables can partly be attributed to the number of spatial calcium compartments: 12 variables are used for the gating of release channels as there are four separate RyR models working in parallel, and of the total 16 variables tracking concentrations, 12 of them are used solely for calcium in the different compartments.

Figure 5.1, which was shown at the start of the Chapter on page 45, can act as a summary of the model, showing the various compartments and the currents connecting them.

Table 5.13: Subspace Buffering Parameters

Parameter	Description	Value
D_{Na}	Free diffusivity of sodium in cytosol	0.146 $\mu m/s$
$[B_{Na}]$	Concentration of subspace sodium buffer	1.1319 mM
K_{BNa}	Dissociation constant for sodium buffer	10 mM
$[SL_{low}]$	Concentration of low-affinity sites	165 mM
$[SL_{high}]$	Concentration of high-affinity sites	13 mM
$K_{SL_{high}}$	Diss. constant for low-aff. sites	1.1 mM
$K_{SL_{high}}$	Diss. constant for high-af. sites	0.013 mM

Chapter 6

Modeling Fibroblast-Myocyte Coupling

In addition to implementing the Koivumäki model, we will extend it to include fibroblast-myocyte coupling (FMC). In this Chapter, we first give a brief introduction to what fibroblasts are and how they can couple to cardiac myocytes. Next, we look at modeling the coupling between myocytes and fibroblasts. We then give a review of four fibroblast models proposed in the literature, selecting one of the models for use with the Koivumäki model.

6.1 Fibroblasts

Cardiomyocytes are the muscle cells that produce the force necessary for contraction in the heart. But for this force to be transmitted and distributed throughout the tissue smoothly, a network called the extracellular matrix (ECM) is necessary. Within the ECM we find collagen, a structural protein responsible for maintaining the integrity of the cardiac tissue. The ECM and collagen is produced and maintained by support cells called fibroblasts. Unlike cardiac myocytes, fibroblasts are non-excitable cells that do not contract. Healthy cardiac tissue contains about 40 % more fibroblasts than myocytes by number ([[Goldsmith et al., 2004](#)]); they are, however, much smaller and so myocytes are still more abundant in both mass and volume.

Following trauma as part of a wound healing response, fibroblasts can activate and proliferate in the tissue increasing in both number and activity. This leads to increased production of collagen in the tissue leading to *fibrosis*, an excess of fibrous connective tissue. Fibroblasts can also differentiate into a new phenotype, becoming *myofibroblasts*. Myofibroblasts share features both with fibroblasts and

smooth muscle cells, still synthesizing collagen and ECM, but also being able to contract.

Fibrosis is known to be arrhythmogenic through many mechanisms and is considered an anatomical substrate for atrial fibrillation ([[Nguyen et al., 2014](#)]). This is mainly due to collagen being non-conductive, and larger-than-normal collagen deposits will electrically decouple the myocardial syncytium leading to both slowed conduction, and possibility of unidirectional conduction block.

Experimental studies show that gap junctions between myocytes and fibroblasts can form in *in vitro* cell cultures ([[Kohl and Camelliti, 2007](#)]). While fibroblasts are non-exitable, gap junctions between myocytes and fibroblasts have big implications for electrophysiological properties of the myocardium, as this would lead to increased electrotonic load for myocytes as the fibroblasts act as current sinks. To what extent fibroblast-myocyte gap junctions are present *in situ* are still unknown, but [[Camelliti et al., 2004](#)] showed that they are present in the rabbit sinoatrial node. Figure 6.1 shows images of fibroblast-myocyte gap junctions in sheep myocardium. It has been hypothesized that myocyte-fibroblasts gap junction become upregulated and more numerous during heart disease, as fibroblasts isolated from ischemic hearts express more connexin, the structural protein of gap junctions ([\[Vasquez et al., 2009\]](#)).

If myocyte-fibroblast coupling through gap junctions really does become upregulated *in situ* in cardiac disease, such coupling may be important in understanding the proarrhythmic effects of fibrosis. In light of this, there have been numerous cell culture experiments and computational studies the last ten years on the effects of fibroblast-myocyte coupling. We aim to reproduce some results of this work using the Koivumäki model.

6.2 The Gap Junction Current

Gap junctions consist of connexin proteins forming connexon pores between two cells. Ions can then move through the pores from the interior of one cell to the other, carrying an electric current between them. The transport of ions through the gap junction is passive, driven by an electrodiffusion gradient between the two cells. As a first approximation, the current can be expressed as a non-specific Ohmic current

$$I_{\text{gap}} = G_{\text{mf}}(V_m - V_f). \quad (6.1)$$

Here V_m is the myocyte transmembrane potential and V_f is the fibroblast membrane potential, the difference between these two is then the driving voltage of the gap junction current, and G_{mf} is the conductance of the m-f gap junction.

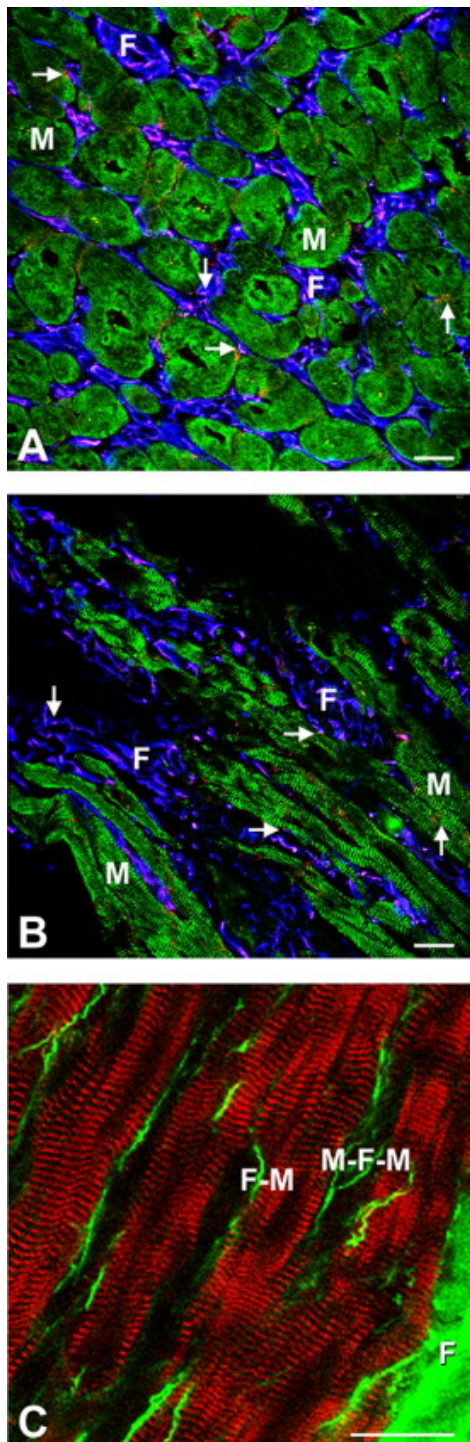


Figure 6.1: Physiological images of cardiac myocytes and fibroblasts together *in situ*. The scale bars correspond to 20 μm .

(A, B): Using antibodies, myocytes have been marked green and fibroblasts blue. Both images are of sheep myocardium with (A) being healthy tissue and (B) infarcted tissue. Note a higher relative proportion of fibroblasts in the infarcted tissue. Connexin43, a specific type of connexin protein, has been marked orange-violet, showing gap junctions. The arrow point to different types of cell-cell connections: ↑ means myo-myo junction , ↓ means fib-fib junction, →: means myo-fib junction.

(C): Fibroblasts have been marked green and myocytes in striated red. Fibroblasts can be distant and unconnected from the myocytes (F), between directly connected groups of myocytes (F-M) or bridge gaps between unconnected myocytes (M-F-M).

Figure taken from [Kohl and Camelliti, 2007]. Figure is under copyright of and used with permission from Elsevier.

In this case, the gap-junction current I_{gap} is defined as positive when current is flowing from the myocyte to the fibroblast.

A more accurate formulation would be to describe the current as carried by different ionic species

$$I_{\text{gap}} = I_{\text{gap},\text{Na}} + I_{\text{gap},\text{K}}, \quad (6.2)$$

$$I_{\text{gap},x} = G_{\text{mf},x}[(V_m - V_f - E_{\text{gap},x})], \quad \text{for } x = \text{Na, K}. \quad (6.3)$$

Each ion must now be described by their own species-specific gap junction conductance. We must also include the Nernst-potential to account for the electro-diffusion equilibrium of the ions

$$E_{\text{gap},x} = \frac{RT}{z_x F} \log \frac{[x]_f}{[x]_m}, \quad \text{for } x = \text{Na, K}. \quad (6.4)$$

Where the subindices indicate whether the intracellular ion concentrations of the fibroblast or the myocyte are meant.

Note that these equations only include Na^+ and K^+ as charge carriers. Calcium is ignored, as the cytosolic concentrations are several orders of magnitude smaller than those of sodium and potassium and could therefore contribute negligibly to the gap junction current.

Circuit equivalent diagrams of a myocyte-fibroblast pair coupled with these gap junction currents are shown in Figure 6.2.

Larger systems of myocytes and fibroblasts

If looking at systems of more than two cells, there will be a possible gap junction between any pair of neighboring cells. In Figure 6.1A and B, different configurations of coupling between myocytes and fibroblasts are present in the form of myocyte-myocyte, fibroblast-fibroblast and myocyte-fibroblast couplings. Following the terminology laid forth in [Kohl and Camelliti, 2007], it is useful to distinguish between zero-sided, single-sided or double-sided connections.

- *Zero-sided connections* means no myocyte-fibroblast coupling. No current will pass between them and fibroblasts are effectively passive insulating barriers, much like collagen. This corresponds to the isolated fibroblast marked F in Figure 6.1C. In the zero-sided case, no model is needed to model the fibroblasts' electrophysiology.
- *Single-sided connection* means that one or more fibroblasts are coupled to a single myocyte or a group of myocytes that are tightly enough coupled to act as a single unit. In this case, fibroblasts act as an electrotonic load for

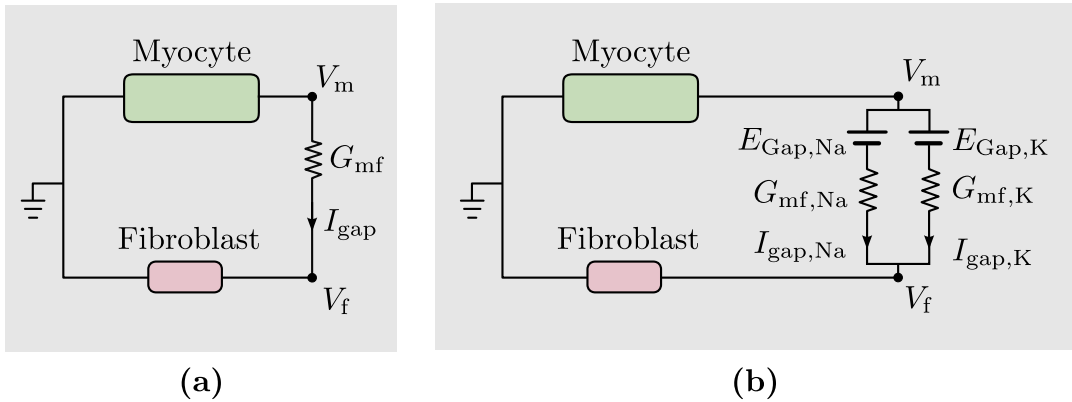


Figure 6.2: Circuit equivalent diagrams of myocyte-fibroblast coupling with Ohmic gap junction currents. (a) Non-specific gap current. (b) Ion-specific gap currents.

myocytes in the system, but do not lead to new conduction paths in the tissue. This corresponds to the F-M configuration in Figure 6.1C.

- *Double-sided connection* means that fibroblasts can couple to both other fibroblasts and myocytes, an possibly several cells at once. This means fibroblasts can act as conductive bridges, even through otherwise non-conductive collagen barriers. This is like the M-F-M configuration in Figure 6.1C.

As seen in the image, in myocardium all three types of connections are likely to co-exist. Tissue-level modeling is needed to see the effects of the insulating effects of the zero-sided connections and the bridging/conductive effects of double-sided connections. But to examine electrotonic load effects of single/double-sided connections, it is sufficient to use models for a single myocyte.

In this thesis, we do not look at tissue-level dynamics, but only run single-myocyte simulations. We therefore only look at one-sided coupling of a number of fibroblasts to the same myocyte. The gap junction current of each coupled fibroblast can then either be modeled independently, or assumed similar and simply multiplied by the number of coupled fibroblasts, n_{fib} .

6.3 Fibroblast Models

Electrophysiological models for cardiac fibroblasts are not well developed compared to myocyte models. A big reason for this is that it is still unknown to what extent fibroblast-myocyte coupling occurs *in situ*. Another important reason is

that there exists much less experimental electrophysiological data on fibroblasts than myocytes and reported data varies much more drastically than myocyte data, even within single studies. Some of the reported variation can be explained by electrophysiological measurements being more challenging on fibroblasts due to their small size and high input resistance compared to myocytes, which could also lead to culture artifacts ([MacCannell et al., 2007]). However, it could also be feasible that there are larger natural variations in fibroblasts than found in myocytes.

There are wide ranges of most electrophysiological measurements of fibroblasts reported in the literature. This means that it is impossible to fine-tune any of our current fibroblast models. Instead, the currently existing fibroblast models should be seen as computational tools to study the theoretical mechanistic effects of fibroblast-myocyte coupling, at which they have been very successful. If future studies indicate that FMC is common *in situ* in disease, more accurate electrophysiological measurements and thus more experimentally constrained models are sure to follow.

The Passive Fibroblast Model

Fibroblasts are non-excitible, meaning they will not fire an action potential if stimulated by a small current. This does not mean however, that the fibroblast cell membrane cannot contain any ion channels or that the transmembrane potential is constant. One of the simplest model we can construct for the fibroblast is a cell containing only a single non-specific constant conductance leak current

$$I_f = G_f(V_f - E_f). \quad (6.5)$$

Where G_f is the conductance of the leak current, V_f is the fibroblast membrane potential and E_f the reversal potential of the leak current. For an isolated fibroblast, the resting fibroblast potential will equal to the reversal potential and so we could also refer to E_f as the fibroblast resting potential.

As this fibroblast model does not contain any gated ion channels, it does not respond to its environment or changing membrane potential in any way, and so can be referred to as a *passive* fibroblast model. This is in contrast to *active* fibroblast models, which contain gated ion channels.

The simplicity of the passive model comes with the payoff that there is only really four properties that define the properties of the fibroblast: (1) The capacitance C_f , (2) the fibroblast rest potential E_f , (3) the conductance of the leak current G_f , and (4) the myocyte-fibroblast coupling conductance, G_{mf} . Using such a passive model, we can study the effects of every parameter in both isolation and

in connection to all the other parameters and, with reasonable effort, explore large parts of the model's parameter space.

A natural extension of the simple passive fibroblast is splitting up the leak current into specific ionic currents

$$I_f = G_{f,\text{Na}}(V_f - E_{f,\text{Na}}) + G_{f,\text{K}}(V_f - E_{f,\text{K}}). \quad (6.6)$$

[Xie et al., 2009] used a non-specific passive fibroblast to study the effects of FMC on a ventricular myocytes. They looked at one-sided connection of a number of passive fibroblasts to the Luo Rudy 1 model from the human ventricular myocyte. They also look at FMC on a rabbit ventricular model they developed themselves. Their results show that the effects of the FMC can vary wildly depending on the passive fibroblast parameters. They showed that the FMC can prolong or shorten action potential duration (APD), promote or suppress voltage-driven APD alternans by altering APD restitution and promote calcium driven and spatially discordant alternans. They describe most of these changes in terms of the gap junction current, which they describe as having an early component that looks much like the transient outward current of the myocyte.

The Sachse Fibroblast

[Sachse et al., 2008] produced a mathematical fibroblast model based on experimental data of isolated adult rat ventricular fibroblasts. Their data showed that the fibroblast contained two potassium currents: an inwardly rectifying potassium current and a voltage dependent outward potassium current. In addition they added an unspecific background current. In total the Sachse et al fibroblast model is

$$\frac{dV_f}{dt} = -\frac{1}{C_f}(I_{\text{Kir}} + I_{\text{Shkr}} + I_b). \quad (6.7)$$

They used the model to study how a single virtual rat ventricular myocyte was affected when coupled to one or more fibroblasts. They found it had little impact on the myocyte resting potential and action potential amplitude, but observed larger changes in both action potential duration and the upstroke velocity of the myocyte membrane potential (dV/dt_{max}). They also studied conduction in a 1D chain of myocytes layered with single-sided connected fibroblasts and found that both upstroke velocity and conduction velocity was reduced. They finally studied the bridging effects of fibroblasts, and found that a single fibroblast coupling two chains of myocytes could lead to either propagation, delayed propagation or conduction block, depending on both the m-m and m-f conductances.

The methodology and conclusions of Sachse et al are very interesting, but the model itself describes rat ventricular fibroblasts and so should not be applied directly to the human atrial Koivumäki model.

The Jacquement Fibroblast

[Jacquemet and Henriquez, 2007] developed a phenomenological fibroblast model to study how much fib-myo coupling would be needed to significantly perturb electrical propagation. The study was based on a mouse myocyte model and described the fibroblast membrane currents using a single current-voltage curve fitted to experimental data. The current was described as having a delayed activation, with a voltage-dependent time constant, much like the gating mechanisms of the Hodgkin-Huxley model. The steady-state current was fitted to a third-degree polynomial. The Jacquement et al model can then be written as

$$\frac{dV_f}{dt} = -\frac{1}{C_f} I_f, \quad I_f = \frac{I_{f,ss}(V_f) - V_f}{\tau_f(V_f)}, \quad (6.8)$$

$$I_{f,ss}(V_f) = c_3 V_f^3 + c_2 V_f^2 + c_1 V_f + c_0. \quad (6.9)$$

Jacquement and Henriquez used their model in a 1D strand of myocytes and found that the added fibroblasts both increased the myocyte resting potential and acted as current sinks, leading to a reduction in conduction and maximum upstroke velocity. However, they concluded that the effects of FMC were too small to account for the slowed conduction seen in fibrotic tissue—stating instead that microstructural changes and myocyte decoupling are still necessary factors.

The MacCannell Fibroblast

[MacCannell et al., 2007] produced a model based on human ventricular fibroblasts. The model includes four membrane currents, two of which they observed directly in experiments. The two observed currents are an inward-rectifying potassium current and a time and voltage dependent rectifier potassium current. In addition to these, the authors argue for the inclusion of a potassium pump to offset the potassium efflux of the two observed channels. They argue that Na^+/K^+ -ATPase is a good candidate, as it is expressed in all mammalian tissue. Finally a sodium leak current is included to offset the sodium lost through the NaK-pump. The two potassium currents were fitted to experimental data, while the properties of the NaK-pump and the sodium leak current were chosen such that the influx and efflux of both potassium and sodium were balanced.

The inwardly rectifying K^+ current was modeled by reparameterizing the I_{K1} channel from the ten Tusscher model for the human ventricular myocyte ([[ten Tusscher et al., 2004](#)]). The current is given by

$$I_{K1} = \bar{g}_{K1} \frac{\alpha_{K1}}{\alpha_{K1} + \beta_{K1}} (V_f - E_{f,K}), \quad (6.10)$$

where α and β represent the fractional open probability of the channels as functions of the fibroblast membrane potential.

The time- and voltage gated channel is modeled using an activation variable s , and an inactivation variable r . The current is given by

$$I_{Kv} = \bar{g}_{Kv} r_{Kv} s_{Kv} (V_f - E_{f,K}). \quad (6.11)$$

where the steady state values for the gates are

$$r_{Kv,\infty} = \left(1 + \exp\left[-\frac{V+20\text{ mV}}{11\text{ mV}}\right]\right)^{-1}, \quad (6.12)$$

$$s_{Kv,\infty} = \left(1 + \exp\left[\frac{V+23\text{ mV}}{7\text{ mV}}\right]\right)^{-1}, \quad (6.13)$$

with time constants

$$\tau_{r_{Kv}} \text{ ms} = 20.3 + 138 \exp\left[-\left(\frac{V+20\text{ mV}}{25.9\text{ mV}}\right)^2\right], \quad (6.14)$$

$$\tau_{s_{Kv}} \text{ ms} = 1574 + 5268 \exp\left[-\left(\frac{V+23\text{ mV}}{22.7\text{ mV}}\right)^2\right], \quad (6.15)$$

$$(6.16)$$

The sodium-potassium pump was modeled on a previous NaK pump model from the same group

$$I_{NaK} = \bar{I}_{NaK} \left(\frac{[K^+]_o}{[K^+]_o + K_{mK}} \right) \left(\frac{[Na^+]_i^{3/2}}{[Na^+]_i^{3/2} + K_{mNa}^{3/2}} \right) \frac{V_f - E_{NaK}}{V_f - B}. \quad (6.17)$$

Here the K 's are the half-maximum binding constants, E_{NaK} is the reversal potential of the pump and B is scaling a parameter with unit millivolts.

And, finally, the sodium leak current is a modeled as an Ohmic current

$$I_{Na,b} = g_{Na,b} (V_f - E_{f,Na}). \quad (6.18)$$

The complete MacCannell model can then be written out as

$$\frac{dV}{dt} = -\frac{1}{C_f} (I_{K1} + I_{Kv} + I_{NaK} + I_{Na,b}) \quad (6.19)$$

A sketch of the MacCannell fibroblast is shown in Figure 6.3.

MacCannell et al coupled their model to the ten Tusscher model for human ventricular myocytes ([[ten Tusscher et al., 2004](#)]). They found significant reductions in the action potential plateau height and action potential duration, as well as changes in the underlying ionic currents. They found that FMC had little impact on the myocyte resting potential, due to the ventricular myocytes' much larger capacitance compared to the fibroblast. They also performed computations with a passive fibroblast model, finding the effects to be much smaller, concluding that active fibroblast models were of importance in further modeling work.

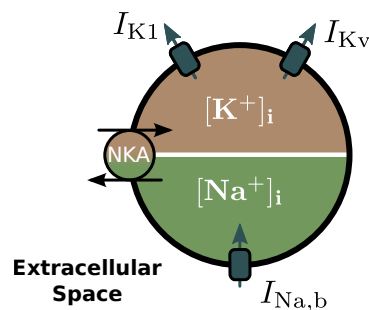


Figure 6.3: Schematic of the ventricular MacCannell fibroblast model, on which the Maleckar human atrial fibroblast model is based.

The Maleckar Fibroblast

The MacCannell fibroblast model is based on human data, but it describes a ventricular fibroblast. [[Maleckar et al., 2009a](#)] reparameterized the model proposed by MacCannell to better fit experimental data from human atria, thereby creating a model for the human atrial fibroblast. The parameters used for the Maleckar fibroblast model are shown in Table 6.1.

Citing the importance of the fibroblast resting potentials impact on the FMC, Maleckar et al also used a different parameter set to yield a fibroblast with a higher resting potential. They designated the two model variants as active I and active II. The changes done to the active II are

- The I_{Kv} max conductance has been reduced to 0.22 nS/pF (-11 %).
- The I_{Kv} steady states voltage-dependence has been shifted by 20 mV.

$$r_{Kv,\infty} = \left(1 + \exp\left[-\frac{V}{11 \text{ mV}}\right]\right)^{-1}, \quad (6.20)$$

$$s_{Kv,\infty} = \left(1 + \exp\left[\frac{V+3 \text{ mV}}{7 \text{ mV}}\right]\right)^{-1}. \quad (6.21)$$

- The I_{NaK} max current has been reduced 1.355 pA/pF (-18 %).

These changes reduced the fibroblast resting potential from -47.8 mV (Active I) to -31.4 mV (Active II).

To study the effects of fibroblast-myocyte coupling on the Koivumäki model, we will use both active human atrial fibroblast models proposed by Maleckar et al, in addition to two passive fibroblast models parameterized to have behavior close to the Maleckar fibroblasts.

Table 6.1: Parameters for the Maleckar fibroblast model

Parameter	Definition	Value
T	Model temperature	33° C
C_f	Fibroblast capacitance	6.3 pF
$V_{cyt,f}$	Cytosolic fibroblast volume	$1.37 \cdot 10^{-3}$ nL
\bar{g}_{K1}	Max I_{K1} conductance	0.4822 nS/pF
\bar{g}_{Kv}	Max I_{Kv} conductance	0.22 nS/pF
\bar{I}_{NaK}	Max I_{NaK} current	1.644 pA/pF
$g_{Na,b}$	Conductance of Na^+ background current	9.5 pS/pF
K_{m_K}	Half-max K^+ binding conc. of NKA	1.0 mM
$K_{m_{Na}}$	Half-max Na^+ binding conc. of NKA	11.0 mM
E_{NaK}	Reversal potential of NKA	-150 mV
B	NKA voltage-scaling	-200 mV

Chapter 7

Solving the Model

In Chapter 5 we outlined the mathematical formulation of the Koivumäki model, and in Chapter 6 we looked at mathematical models of fibroblasts. In this Chapter we outline how such models can be implemented and solved numerically. We also cover how the implementation and solve were verified, to avoid issues of faulty code.

7.1 Solving Initial Value Problems

The equations of the Koviumäki model, detailed in Chapter 5, form a system of coupled ordinary differential equations (ODEs), which can be written as

$$\frac{d\mathbf{y}}{dt} = f(t, \mathbf{y}(t)), \quad (7.1)$$

here \mathbf{y} is vector of state variables and f is the function mapping the current time and values of the state variables to their derivatives. The equation is not well-posed without a set of initial state values

$$\mathbf{y}_0 = \mathbf{y}(t_0). \quad (7.2)$$

The combination of the ODE system and initial values forms a well-posed *initial value problem*, meaning a solution for the time evolution of all state variables, $\mathbf{y}(t)$, exists and is unique.

Initial value problems such as the Koivumäki model can be solved numerically using finite difference methods. In such an approach we uniformly discretize the time domain using a finite time step Δt , yielding time points

$$t_i = i\Delta t. \quad (7.3)$$

By Taylor expanding \mathbf{y} , we get

$$\mathbf{y}(t + \Delta t) = \mathbf{y}(t) + \Delta t \mathbf{y}'(t) + \frac{1}{2} \Delta t^2 \mathbf{y}''(t) + \mathcal{O}(\Delta t^3). \quad (7.4)$$

From Equation 7.4 we can express the time derivative of \mathbf{y} as

$$\mathbf{y}'(t) = \frac{\mathbf{y}(t + \Delta t) - \mathbf{y}(t)}{\Delta t} + \frac{1}{2} \Delta t + \mathbf{y}''(y) + \mathcal{O}(\Delta t^2). \quad (7.5)$$

For small Δt , the last terms will be very small and can be truncated

$$\mathbf{y}'(t) \approx \frac{\mathbf{y}(t + \Delta t) - \mathbf{y}(t)}{\Delta t}. \quad (7.6)$$

This is the first order forward finite difference. Replacing the derivative in equation 7.1 with a first order forward difference and evaluating the equation in t_i

$$[D_t^+ \mathbf{y}(t) = f(t, \mathbf{y}(t))]^{t_i}, \quad (7.7)$$

yields the forward Euler numerical scheme

$$\mathbf{y}_{i+1} = \mathbf{y}_i + \Delta t f(t_i, \mathbf{y}(t_i)). \quad (7.8)$$

This recursive formula lets us calculate the state variables at increasing time points, thus approximating the time evolution of \mathbf{y} . Every time step performed introduces a small error due to the finite difference approximation. From equation 7.4, we see the error is

$$\mathbf{y}(t_i + \Delta t) - \mathbf{y}_i = \frac{1}{2} \Delta t^2 \mathbf{y}''(t_0) + \mathcal{O}(\Delta t^3). \quad (7.9)$$

This is the *local error* of the forward Euler method, which is proportional to Δt^2 . To solve the equations on the interval $t \in (t_0, T]$, we take a total of $N = T/\Delta t$ steps, and so the error will accumulate over all steps taken, leading to a *global error* of

$$E(\Delta t) = \left(\frac{1}{2} \Delta t^2 \mathbf{y}''(t_0) + \mathcal{O}(\Delta t^3) \right) \cdot \frac{T}{\Delta t} = \mathcal{O}(\Delta t). \quad (7.10)$$

As the global error introduced by using the forward Euler scheme to solve the initial value problem is on the order of Δt , the forward Euler scheme is a first-order method.

The forward Euler scheme is the simplest finite difference scheme and many more, often more complex, numerical schemes exist, differing in their approximation to the derivative. Different schemes have different strengths and are naturally suited for modeling different systems. We will now discuss a few of the properties of the Koviumäki model and how that affects our choice of numerical scheme.

Non-linearity

The Koivumäki model is a highly non-linear system of differential equations. This means that the function mapping $(t, \mathbf{y}(t))$ to $\mathbf{y}'(t)$ is not linear. Non-linear ODE systems are in general harder to solve using implicit schemes, such as the *backward Euler*. When using an implicit scheme, the unknown will enter the right-hand side of Equation 7.1. This means the solver has to take into account the exact form of the mapping function f , and the resulting system of equations will have to be solved using analytical or numerical methods. One technique to get around this is to linearize the ODEs or use convergence methods such as Picard-iterations or Newton's method.

Explicit time-discretization methods circumvent the non-linearity of the equations altogether. As the right-hand side, f , is only ever evaluated in previous time steps, where the state values are known, it is straight forward to calculate the right hand side of the system. This means the non-linearity is contained. Explicit methods can thus treat the right-hand side as a black box, simply evaluating the function in the known state values—which makes implementing general explicit solvers considerably easier than implementing implicit ones.

Accuracy and Stability

As we have seen, the accuracy of the numerical solution is proportional to the time-step Δt , meaning a bigger timer step will lead to a larger error. If the time step is increased too much, the numerical solution can start to behave completely different from the actual solution of the initial value problem. A classic example for this is in a model for exponential decay, where a too big time step leads to both oscillatory and growing solutions—both of which have no mathematical foundation in the problem. Stability is a result of how a problem and a numerical scheme work together and must be dealt with on a case-to-case basis.

Conductance-based cell models are inherently unstable due to the gating mechanisms of the channels. The gating variables change over time and in response to changes in V . These changes are exponential, and lead to *stiffness* in the equations. Stiffness is a property meaning a small change in a variable can lead to large changes in the solution. Exponential changes and stiffness can both quickly lead to instability for large time steps. To understand this, recall from our review of the Hodgkin-Huxley model in Section 4.1 that the evolution of the gating particles are given by the differential equations

$$\frac{dp}{dt} = \frac{p_\infty - p}{\tau}, \quad (7.11)$$

solving this system with a forward Euler scheme gives the equations

$$p_{i+1} = p_i + \frac{\Delta t}{\tau} (p_\infty - p_i). \quad (7.12)$$

We know that the gating variable p should approach p_∞ , exponentially. But from Equation 7.12 we see that as long as $\Delta t/\tau$ is larger than unity, p can overshoot p_∞ . This has dramatic consequences for our solution, because even though the steady-state p_∞ is constrained to the interval $[0, 1]$ we now see that p can overshoot and become larger than 1, leading to a larger-than-maximal conductance in a channel. This behavior is clearly a numerical artifact and not a mathematical property of the model itself and comes from instability in the solver. In summary: the forward Euler scheme is only *conditionally stable* for the Koivumäki model, and will be unstable if $\Delta t > \tau_x$ for a given gate x . Other schemes will have different stability criteria.

A numerical scheme developed to handle the instability of the gating variables was proposed in [[Rush and Larsen, 1978](#)]. To derive this scheme note that when evaluating equation 7.11 at time t_i , p_∞ and τ will have constant values, and the differential equation then has a known analytical solution

$$p_{i+1} = p_\infty + (p_i - p_\infty) \exp\left(-\frac{\Delta t}{\tau}\right). \quad (7.13)$$

Note that equation 7.13 is *unconditionally stable* as p can no longer overshoot p_∞ . It is however, not necessarily accurate, as p_∞ and τ are not really constant in time. The accuracy of the Rush-Larsen scheme thus depends on how fast the steady state and time constants of the gate is changing. In the originally proposed Rush-Larsen scheme, this exponential integrator approach was used for all gating variables in a cell model, while the standard forward Euler was used for all remaining state variables.

Many higher-order explicit schemes have been formulated and can be found in textbooks on numerical methods, such as [[Süli and Mayers, 2003](#)]. A commonly used family of methods are the Runge-Kutta methods. These exist in both explicit and implicit forms and of different orders of accuracy. Two commonly used are the explicit second order Runge-Kutta, the RK2, and the explicit fourth order Runge-Kutta, the RK4. While these boast higher orders of accuracy than the forward Euler, they are not known for their stability and are general unsuitable for stiff problems.

7.2 Implementation

When implementing and solving cell models, there are many options for programming languages and frameworks to use; commonly found in the literature

are MATLAB, C/C++, Python, Fortran, as well as dedicate software packages such as NEURON. Independently of what language or package one opts to use, the implementation of the model itself and the solver should be separated. This separation gives the freedom to use different solvers on the same cell model, or solving different models with the same solver—this makes both verification and comparison easier, and makes the code more portable and extendable.

Before we chose what framework to use to implement the Koivumäki model, we considered what properties we wanted our implementation to have:

- *Flexibility*—the mathematical model should be easy to combine with different solvers and specific parameters and state values should be easy to alter.
- *Readability*—the code specifying the mathematical model should be easily readable by a human, even if they are not familiar with the framework. This especially means that the code should look as much like the mathematical formulation of the problem as possible.
- *Modularity*—cell models are inherently modular due to being built up of individual ion channels. For both verification of subcomponents of the model as well as future extendability and portability, the code should reflect the model’s modularity.
- *Metainformation*—as seen in Chapter 5, cell models can consist of a very large amount of parameters and expressions. To avoid confusion when altering or using the model, descriptions of parameters as well as information about what units they have should be present and easily accessible in the implementation.

When it comes to flexibility, it would be very useful to have a model implementation that was not tied to any specific platform, so that one could freely use solvers in different frameworks. One tool to achieve such a goal is CellML¹. CellML is a markup based language based on XML, used for specifying mathematical models in biology and physiology. Once a model has been implemented in CellML, code can be auto-generated in C, Fortran77, Matlab and Python. The goal of the project is to allow scientists to share their models independently of what tools they personally use.

The CellML approach scores highly on flexibility, modularity and the possibility of including metainformation. It does, however, score low on readability. The base language of XML makes the code easily parseable by a computer, but it is not meant to be directly read or written by humans. The auto-generated code is also hard to parse for the user and it hides the mathematic expressions used in

¹See <https://www.cellml.org/> for more information.

the model.

For a similar approach to the CellML format, we turn to Gotran (General ODE TRAnslator)², a lightweight Python interface for specifying ODE systems. The Pythonic Gotran-syntax is very close to the mathematical formulation of ODEs and is easily read and modified by the user. Models specified in Gotran are saved in files with a `.ode`-extension. Such files can easily be written by the user or automatically generated from a CellML-specified ODE. From an `.ode`-file, Gotran allows auto-generation of code in C, C++, Python, Matlab and CUDA. There are also tools available for auto-generating code to be used with FEniCS, a finite element package for scientific computing and cbcbeat, a package for cardiac electrophysiology problems³. Coupling the ODE implementation directly to FEniCS is very helpful for further extendability to two- and three-dimensional simulations.

Although the Gotran-framework allows for much flexibility in the type of auto-generated code, the workflow of either having to generate new code from a base `.ode`-file or modifying hard-to-read computer-generated code can be slow, frustrating and error-prone. Instead of using this approach, we will use Gotran's capabilities of producing just-in-time (JIT) compiled C code that is interfaced in Python through SWIG⁴. The Gotran framework accepts compilation flags to allow the JIT-compiled C code to have built-in solvers. This allows us to write Python scripts that work directly on the `.ode`-files and solving it through low-level C code, removing the need for a multi-step workflow of first auto-generating code, and then interfacing said code.

Although the Gotran framework handles the compilation of the C code as well as the SWIG interfacing behind-the-scenes, the code needed to set up this system as well as handle it through scripting can be quite difficult unless proficient in Gotran. To make the workflow of going from a `.ode`-file specification to virtual experiments both quick and as easy as possible for the user, we create a Python-class to interface Gotran.

We design the `ODEProblem`-class such that the constructor takes in a `.ode`-file and JIT-compiles it, the `ODEProblem`-object then acts as an interface to the model with setters and getters for any parameter or state value as well as methods for solving the model over time. When compiling the model, the user can use flags to choose desired numerical scheme. We have created subclasses of the `ODEProblem`-class called `CellModel` and `MyocyteModel`. These subclasses have more specific functionality relevant for cell models, such as calculating action potential duration for a given level of repolarization.

²See <https://bitbucket.org/johanhake/gotran>.

³See <https://bitbucket.org/meg/cbcbeat>

⁴Simplified Wrapper and Interface Generator. <http://www.swig.org/>

As described in the last Section, the Koivumäki model contains stiff gating equations and so must be solved with a fairly small time step. The number of states contained in the model and the relatively long simulation times needed for simulations makes it is unfeasible to store all model states over time. The `ODEProblem`-framework therefore only keeps track of the current state values and instead has implemented methods used to specify what states to track over time. In addition to state values, the framework allows for tracking any intermediate expressions in the model over time, such as the current of a specific channel.

The source code for the `CellModel`/`MyocyteModel`-classes can be found online⁵. This repository also includes the implemented `.ode` files for the 2014 and 2015 formulations of the Koivumäki model, as well as the extended model including fibroblast-myocyte coupling. The solver classes are found in `/src/`, while the ODE implementations (along with initial conditions) are found in `/ode/`.

A schematic of the workflow when using the `MyocyteModel`-class to solve the Koivumäki model or similar models is shown in Figure 7.1 on page 90. For an example of Gotran syntax an implementation of the Hodgkin-Huxley model is shown in Listing 7.3 on page 94. For an example of use of the `MyocyteModel` see Listing 7.1.

⁵See <https://bitbucket.org/jonasvdbrink/cellmodel>.

Listing 7.1: Example of use for `MyocyteModel`. The constructor of the class reads in the path of the `.ode`-file and JIT compiles the ODE system. The solver flag specifies that the Rush-Larsen numerical scheme is to be used and the intermediates flag causes the model to be compiled with functionality to track the sodium current. The second and third adjust two parameters in the model. Finally the model is solved on the interval $t \in (0, 2000 \text{ ms}]$ with a time step of 1 μs , while tracking the membrane voltage, the four gating variables of the sodium current and the sodium current itself. The returned variables is an array of time-points and a dictionary of arrays of the tracked values. The final line indicates how one could plot the sodium current using the matplotlib plotting package for Python.

```
model = MyocyteModel("K2015_nSR.ode",
                      solver='rush_larsen', intermediates='INa')

model.set_param('gNa', 0.4)
model.set_param('PCL', 500)

t, d = model.tracksolve(dt=0.001, T=2000, states=['V', 'm', 'h1', 'h2', 'f1'],
                        intermediates='INa')

plt.plot(t, d['INa'])
```

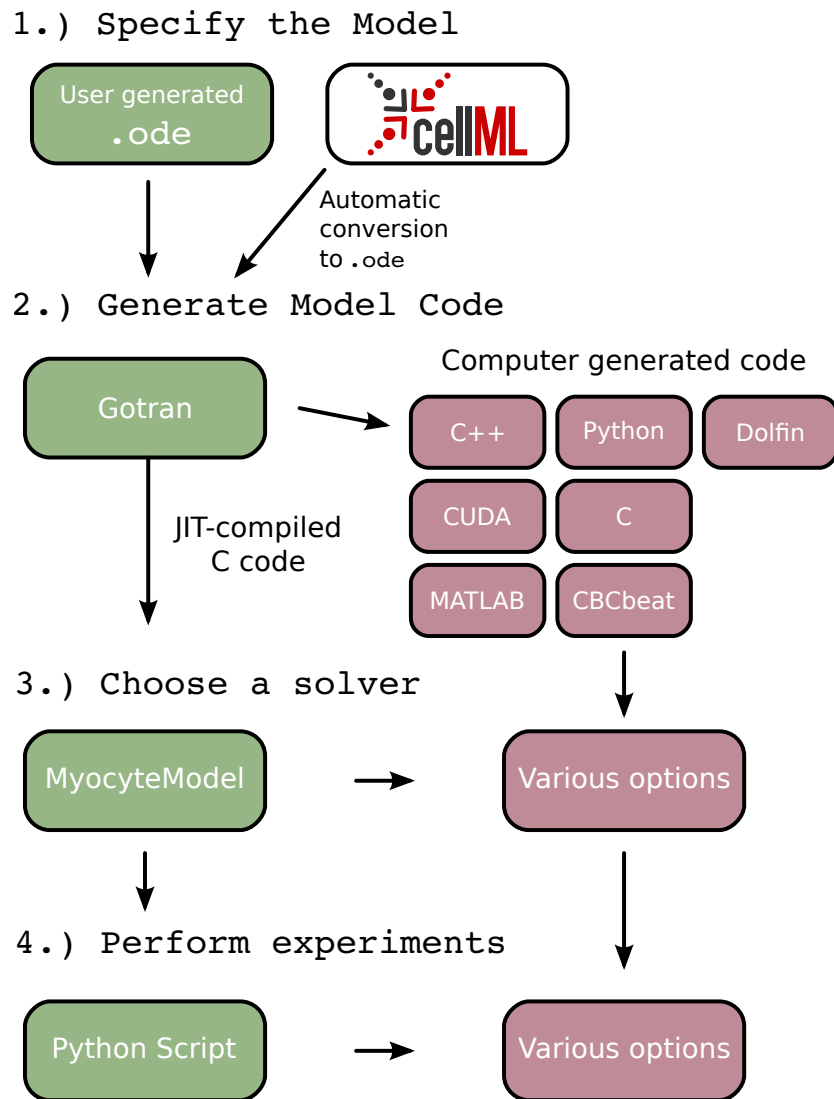


Figure 7.1: Workflow used in this thesis work shown in green, remaining boxes show how the used tools can be combined with other solvers and frameworks. The Koivumäki model was specified in a Gotran .ode-file. Gotran allows for just-in-time (JIT) compilation of C code interface through SWIG. To make scripting of experiments easier and faster we implemented a MyocyteModel-class with methods for setting and getting parameters and state values as well as solving over time and tracking any state variable or intermediate expression specified in the model.

7.3 Verification

When writing code, there is always the possibility of bugs, and so it is important to check whether our implementation is working as intended—this process is known as verification. We need to verify both the `ODEProblem/MyocyteModel`-framework, as well as our implementation of the Koivumäki model itself.

To verify the `ODEProblem/MyocyteModel`-framework we run two test-cases: a simple exponential ODE with a known solution and the Hodgkin-Huxley model. In both cases we compare our computed solutions to known solutions.

To verify our implementation of the Koivumäki model itself, we compare the output given by the `MyocyteModel`-solver with the ouput of the original authors' MATLAB implementation when both are solved with the same numerical scheme and time step.

7.3.1 Test case: Exponential decay

The first test case is a simple model of exponential decay

$$\frac{du}{dt}(t) = -au(t), \quad t \in (0, T], \quad u(0) = u_0. \quad (7.14)$$

To solve this system with our implementation we specify and solve it in the same manner as we will for more complex atrial cell models later. The `.ode`-file used to specify this ODE is shown in Listing 7.2.

Listing 7.2: The `.ode`-file specifying the exponential decay test case.

```
states(u = 2.5)
parameters(a = 0.4)
du_dt = -a*u
```

The ODE can also be solved analytically using separation of variables

$$\frac{1}{u}du = -a \cdot dt \quad \Rightarrow \quad u(t) = u_0 \cdot e^{-at}. \quad (7.15)$$

With a known solution we can calculate the error of the computed numerical solution in each gridpoint

$$e^n = u_e(t_n) - u^n, \quad n = 1, \dots, N. \quad (7.16)$$

where u_e and u is the exact and computed solutions respectively. The n index denotes the meshpoint corresponding to the time $t_n = n\Delta t$. Knowing this error

we can define a scalar measure of the global error, most commonly used is the l^2 -norm, defined as

$$E = \|e^n\|_{l^2} = \sqrt{\Delta t \sum_{n=0}^{N_t} (u_e(t_n) - u^n)^2}. \quad (7.17)$$

In a correct implementation, we expect this error to converge to zero as $\Delta t \rightarrow 0$ following the power law

$$E \simeq C \Delta t^r, \quad (7.18)$$

where the value r , the *rate of convergence*, will depend on the numerical scheme that is being used. By computing a series of errors, E_i , corresponding to a series of time steps, Δt_i , we can compute the rate of convergence from

$$r_i = \frac{\ln(E_{i-1}/E_i)}{\ln(\Delta t_{i-1}/\Delta t_i)}, \quad (7.19)$$

where the convergence rate is also given an index; as it will be slightly different for different pairs of measurements. The power-law behavior shown in equation 7.18 is expected to become more accurate as Δt becomes small, so r_i is expected to converge to the predicted value for the numerical scheme as Δt becomes small.

We test the rate of convergence of the `ODEProblem`-solver using a forward Euler scheme, the results are shown in table 7.1. The forward Euler scheme is a first-order method, meaning the rate of convergence is expected to approach 1. The measured error indicates the implementation has the correct rate of convergence.

It is also useful to check the numerical results of the solver with a different numerical solver, as the chance of two separately implemented solvers having the exact same errors are slim. Solving the ODE using a FE scheme yields the recursive formula

$$u^{n+1} = u^n - au^n \cdot \Delta t. \quad (7.20)$$

which can be solved recursively in any programming language of choice. Comparing the solutions produced by `ODEProblem` with the solution of equation 7.20

Table 7.1: Convergence of error with a decreasing time step for the `ODEProblem` solution using a forward Euler scheme on the exponential decay problem. We find the convergence rate approaches 1, as expected for this first order method.

Δt	10^{-1}	10^{-2}	10^{-3}	10^{-4}	10^{-5}	10^{-6}
E	3.79e-02	3.74e-03	3.73e-04	3.73e-05	3.73e-06	3.73e-07
r	1.07	1.01	1.00	1.00	1.00	1.00

found in NumPy, a scientific programming package for Python, reveals them to be similar in each grid point down to machine precision for all Δt , also for those where the numerical solution is unstable and oscillatory.

7.3.2 Test case: Hodgkin-Huxley model

The exponential decay problem gave some confirmation that the implementation seems to be correct, but our atrial cell models are certainly more complex. For a test case closer to our model, we turn to the Hodgkin-Huxley model. Again we implement the ODE-problem at hand in a `.ode`-file and solve it with the `MyocyteModel`-class. To control the solution, we reproduce a Figure of the neuron action potential from the original paper [[Hodgkin and Huxley, 1952](#)]. Listing 7.3 shows the `.ode` file specifying the HH-model and Figure 7.2 shows the resulting plot used to verify the implementation.

Summary of Verification

We have found the solver to have the correct convergence rate for an exponential decay test case. We have also seen the ability of the solver to correctly reproduce the Hodgkin-Huxley model. In addition, we have compared output from the implemented solver and model with output from the authors' original implementation and found them to give the same results for the same scheme and time step. With these results we consider our implementation sufficiently verified and move on to run virtual experiments on the model.

```

states(V = ScalarParam(-65., unit="mV"),
       m = 0.053,
       h = 0.596,
       n = 0.318)

parameters(
    Cm = ScalarParam(1.0, unit="uF*cm**-2"),
    ENa = ScalarParam(50., unit="mV"),
    EK = ScalarParam(-77., unit="mV"),
    EL = ScalarParam(-54.4, unit="mV"),
    gNa = ScalarParam(120., unit="mS*cm**-2"),
    gK = ScalarParam(36., unit="mS*cm**-2"),
    gL = ScalarParam(0.3, unit="mS*cm**-2"))

# Gating rates, unit = ms**-1
a_m = 0.1*(V + 40)/(1 - exp(-(V + 40)/10))
b_m = 4*exp(-(V + 65)/18.)
a_h = 0.07*exp(-(V + 65)/20)
b_h = 1/(exp(-(V + 35)/10)+1)
a_n = 0.01*(V + 55)/(1 - exp(-(V + 55)/10))
b_n = 0.125*exp(-(V + 65)/80)

dm_dt = a_m*(1-m) - b_m*m
dh_dt = a_h*(1-h) - b_h*h
dn_dt = a_n*(1-n) - b_n*n

INa = gNa * m**3 * h * (V - ENa)
IK = gK * n**4 * (V - EK)
IL = gL*(V - EL)

dV_dt = -(INa + IK + IL)/Cm

```

Listing 7.3: The Hodgkin-Huxley ODE-system formulated in Gotran.

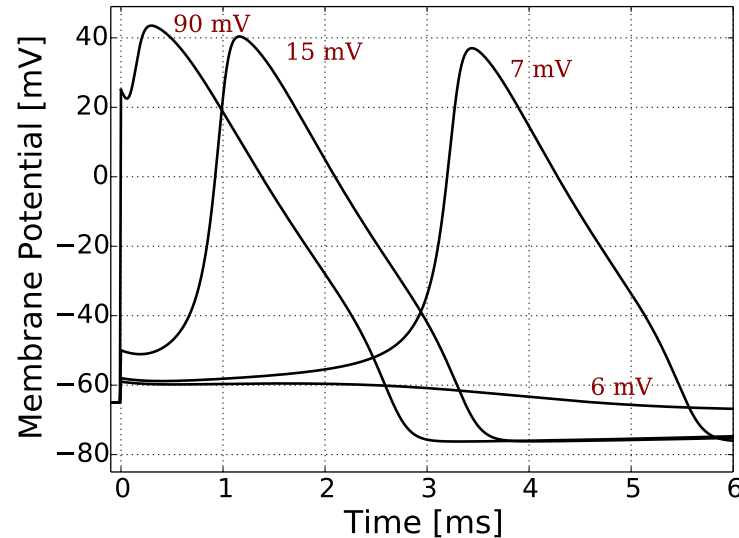


Figure 7.2: Computed solutions from CellModel working on the .ode file shown in Listing 7.3 when different perturbations are introduced in the membrane potential. The red text denotes the amount the membrane potential was depolarized by at time $t = 0$. The Figure is a reproduction of Figure 12a in [Hodgkin and Huxley, 1952].

Chapter 8

Simulation Protocols

Using the implemented models for the human atrial myocyte and human atrial fibroblasts, we are ready to run simulations. Here we give the simulation protocols used, while the results of the simulations are shown in the following Chapter.

We first look at alternans in the Koivumäki model, for both the 2014 and 2015 model variants . Then we turn to the effects of fibroblast-myocyte coupling, this time focusing only the 2015 variant. In all simulations, we solve the model using a forward Euler scheme with a time step of 1 μ s. To see if the chosen time step was acceptable, a selection of the results were also simulated with time steps of 0.1 or 0.01 μ s, with no discernible differences in the results, indicating that the solver is stable for the chosen time step.

8.1 Alternans in the Koivumäki model

The main goal of these simulations is to see to what extent the Koivumäki 2014 and 2015 model variants exhibit alternans and to understand the underlying mechanisms of this behavior. If there are clear differences in the two model variants, the reasons for these differences will be explored.

8.1.1 Dynamic Restitution

To study if the model variants exhibit action potential duration (APD) alternans, we mirror the method used in [Wilhelms et al., 2012]. A restitution curve is produced, which shows how the APD changes as a function of the pacing cycle length (PCL). If alternans are present, a given cycle length will give rise to different action potential durations and the restitution curve will split into two.

To produce the restitution curve, we use the following dynamic pacing protocol:

1. The virtual myocyte is paced for 30 seconds to allow it to reach a semi-stable cycle
2. The APD₉₀ of five consecutive beats are measured. This is the duration from the upstroke of the action potential, until it reaches 90 % repolarization.
3. The PCL is shortened by 10 ms and we start at step 1

To produce the restitution curve, the maximal and minimal measured APD₉₀ for each cycle length are plotted into the same plot. If no alternans are present, the maximum and minimum APD will be the same and the two curves overlap and produce a single trace in the restitution plot. If alternans are present, the maximum and minimum value will be different and the restitution curve bifurcates in the plot.

Due to memory effects of the system, it is important to start at a long cycle length and step down gradually to preserve 1-to-1 capture between the stimulus and action potentials. A starting cycle length of 1000 ms is chosen, and we step down to 100 ms. Note that 100 ms is a very short cycle length, corresponding to a frequency of 600 beats per minute. Such a small cycle length is chosen so that we are assured to get all ranges where the myocyte is successfully firing regularly. If a pacing rate is too fast, the myocyte will fail to excite properly and the resulting peak potential will be very low, leading to an APD₉₀ that is roughly 90 % of the PCL; this will be visible as a triangular spike at the lower end of the restitution curve.

8.1.2 Exploring Alternans Mechanisms

Once the restitution plot is produced, we have insight into the cycle lengths at which the two model variants exhibit alternans. The next step is to explore the mechanisms leading to alternans instability. We can then narrow in on select cycle lengths. To see whether the APD-alternans shown in the restitution curve are occurring simultaneously as calcium transient (CaT) alternans, we track the cytosolic calcium concentration. As it is the subspace calcium that affects the calcium-dependent sarcolemmal currents, we track the subspace and bulk concentrations separately. To plot the bulk cytosolic concentration, we average it over the four non-junctional cytosolic calcium compartments

$$[\text{Ca}^{2+}]_i = \frac{\sum_{k=1}^4 [\text{Ca}^{2+}]_k V_k}{\sum_{k=1}^4 V_k}. \quad (8.1)$$

In addition to the cytosolic calcium concentrations, we plot the SR calcium concentration. We do this because alternating diastolic SR load is one of the main proposed mechanisms of calcium alternans (see Section 3.8.2). For the SR calcium, we track the junctional-SR, i.e., compartment 4, and the non-junctional SR, i.e, the average of compartments 1–3, separately.

In addition to tracking the membrane potential, calcium transient and SR load over time, we track some ion fluxes and gating mechanism in the model. These help us to pin down what is driving the alternans in the model. We look at

- L-type calcium channel flux, $J_{\text{Ca,L}}$.
- Calcium inactivation of the LTCC, f_{Ca} .
- Calcium release flux from the SR through the RyR, J_{rel} .
- Ryanodine receptor activation, inactivation and adaptation gates.

The L-type calcium channel (LTCC) is important, as it is hugely impactful on intracellular calcium concentrations through calcium induced calcium release. It is the most important way for the APD to affect the calcium dynamics of the myocyte. The calcium inactivation of the LTCC is also important, as it is the main mechanism by which the intracellular calcium dynamics affect the membrane potential, as a calcium-inactivated LTCC is expected to reduce APD. The calcium release flux is interesting to track, as it is an alternating SR release flux that is expected to drive alternans in the calcium transient. The gates of the ryanodine receptors are important to track to see if they become refractory, as this is also a plausible mechanism (see Section 3.8.2).

In addition to tracking the fluxes over time, we compute total flux per cardiac cycle

$$Q_L = \int_{t_i}^{t_{i+1}} J_{\text{Ca,L}} dt = \int_{t_i}^{t_{i+1}} -\frac{I_{\text{Ca,L}}}{2F} dt, \quad (8.2)$$

$$Q_{\text{rel}} = \int_{t_i}^{t_{i+1}} \sum_x J_{\text{rel},x} dt. \quad (8.3)$$

where i denotes the cycle number and x the different SR compartments. Summing the contributions from all SR compartments allows us to find the total SR release. From this we can compute the excitation-contraction coupling (ECC) gain, which is defined as the ratio of the total SR release to the total LTCC influx

$$\text{ECC}_{\text{gain}} = \frac{Q_{\text{rel}}}{Q_L}. \quad (8.4)$$

To integrate the fluxes, we numerically integrate the tracked values of the fluxes using a trapezoidal rule.

8.1.3 Model Differences

To understand any differences observed in alternans behavior of the two models, we take a closer look at their calcium dynamics. The changes made to the K2015 are:

- A new formulation of I_{Na} current.
- Updated rectifier current parameters for I_{Kr} and I_{Ks} .
- The potassium currents I_{KAch} and I_{KCa} have been added.
- The sodium-potassium pump, NKA, has been updated.
- The transient outward current, I_{to} , conductance has been increased.
- The L-type calcium current has been reformulated, with a significant reduction in the maximum conductance ($15 \text{ nS} \rightarrow 7 \text{ nS}$).
- The model temperature has been adjusted from 33°C to 37°C .

Of these changes, we expect the L-type calcium current to have the largest impact on the calcium dynamics of the model. The updated rectifier currents affects the late component of the action potential. The SK-channel, I_{KCa} , has a low conductance and is therefore of little importance in this context. We have ignored I_{KAch} in our present simulations. The reformulations of I_{Na} , I_{to} , and $I_{\text{Ca,L}}$ lead to a stronger early repolarization of the action potential, but do not strongly affect intracellular Ca^{2+} cycling. The reformulation has led to a more classically spike-and-dome shaped action potential (see Fig. 8.1).

To see how the changes to the model have affected the intracellular calcium dynamics, we will compare the L-type calcium flux, calcium release, and spatiotemporal calcium transients of the two model variants. The spatiotemporal transient is found by interpolating the cytosolic compartment Ca^{2+} concentrations, giving the concentration as a function of distance into the cytosol and time.

To see if the strongly reduced max conductance of the L-type current can account for the changes observed, we look at how the models change with \bar{g}_{CaL} , which we vary in the range $[5 \text{ nS}, 15 \text{ nS}]$ in steps of 0.025 nS . For each value of the max conductance, we create a restitution curve, as detailed in the previous Section. For every PCL we calculate the difference in maximal and minimal APD observed:

$$\Delta \text{APD}_{90}(\text{PCL}) = \max (\{\text{APD}_{90}^i\}_{i=1}^n) - \min (\{\text{APD}_{90}^i\}_{i=1}^n), \quad (8.5)$$

where the i index denotes the different measured beats at each cycle lengths, and n the number of measured beats, which we set to 5. We then plot out ΔAPD_{90} as a function of PCL and \bar{g}_{CaL} . This results in a heatmap which indicates at what cycle lengths APD-alternans are found, and their magnitude, as the L-type

conductance changes. The resulting plots are shown in the next Chapter, see Figures 9.8 and 9.9 on page 115.

To examine the effects of the other changes as opposed to that of the L-type current, we create a *hybrid* model variant of the 2014 and 2015 variants. This is done by taking the K2015 and reverting the formulation of the L-type channel completely, so that it matches the formulation of the 2014 variant. For the hybrid model variant, we produce a heatmap of APD magnitude as a function of PCL and max L-type conductance.

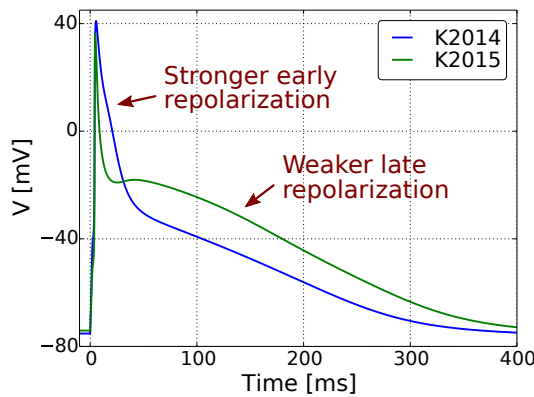


Figure 8.1: The 2015 model variant has a more spike-and-dome shaped action potential due to stronger early repolarization (upregulated I_{to} and weakened peak of $I_{Ca,L}$) and weaker late repolarization (weaker outward rectifying K^+ currents and longer-lasting LTCC current).

8.2 Fibroblast-Myocyte Coupling

To study the effects of fibroblast-myocyte coupling on the Koivumäki model we, use the two active fibroblast models proposed by Maleckar et al, in addition we include two passive fibroblast models parameterized to have the same resting membrane potential as the active models. We denote our four model variants as Active I, Active II, Passive I, and Passive II.

The fibroblast resting membrane potential (RMP) is -48.7 mV for the I-models and -31.4 mV for the II-models. Both passive fibroblasts have a leak-conductance of 0.093 nS, which corresponds to a resistance of 10.7 G Ω , which is what Maleckar et al used for their passive fibroblast leak conductances. This leak conductance assures that the active and passive models have comparable decay rates of the membrane potential, see Figure 8.2.

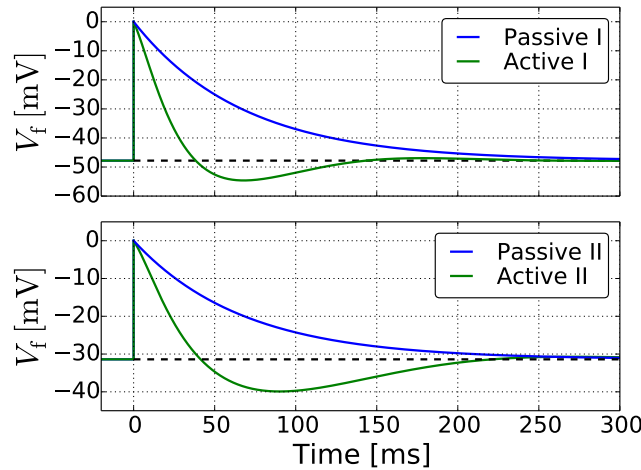


Figure 8.2: Decay of fibroblast transmembrane potential in isolation following an excitation to 0 mV. The two passive model variants have been parameterized to have identical RMPs and comparable decay rates back to RMP following a depolarization.

For the fibroblast-myocyte coupling itself, we use a non-specific Ohmic gap junction current for simplicity, as there are few good measurements of ion-specific conductances in m-f pairs. [Rook et al., 1992] measured the conductance of gap junctions in m-f pairs in cell cultures and found them to vary between 310 pS and 8 nS. To reflect this we look at gap junction conductances in the range

$$G_{\text{mf}} \in [0, 8.0 \text{ nS}],$$

where we move from the control case of no coupling (0.0 nS), to weak coupling (0.5 nS), to medium coupling (4.0 nS) to strong coupling (8.0 nS). We look only at single-sided connections with 1–4 fibroblasts being coupled to a single myocyte.

After coupling 1–4 fibroblasts of a given type to a virtual myocyte, the myocyte-fibroblast system will find a new steady-state under regular pacing. To make sure the system is not affected by the original, uncoupled initial conditions of the myocyte or fibroblast in isolation, we pace the m-f system for at least five minutes at a cycle length of 1000 ms before making any measurements. If any measurements are to be taken of the system at any other cycle length than 1 second, we first equilibrate the coupled system at a 1 second PCL, and then gradually shorten or lengthen the pacing rate in increments of 10 ms to preserve 1-to-1 capture.

Specific Simulations

First, we look at changes in the myocyte action potential morphology as more fibroblasts are coupled to the virtual myocyte. For each fibroblast model, we look at the steady-state AP at a cycle length of 1000 ms for 0–4 coupled fibroblasts for weak (0.5 nS) and strong coupling (8.0 ns).

As the virtual fibroblasts have a higher resting membrane potential than the virtual myocyte, we expect FMC to lead to a depolarization of the myocyte resting membrane potential. To see how this effect works, we plot out the RMP as a function of number and type of coupled fibroblasts.

We expect the sodium channel to be less available as a result of a depolarized RMP. To understand why, see the activation parameters of the Koivumäki model in Figure 8.3. As the RMP of the myocyte increases we see that the inactivation gates drop lower, while the activation gate grows stronger. While both activation and inactivation thus get a ‘head start’ on the AP, we expect this effect to be stronger for the inactivation due to its slower response time. The net result is expected to be a weaker sodium current. To see if this is the case, we integrate the fast and late components of the sodium current over a cardiac cycle to find the total flux of the current

$$Q_{\text{Na},F} = \int_0^{\text{PCL}} I_{\text{Na},F} dt, \quad (8.6)$$

$$Q_{\text{Na},L} = \int_0^{\text{PCL}} I_{\text{Na},L} dt, \quad (8.7)$$

$$Q_{\text{Na}} = Q_{\text{Na},F} + Q_{\text{Na},L}. \quad (8.8)$$

We plot the measured fluxes against the number of coupled fibroblasts for the different fibroblast types and coupling strengths.

The sodium channel is responsible for driving the upstroke of the action potential, and reduced availability is expected to lead to a weakened upstroke, or excitability, of the myocyte. To examine if this is the case for the Koivumäki model, we plot the measured maximum upstroke velocity, dV/dt_{max} , and action potential amplitude for the different numbers of coupled fibroblast of the different types. We plot our data points as a function of the measured RMP of those points to see if there is a trend in the effect of FMC on RMP and reduced myocyte excitability.

In addition to a depolarized RMP, we expect FMC to reduce myocyte excitability through additional electrotonic load on the myocyte. To see how impactful this effect is compared to the shift in RMP, we look at the control case of an isolated myocyte without any FMC. For the control myocyte, we raise the resting membrane potential by increasing the extracellular potassium; this raises the Nernst potential for potassium for the cell and thus the I_{K1} -channel mainly responsible

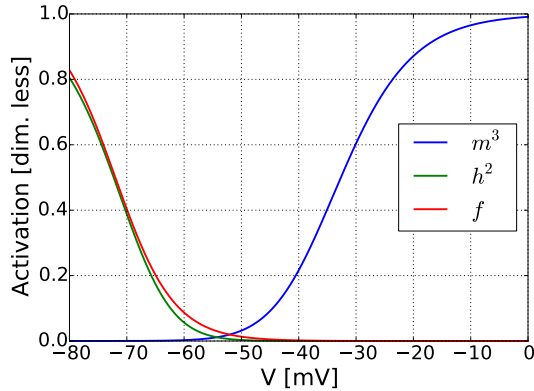


Figure 8.3: Steady-states of the gates of the sodium channel formulation in the Koivumäki model. Both the fast and late component of the sodium current use three m -gates for activation. The fast component inactivation is caused by two h -gates, while the late component is inactivated by a single f -gate. Note that while the steady-states of the gating mechanism allows for very little sodium flux, the activation gate is faster than the inactivation gates ($\tau_m > \tau_f > \tau_h$). However, during diastole all gates are given enough time to reach their steady state. An increased resting membrane potential therefore reduces the availability of both sodium components through the inactivation gates.

for the action potential is less effective. We vary the extracellular potassium concentration in the range

$$K_o \in [5.4 \text{ mM}, 25 \text{ mM}]. \quad (8.9)$$

Starting at 5.4 mM (the standard concentration in the model), we gradually increase the concentration in steps of 0.1 mM. For each increase, we pace the myocyte for five minutes before measuring the resting membrane potential, maximal upstroke velocity and action potential amplitude.

In the next Chapter we present the results of the simulations we have outlined here.

Chapter 9

Results

Here, we present the results of the simulations outlined in Chapter 8. First, we present the results of our studies of alternans behavior of the 2014 and 2015 Koivumäki model. Next, we look at the effects of fibroblast-myocyte coupling on the Koivumäki virtual myocyte.

9.1 Alternans in the Koivumäki Model

The measured restitution curves of the models are presented, showing at what pacing cycle lengths (PCLs) the models exhibit alternans. Next, we show a closer look at the model behaviors at select cycle lengths chosen from the restitution curves.

Restitution Curves

The restitution curves produced for the 2014 and 2015 versions of the Koivumäki models (K2014/K2015) are shown in Figure 9.1. The Figure shows large differences in the alternans behavior of the two model variants. The 2015 variant has an APD₉₀ (duration from upstroke until action potential is 90 % repolarized) that is about 50 ms longer for a cycle length of 1 s, and thus has a steeper restitution curve as the pacing rate is increased. Both models are seen to exhibit APD-alternans. The 2015 version has two pockets of alternans at cycle lengths of roughly 425–550 ms and 650–850 ms, as seen from the bifurcation of the restitution curve. In comparison, the 2014 version has only a single pocket of alternans found at the shorter cycle lengths of 200–350 ms. The magnitude of the changes in APD are larger in the K2014, both in absolute and relative measurements. At low cycle lengths, both models eventually experience failed excitation, as seen

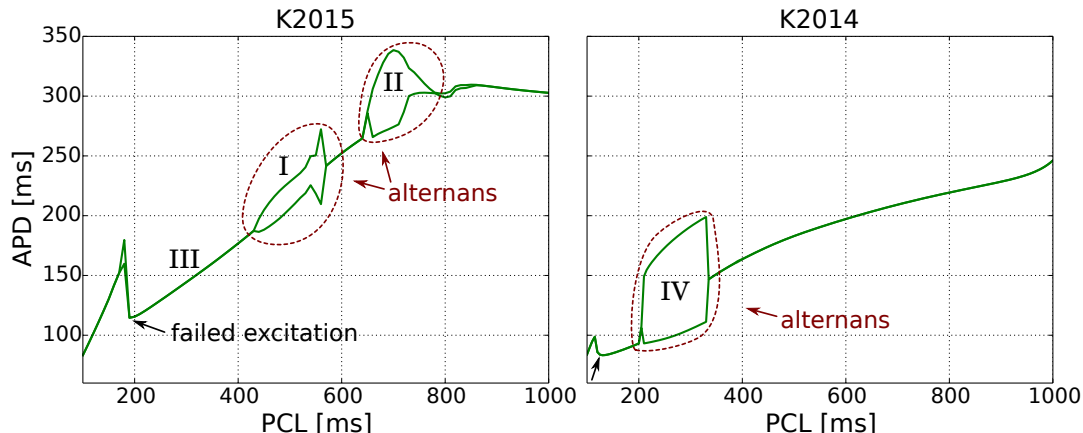


Figure 9.1: Restitution curves for the Koivumäki model. Red arrows point to regions where alternans are present, as seen from the bifurcation of the restitution curve. Black arrows indicates the cycle length where excitation fails. (**K2015**): 2015 formulation of the model, two regions of alternans are seen at longer cycle lengths. (**K2014**): 2014 formulation of the model, a single region of alternans is seen at short cycle lengths. The Roman numerals indicate regions of interest.

from the triangular ‘bump’ at short cycle lengths. The point of failed excitation occurs at a longer cycle length for the 2015 variant.

From the restitution curve, there are three distinct regions where alternans are exhibited in the two model variants. These areas are designated areas I, II and IV (see Figure 9.1. For these three regions we look at cycle lengths of 500, 700 and 250 milliseconds. Region IV corresponds to the alternans in the K2014. To understand why the K2015 exhibits no alternans at the same short cycle lengths we also look closer at the K2015 for a PCL of 250 ms, designated area III in the restitution plot.

Region I

Figure 9.2 shows five consecutive cycles of the K2015 paced at a cycle length of 500 ms, corresponding to region I in the restitution plot (Fig. 9.1).

From panel (a) there are visible period-2 action potential duration (APD) alternans, with relative changes of 10 % in APD from beat to beat. There are also period-2 alternans in the calcium transient (CaT), seen in panel (b), with relative changes of roughly 50 % in $[Ca^{2+}]_i$. The alternans are electromechanically concordant, i.e., the APD- and CaT-alternans are in phase.

There are also clear beat-to-beat variations in the SR Ca^{2+} concentration tran-

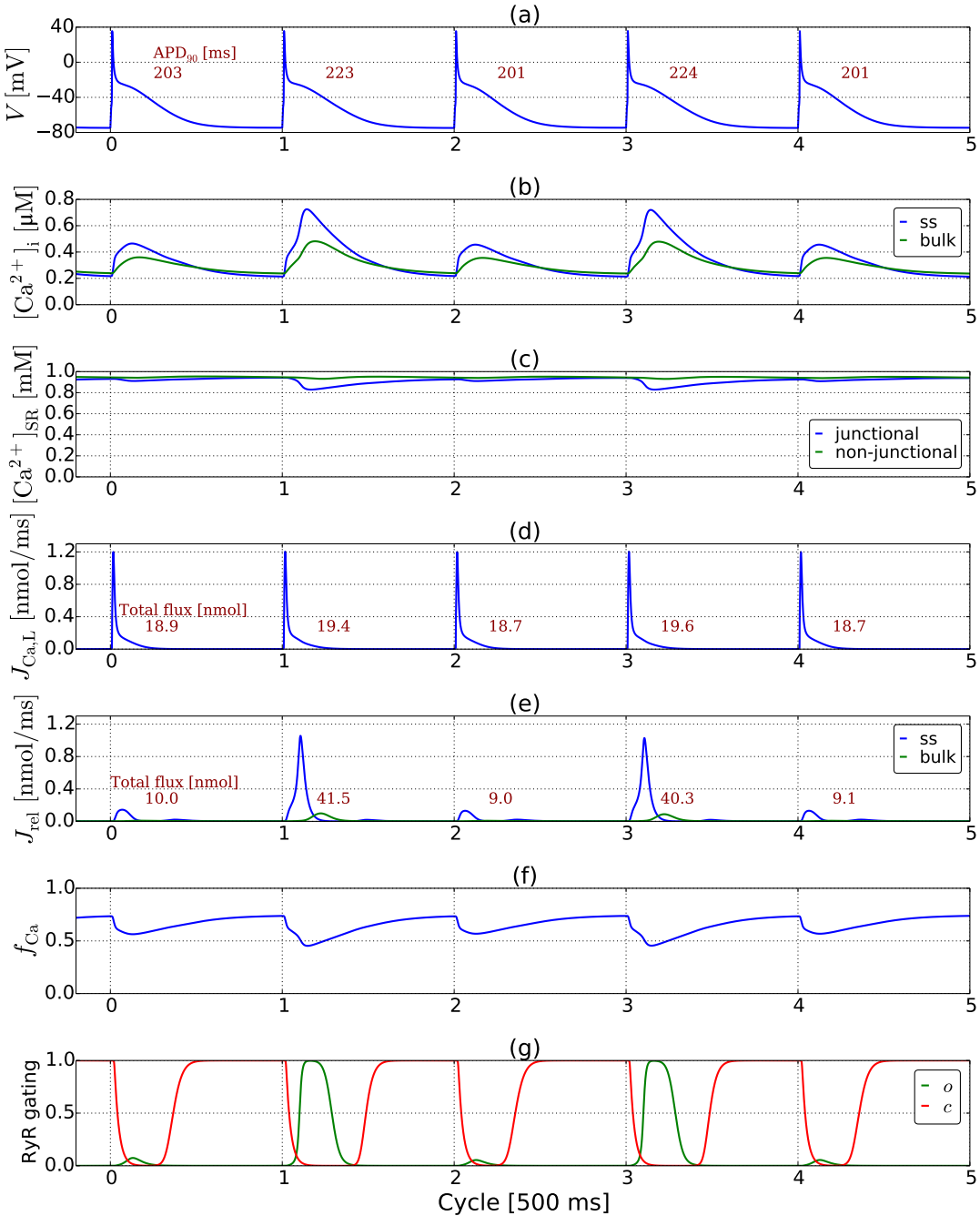


Figure 9.2: Five consecutive beats of the 2015 model variant of the Koivumäki model being paced at 500 ms, corresponding to region I in the restitution plot (fig 9.1). Clear alternans are seen in APD (a), CaT (b) and SR transient (c). There are strong variations in SR release flux (e) and weak variations in LTCC flux (d). There are no alternans in *diastolic* cytosolic (b) or SR calcium concentration (c). Strong beat-to-beat variations are seen in the RyR activation, but not inactivation (g).

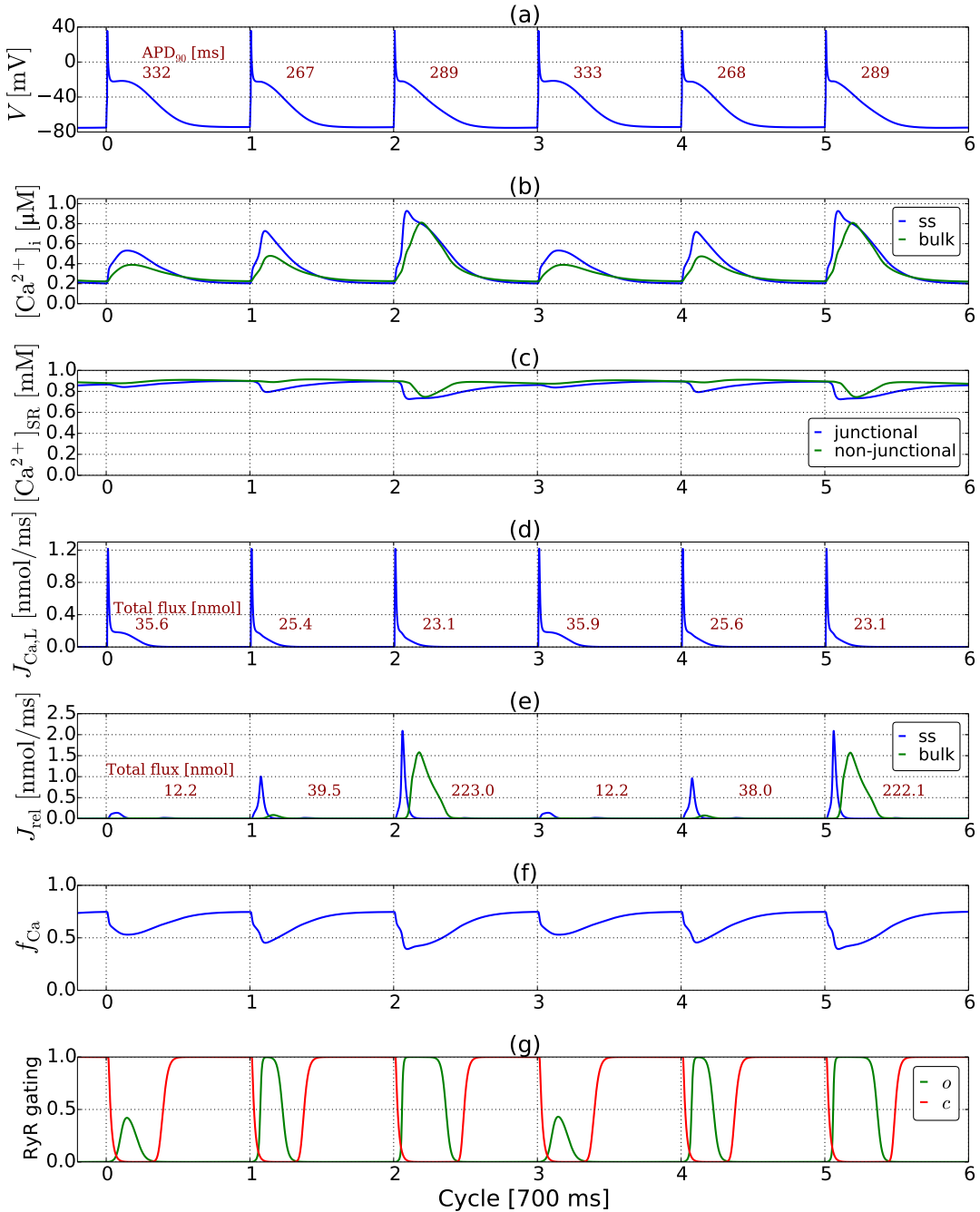


Figure 9.3: K2015 at a PCL of 700 ms, i.e., region II in Figure 9.1. The model is exhibiting stable period-3 alternans. Clear alternans are seen in APD (a), CaT (b) and SR calcium concentration (c). In addition to SR transient variations, the diastolic SR load is slightly lower every third beat. The calcium release flux shows very strong variations (e); the LTCC also shows beat-to-beat variations (d), but these variations are small compared to the variations in the release flux.

sient, panel (c). The diastolic SR load, the SR calcium concentration at the start of a cardiac cycle, show no clear variations from cycle to cycle. Compared to the cytosolic variations the absolute changes in SR concentration are much larger (note different units on the y-axis for panel (b) and (c)); this is due to the SR's smaller volume.

Next the influx of calcium through the L-type calcium channel is shown in panel (d), which sees very weak beat-to-beat changes, with a changes of 3-5 % in the total flux between beats. The LTCC alternates in phase with the APD, and out of phase with the calcium-inactivation ($1 - f_{Ca}$), shown in panel (f). In comparison to the LTCC, the RyR release flux shown in panel (e) is alternating much more drastically, with relative changes 330 % from beat to beat. A drastically alternating release flux coupled with a nearly constant LTCC flux gives very different excitation-contraction coupling (ECC) gains, with strongly coupled beats having a gain of 2.0, while weekly coupled beats have a gain of 0.5.

Looking at the gates of the RyR in panel (g), we see strong beat-to-beat variations in the activation gate (o), which fully activates every other beat, but then reaches a peak of less than 0.1 the other beats. The inactivation gate (c), on the other hand, has the same time evolution every cycle.

We will return to these results, and explain them, in our discussion of the underlying alternans mechanisms, which will be given in Section 10.1.1.

Region II

Figure 9.3 shows six consecutive cycles of the K2015 at a 700 ms PCL, corresponding to region II in the restitution plot (Fig. 9.1).

We now see clear period-3 patterns, which is quite different from the period-2 pattern found at region I. The pattern seems quite stable, as the traces for the first and fourth, second and fifth, and third and sixth cycles seem identical. Panel (a) shows the APD first falls by 19 %, before growing back up in steps of 6 % and 13 % in following cycles. In panel (b) the same is seen in the peak cytosolic concentration (panel b), which gradually grows stronger before falling back down. The diastolic levels of cytosolic calcium at the onset of every beat is constant, as it was for region I. Panel (c) shows diastolic SR load, which is slightly lower every third beat. The APD-alternans and CaT-alternans are no longer in phase, and the largest APD is concurrent with the smallest calcium peak, meaning these alternans are electromechanically discordant.

The LTCC flux, panel (d), is larger than it was for region I, due to a longer APD, but it also experiences larger relative beat-to-beat changes. The largest LTCC flux is concurrent with the largest APD, but the smallest LTCC occurs with the

middle APD due to calcium inactivation of the LTCC, panel (f), following a very large release flux. The RyR release flux, shown in panel (e), is out of phase with the LTCC, having the largest release when the LTCC is the smallest. It has a very large release every third beat, roughly 17 times bigger than the weakest release; this is seen to be caused by a large junctional release triggering an even larger non-junctional release. The ECC gain is 0.4, 1.4 and 9.5, giving weakly, medium and very strongly coupled beats, respectively.

Panel (g) shows the gates of the RyR. The behavior is much like in region I. The inactivation has no beat-to-beat variations, while the activation gate has clear variations—only reaching half-maximum in the weakest beat, and then getting progressively stronger.

Region III

Figure 9.4 shows five consecutive cycles of the K2015 at a 250 ms PCL, corresponding to region III in the restitution plot (Fig. 9.1).

We see a very stable cardiac cycle with no beat-to-beat variations. From panel (b), the diastolic calcium levels at the onset of each cycle is markedly higher than for region I and II, but with smaller calcium transients, yielding lower peaks. The RyR gates in panel (g) show only very slight activations every cycle, giving a comparatively very small SR Ca release, shown in panel (e). Note the y-axis is an order of magnitude smaller than for the region I/II Figures. The ECC gain is small due to the low release flux; at 0.5 it is comparable to the weakly coupled beats of region I and II.

Region IV

Turning to the K2014, Figure 9.5 shows the five consecutive cycles of the model at a 250 ms PCL, corresponding to region IV in the restitution plot (Fig. 9.1).

Looking at panel (a) we see that the model is exhibiting not only action potential duration alternans, but also action potential amplitude (APA) alternans. The APD-alternans are also very large, with relative changes of about 45 %, much more than the 9–19 % changes we saw in region I and II for the JKK2015. Note that the membrane potential at the onset of the AP also varies, as the myocyte does not have time to completely recover. The cell is being paced very rapidly at this point (a cycle length of 250 ms corresponds to 240 beats per minute) and we can see that the long beats are effectively of the same duration as the cycle length.

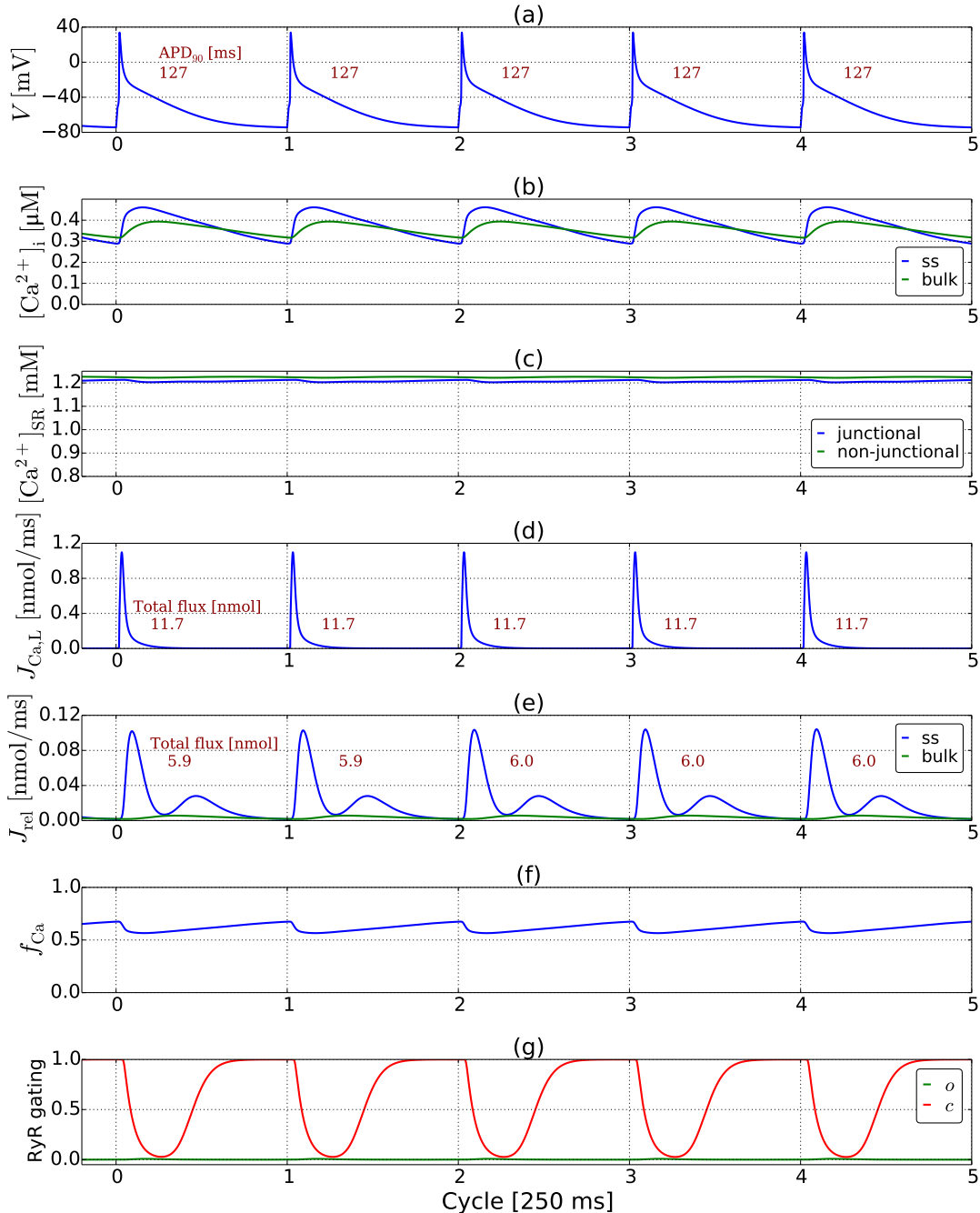


Figure 9.4: K2015 at 250 ms PCL, i.e., region III in Figure 9.1. No alternans are present and the system seems stable from cycle to cycle. The release flux is very small (d) (note the scale of the y-axis), due to the activation of RyR failing completely (g). The SR calcium load (c) is considerably higher than in region I and II. The diastolic calcium level (b) is also higher than I and II, but the amplitude of the calcium transient is much smaller, giving smaller CaT-peaks.

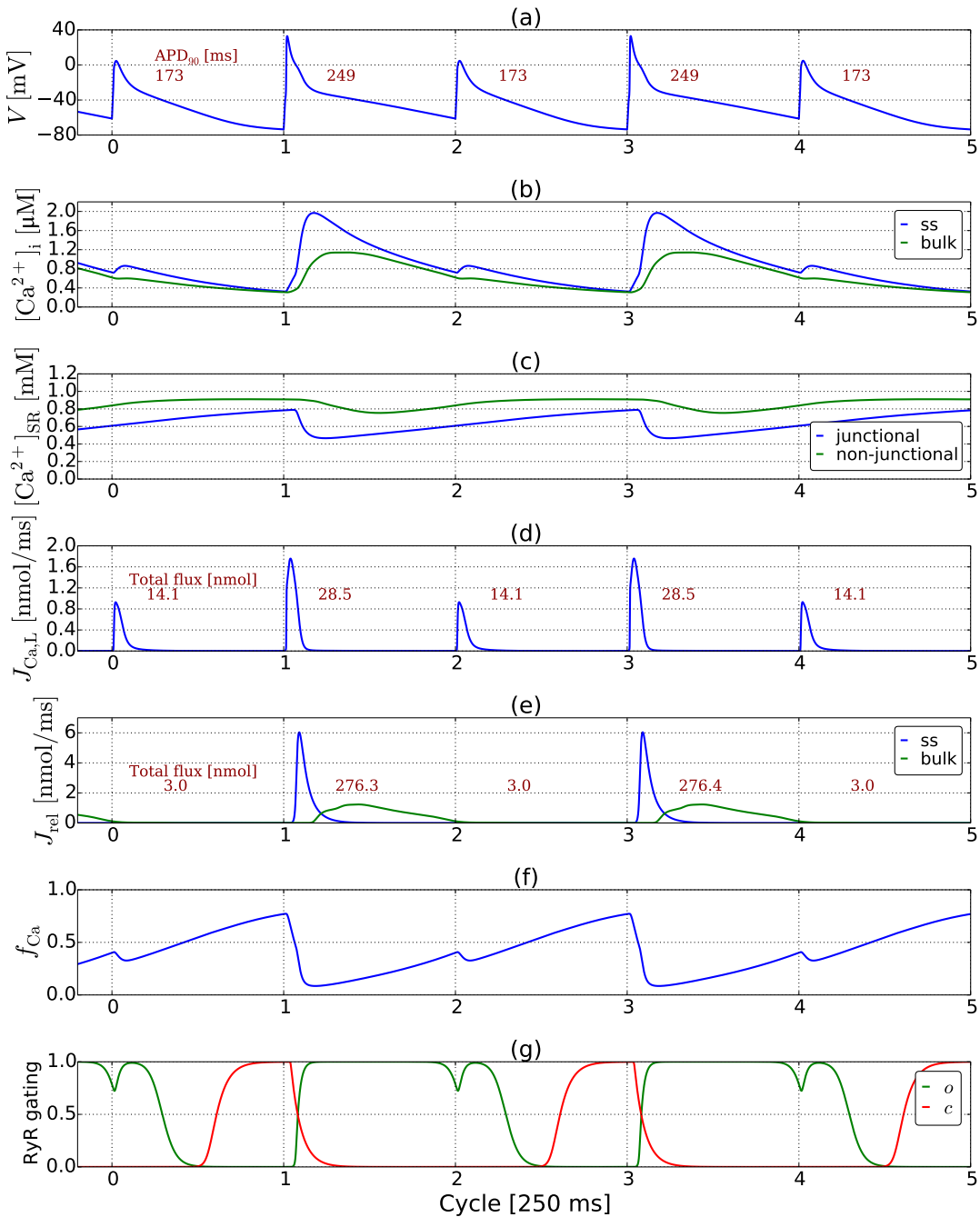


Figure 9.5: Five consecutive beats of the JKK2014 at a PCL of 250 ms, corresponding to region IV in Figure 9.1. Period-2 alternans are seen in all variables. In addition to AP duration alternans, there are clear AP amplitude alternans (a). The beat-to-beat variations seen are very large. Calcium release only occurs every other cycle (e), leading to a very large calcium transient (b) that requires two cycles to return to the same diastolic level.

In panel (b), we also see much stronger CaT-alternans in this variant, with a relative change of over 400 % in cytosolic calcium concentration. These are electromechanically concordant alternans as the CaT and APD alternate together, in phase. The peak calcium concentration is very high compared to the concentrations seen in the K2015, and the myocyte is clearly calcium overloaded. Every other beat there is practically no increase in calcium, and it requires two cycles to return to the same diastolic calcium levels.

From the trace of the SR calcium concentration, shown in panel (c), there is a much higher fractional release, of about 45 %, compared to at most 10 %, for the JKK2015. However, this release occurs only every other beat, seen in panel (e), with practically nonexistent release each other beat. The LTCC, shown in panel (d), is also alternating more strongly, with a relative change in both amplitude and total flux of about 100 %, also in phase with the APD.

Panel (g) shows the RyR gates are both alternating in a period-2 fashion. The weak release flux is seen to be primarily due to the inactivation gate being refractory throughout every other beat.

9.1.1 Model Differences

Figures 9.6 and 9.7 show the comparisons of the L-type and release currents and spatiotemporal calcium transients of the two models at cycle lengths of 1000 ms, 700 ms, 500 ms and 250 ms. The three shortest cycle lengths correspond to regions I, II, III and IV in the previous Section.

From Fig. 9.6 (a) and (c) we see that the total L-type and release fluxes are about the same in magnitude, but the K2014 has a shorter-lasting current with a peak almost twice as large in both L-type and release current. From panels (b) and (d) we see that the larger peaks in both Ca^{2+} currents leads to a transient with a higher peak concentration in the K2014.

From Fig. 9.6 (e) and (g) we see the two models at a cycle length of 700 ms. The K2014 exhibits no alternans, but the K2015 does. The L-type flux of the K2014 is roughly the same as at 1000 ms, while the K2015 has seen about a 15 % reduction in the current. The release current of the K2014 has been reduced by about a third. The K2015 has a strongly varying release current which is much lower than the K2014 for the weak cycle and slightly larger at the strong cycle. Taking the average of the two cycles, the K2014 flux has about a 40 % larger release flux. Again we see the K2015 to have longer-lasting currents with higher peaks. In (f) and (h), the calcium transients now look very different for the two models. For the K2015, the weak calcium cycle sees a very weak transient that doesn't reach very far into the cell. The strong calcium cycle doesn't see as large

a peak as the K2014 transient, but it reaches far into the cell, a result of a large bulk Ca^{2+} SR release.

Fig. 9.7 (a) and (c) show the Ca^{2+} -currents at a PCL of 500 ms. The L-type calcium current is again quite similar for the K2014, but the K2015 L-type flux has been reduced to about two thirds of the flux at 1000 ms. The release flux of the K2014 has reduced to roughly half, while the K2015 again has an alternating release flux it is very weak compared to the K2014 for both beats. In Figure 9.7 (b) and (d) we see that this leads to a very weak calcium transient for the K2014.

The situation at a PCL of 250 ms is shown in Figure 9.7 (e) and (g), where we see the L-type of the K2015 is about one-third of the flux at 1000 ms, with a smaller flux than both cycles of the alternating K2014 flux. The K2015 exhibits almost no release flux whatsoever, while the K2014 has a very large release flux every other cycle versus non-existent release flux. The calcium transients shown in (f) and (h) are now completely different. The K2014 shows an enormous calcium transient that lasts longer than a single cycle length, merging together two cycles in the transient. The K2015, on the other hand, has such weak calcium currents that no real transient is seen at all.

Altering the L-type Calcium Conductance

Results of altering the L-type conductance of the models are shown in Figure 9.8. For both model, we observe large changes in behavior as the conductance changes from below 8 nS to above it. From Fig. 9.8b, we see only slightly increasing L-type conductance pushes the alternans behavior to shorter pacing cycle lengths and results in behavior more resembling the K2014. The K2014 originally has a conductance of 15 nS; from Fig. 9.8a we see that reducing this by small amounts has little effect on alternans behavior. If the conductance is set to the 7 nS found in the 2015 model version, however, there is a significant change in behavior. The alternans occurs longer PCLs. At 6 nS, the K2014 shows alternans at PCLs as long as 700 ms, which is still well below the cycle lengths where the K2015 features alternans.

In our study of the alternans behavior of the two models, we found the K2014 to exhibit alternans that were larger in magnitude. Comparing Figures 9.8a and b reveals the K2015 exhibits the largest alternans of the two if the L-type conductance is increased slightly (note the different scales on the colorbars). If the K2015 conductance is increased further, above 11–12 nS, the alternans become weaker again.

Figure 9.9 shows the ΔAPD heatmap of the K2014/K2015 hybrid model where the L-type formulation of the K2015 has been reverted. The heatmap looks like a mixture of the two maps found for the two model variants (Fig. 9.8a and b),

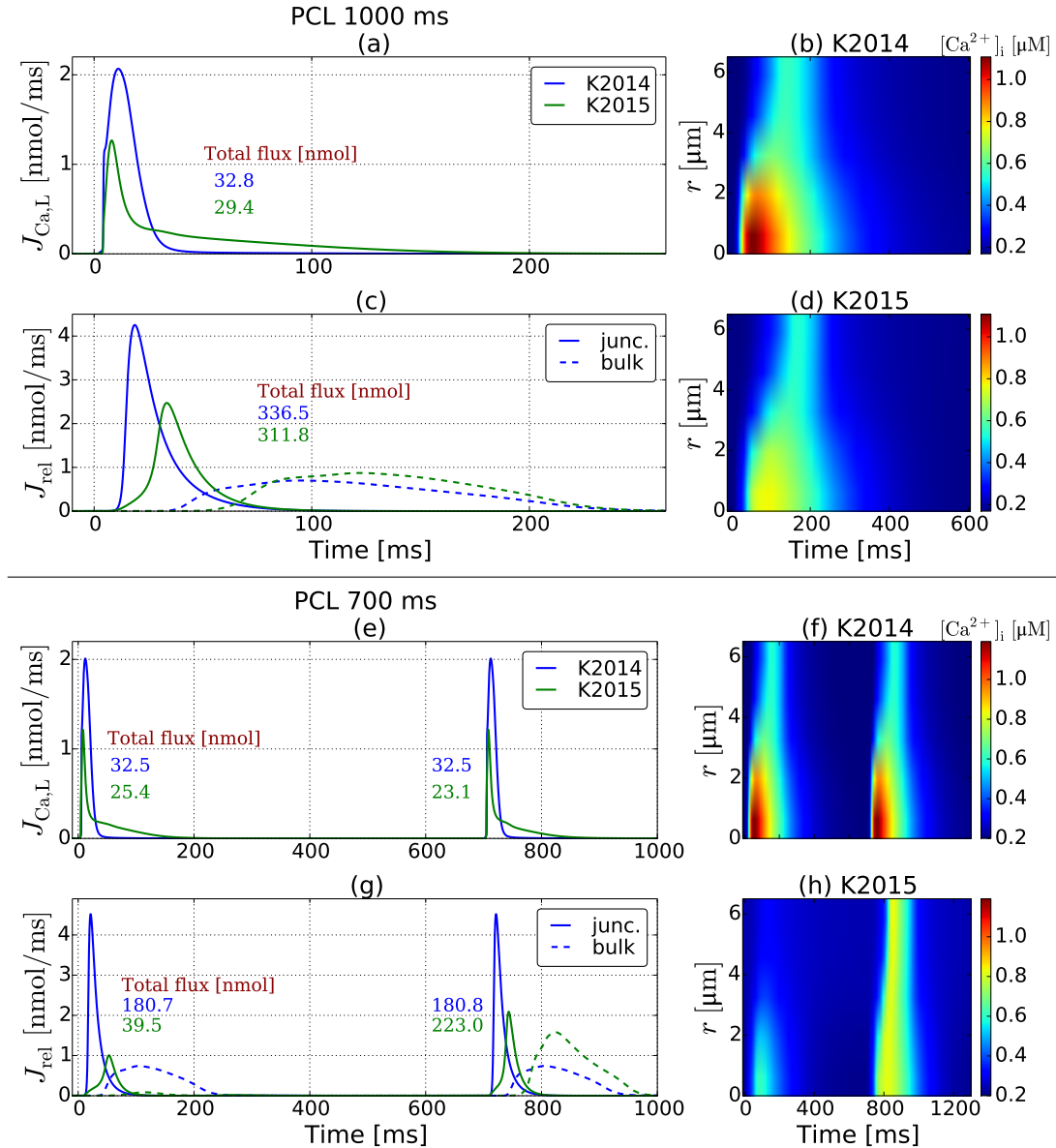


Figure 9.6: Comparison of the calcium transients of the two model variants. (a), (e): L-type calcium current, (c), (g): SR calcium release, (b), (d), (f), (h): Spatiotemporal view of the calcium transient, with r denoting distance into the cytosol. Differences in the calcium transients of the two models are seen. The total flux of both L-type calcium and SR currents are comparable, but the K2014 has a short-lasting current with a larger peak leading to a more concentrated transient.

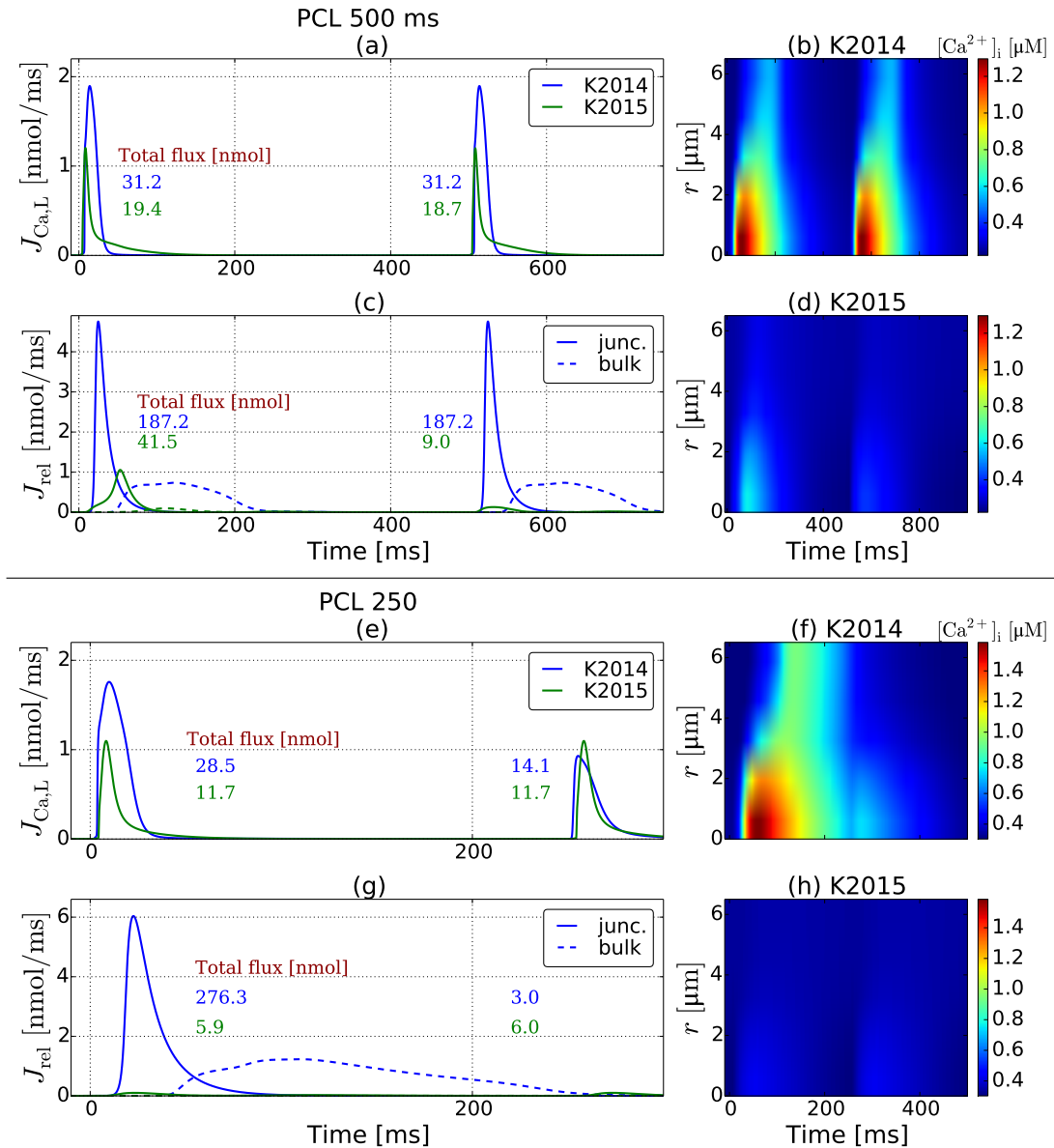


Figure 9.7: Comparison of the calcium transients of the two model variants. (a), (e): L-type calcium current, (c), (g): SR calcium release, (b), (d), (f), (h): Spatiotemporal view of the calcium transient, with r denoting distance into the cytosol. Large differences in the calcium transient are seen, with the K2015 transient being nearly non-existent in comparison to the K2014 transient, due to a much lower L-type current and extremely low release current.

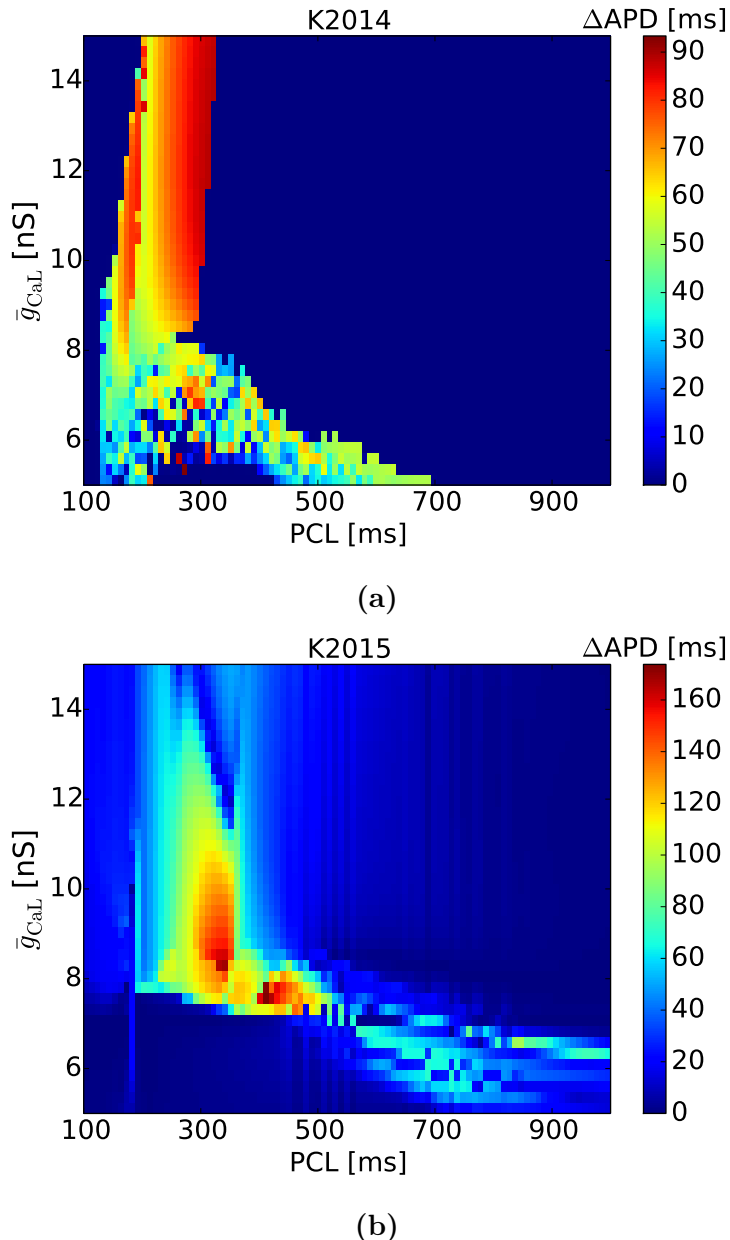


Figure 9.8: Magnitude of cardiac alternans observed as function of pacing cycle length (PCL) and maximal L-type calcium current conductance, \bar{g}_{CaL} . **(a):** 2014 formulation of the Koivumäki model. **(b):** 2015 formulation of the Koivumäki model. The magnitude of alternans is found by the dynamic restitution protocol described in Section 8.1.1 on page 95. Significant changes in alternans behavior are seen as the L-type conductance is changed, with both model variants having the biggest change in behavior around 7–8 nS. The native value of the conductance for the two models is 7 nS for the K2015 and 15 nS for the K2014.

with the behavior of both model variants. Alternans are seen at very long cycle lengths for low conductances. As the conductance is increased the alternans get pushed to shorter PCLs. Around 7 nS the alternans increase in magnitude. As the conductance is increased past 10 nS the alternans behavior is quite stable in both the cycle lengths they appear and the magnitude.

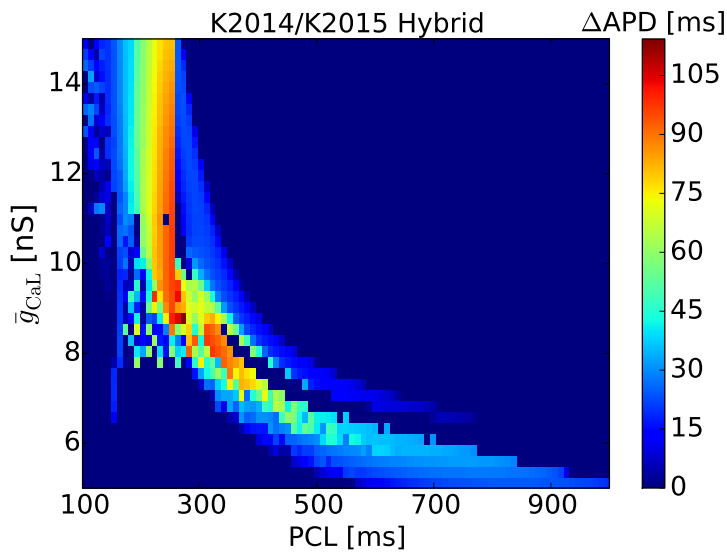


Figure 9.9: Magnitude of cardiac alternans observed as function of pacing cycle length (PCL) and maximal L-type calcium current conductance, \bar{g}_{CaL} for a hybrid of the K2014 and K2015. The magnitude of alternans is found by the dynamic restitution protocol described in Section 8.1.1 on page 95. The hybrid model was created by reverting the L-type calcium channel to the 2014 formulation. The resulting behavior can be seen as a mixture of the K2014 and K2015 (see Fig. 9.8a and b). At low L-type channel conductances alternans are seen at very long cycle lengths. As the L-type conductance is increased, the alternans occur at shorter cycle lengths. After the L-type conductance increases above roughly 10 nS, the change in behavior is smaller as the L-type conductance is increased further, with the alternans occurring at roughly the same cycle lengths and decreasing only slightly in magnitude.

9.2 Effects of Fibroblast-Myocyte Coupling

Here, we present the results of our studies on the effects of FMC on the Koivumäki model.

9.2.1 Action Potential Morphology

Figure 9.10 shows how the myocyte action potential at a 1000 ms cycle length changes due to FMC, for weak and strong coupling to 0–4 fibroblasts of all four variants.

We see that FMC causes significant changes to the myocyte AP shape. For all cases, we see a depolarization of the myocyte resting membrane potential and a clear reduction in the action potential amplitude. These modulations only increase with the number of coupled fibroblasts and coupling strength. The shape of the AP also fundamentally changes due to the FMC, but the exact modulations are different depending on the fibroblast variant, coupling strength and number of fibroblasts. A general observation is that the AP notch seems significantly reduced or removed in all cases. Due to the changes in the RMP and APA, seeing a clear pattern in APD from the Figure alone is challenging. For the fibroblasts of type I (those with the highest fibroblast resting potential), only the most extreme APA reduction causes the AP to never cross 0 mV, and even in that case there is still a discernible AP present. For the II-models, however, there seems to have been a significant change in the myocyte resting potential, as it jumps from below -60 mV to close to -40 mV going from 2 to 3 coupled fibroblasts. At these resting membrane potentials, the action potential amplitude is severely diminished and the myocytes are no longer excitable.

9.2.2 Reduced Sodium Channel Availability

Figure 9.11 shows how the resting membrane potential of the myocyte changes due to FMC, and the resulting changes in the sodium current.

We see that the results are very similar for the three coupling strengths, with only a slightly larger depolarizations seen as the coupling strength is increased. For all four fibroblast types, the RMP increases monotonically as more fibroblasts are added, while the magnitude of both components of the sodium flux decrease monotonically.

The perturbation of the myocyte RMP is seen to be significantly smaller for the I-fibroblasts; it is also more linear with the number of attached fibroblasts. The II-fibroblasts cause larger depolarizations in the myocyte RMP. A significant

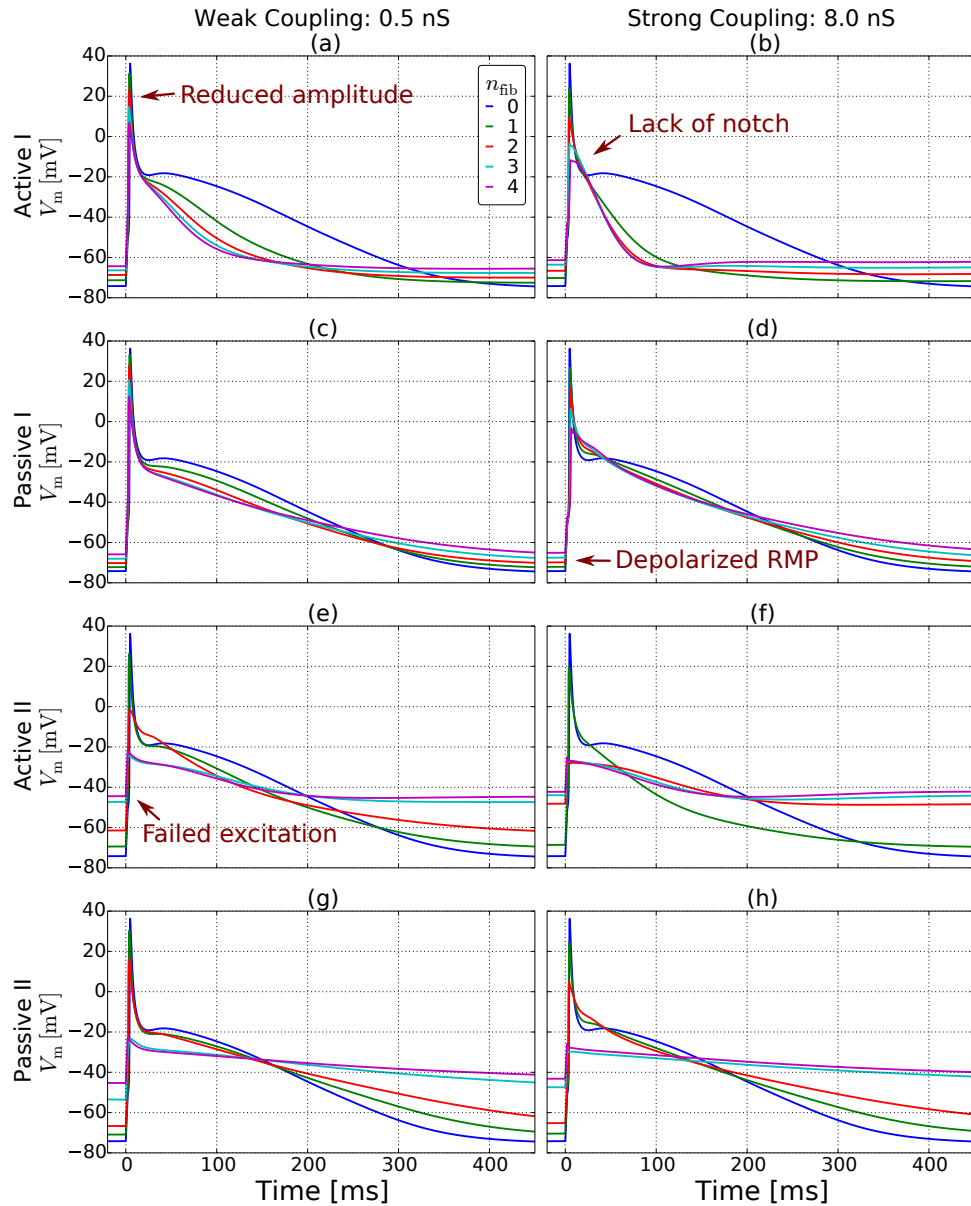


Figure 9.10: Myocyte action potential at a cycle length of 1000 ms when coupled to n_{fib} fibroblasts of different types with weak (0.5 nS) and strong (8.0 nS) coupling. Arrows indicate points of interest. In all cases a reduction in action potential amplitude and a depolarization of myocyte resting membrane potential is observed. Both of these effects are seen to be stronger with a greater number of coupled fibroblasts. The shape of the action potential changes as a result of FMC, where we see that the notch of the action potential is significantly diminished in all cases. For 3 or 4 coupled fibroblasts of type-II the myocyte is no longer excitabile, with only a very small increase in the membrane potential following stimulation.

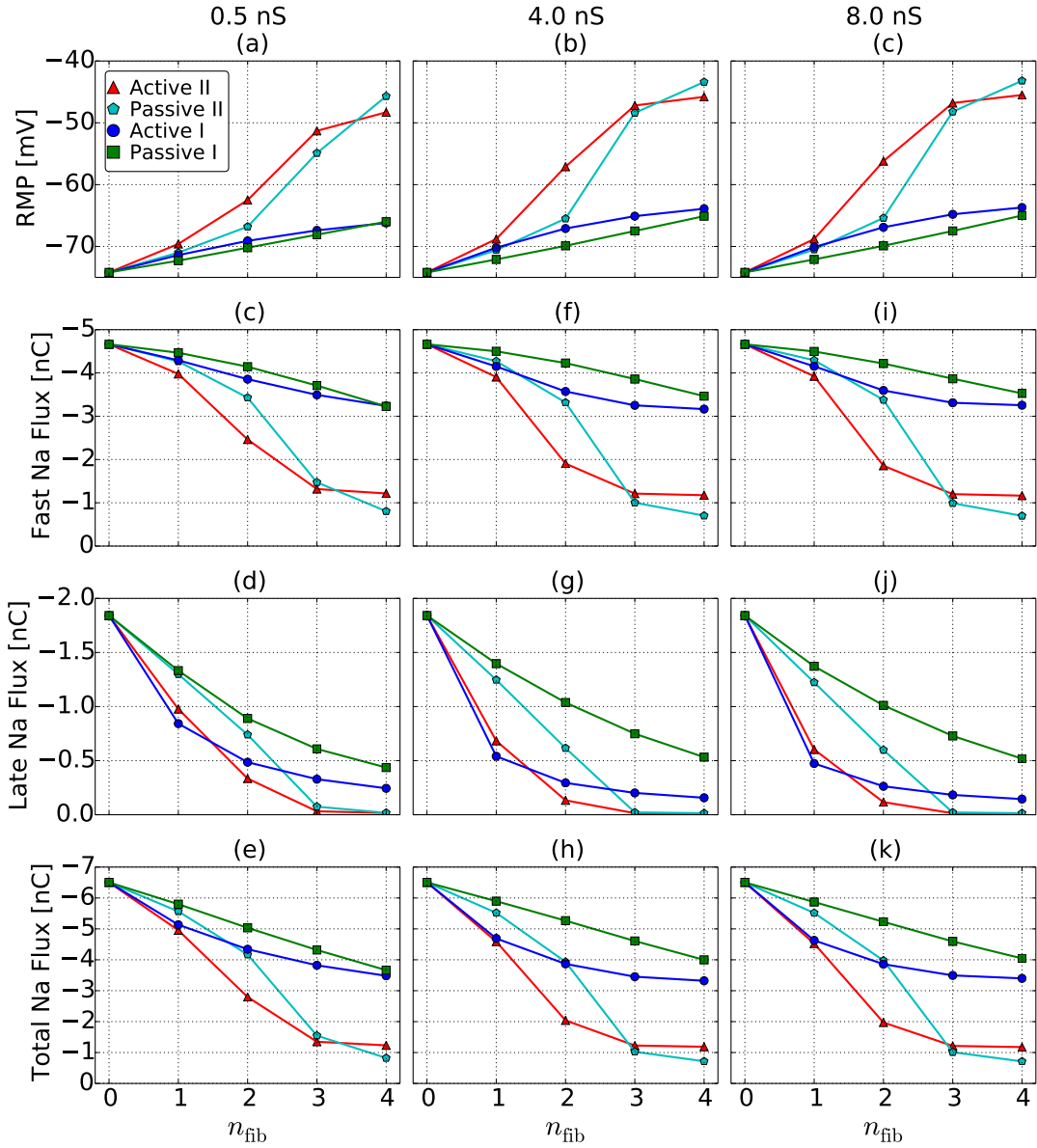


Figure 9.11: Perturbation of resting myocyte membrane potential and resulting sodium current flux when coupled to n_{fib} fibroblasts of different types at different coupling strengths. For all fibroblast types, the RMP increases monotonically with the number of coupled fibroblasts. For the type-I fibroblasts, the change in RMP is near-linear in the number of fibroblasts, while for the type-II a clear change in behavior is seen as the RMP approaches -60 mV. For the sodium current we see a decrease in available sodium channels as the RMP is depolarized. The decreased availability of sodium channels when the myocyte is coupled to the type-I fibroblasts is near-linear, but a large drop in sodium current is seen as the RMP increased above -60 mV, making the cell unexcitable.

jump in the RMP is seen when moving from 2 to 3 attached type-II fibroblasts. This jump occurs as the RMP is approaching roughly -60 mV.

For the I-fibroblasts, the total flux of the fast component of I_{Na} falls almost linearly with the change in the RMP, while the late component falls more drastically as the RMP is slightly depolarized and then flattens out when the RMP is depolarized further by increasing the number of fibroblasts.

When attached to type-I fibroblasts, the total sodium flux is reduced by roughly 10 % per attached fibroblast, and so is quite significant when attached to four fibroblasts. The reduction in I_{Na} is much more significant when coupled to 3 or 4 type-II fibroblasts, as the flux sees a significant drop when the RMP depolarization takes a large step with this coupling.

9.2.3 Myocyte Excitability

Figure 9.12 shows measured values of maximum upstroke velocity (dV/dt_{max}) and action potential amplitude (APA) for 0–4 connected fibroblast of different types. The data points are divided into three figures, based on coupling strength. In each figure, the best linear fit is also shown. Data points with an RMP of more than -60 mV have been ignored for the regression analysis, as Figure 9.11 showed drastic behavior change when the myocyte RMP was depolarized to this range.

We see a clear linear decrease in both upstroke velocity and AP amplitude as myocyte RMP is depolarized, with $R^2 > 0.95$ in all cases. From the linear behavior, we see the upstroke velocity is expected to hit 0 at around roughly -60 mV, but as the RMP crosses this point the upstroke velocity stabilizes at 11.5 mV/ms; the upstroke velocity resulting from the external stimulus current. While the APA also is close to linear when $RMP < -60$ mV, it does not approach 0 as RMP approaches -60 mV. The APA is also seen to stabilize at 20–25 mV as the RMP is increased above -60 mV. This is in the range expected to be resultant of only the external stimulus pulse, which leads to a depolarization of 22.5 mV.

The measured dV/dt_{max} and APA of the FMC systems were plotted against the control case of an isolated myocyte with a depolarized RMP achieved through increased extracellular potassium concentration. This is shown in Figure 9.13.

We see that the RMP of the control myocyte gradually depolarizes as $[K^+]_o$ is increased. The maximum upstroke velocity decreases monotonically with the depolarizing RMP. It is seen to decrease close to linearly until the RMP is slightly above -60 mV, where it begins to flatten out, stabilizing at 11.5 mV/ms. For APA as a function of RMP, things are more complex. The AP amplitude is seen to decrease close to linearly until roughly -60 mV, where V_{peak} crosses under 0 mV. This changes the slope of the APA as a function of RMP, which is quite flat

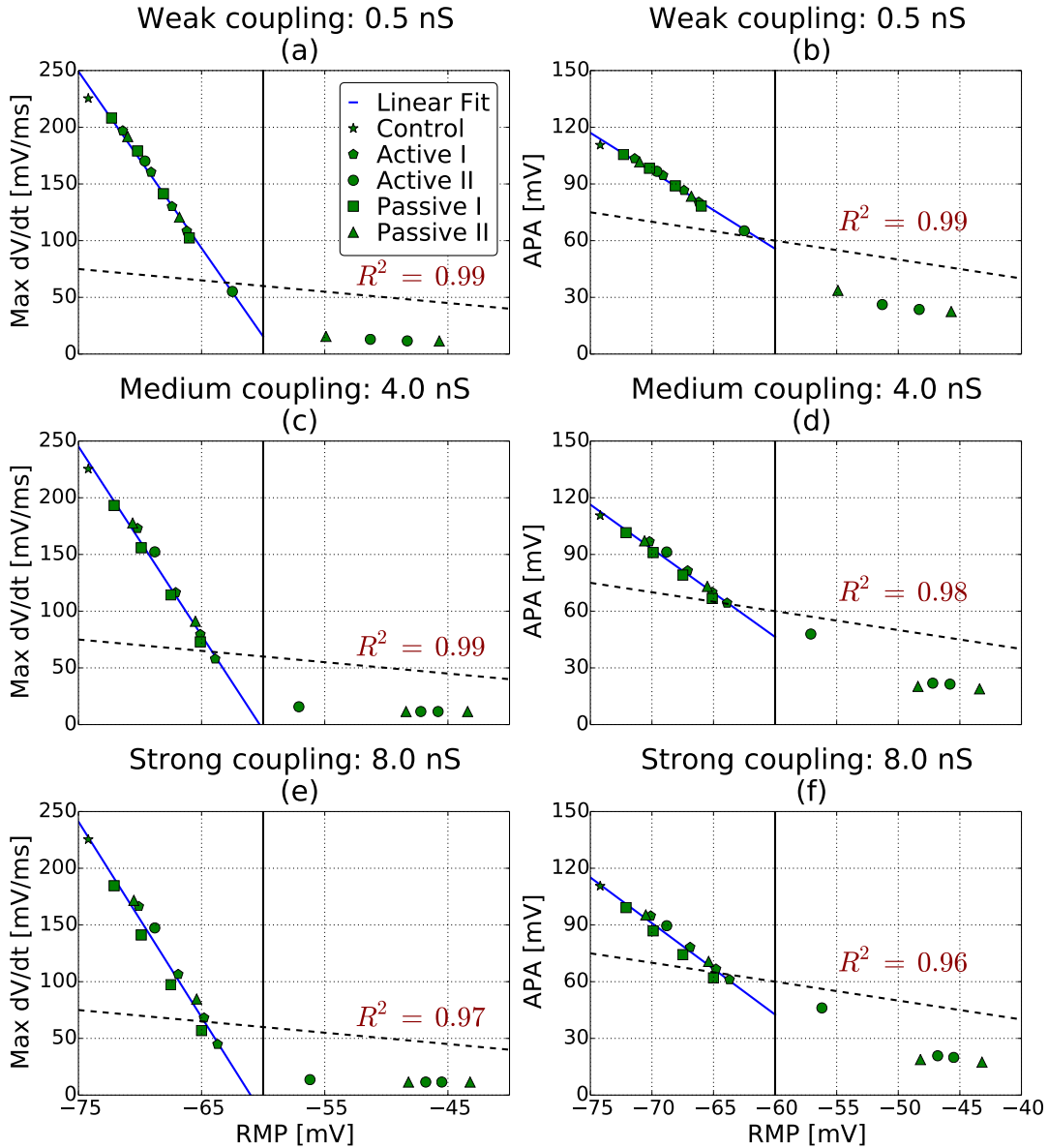


Figure 9.12: Measured Action Potential Amplitude and maximal upstroke velocity as functions of RMP of myocyte-fibroblast systems. The solid vertical black line denotes the point of where RMP drops significantly and the cell lost excitability completely (see Fig. 9.11). Data points with an RMP above the line have been ignored for the purposes of regression. The diagonal dashed line denotes the APA needed for the myocyte potential to cross above 0 mV. The blue line is a least-squares best fit linear function. The R^2 value of the fit is shown in red text. Each plot corresponds to data from all fibroblast models for a given coupling strength.

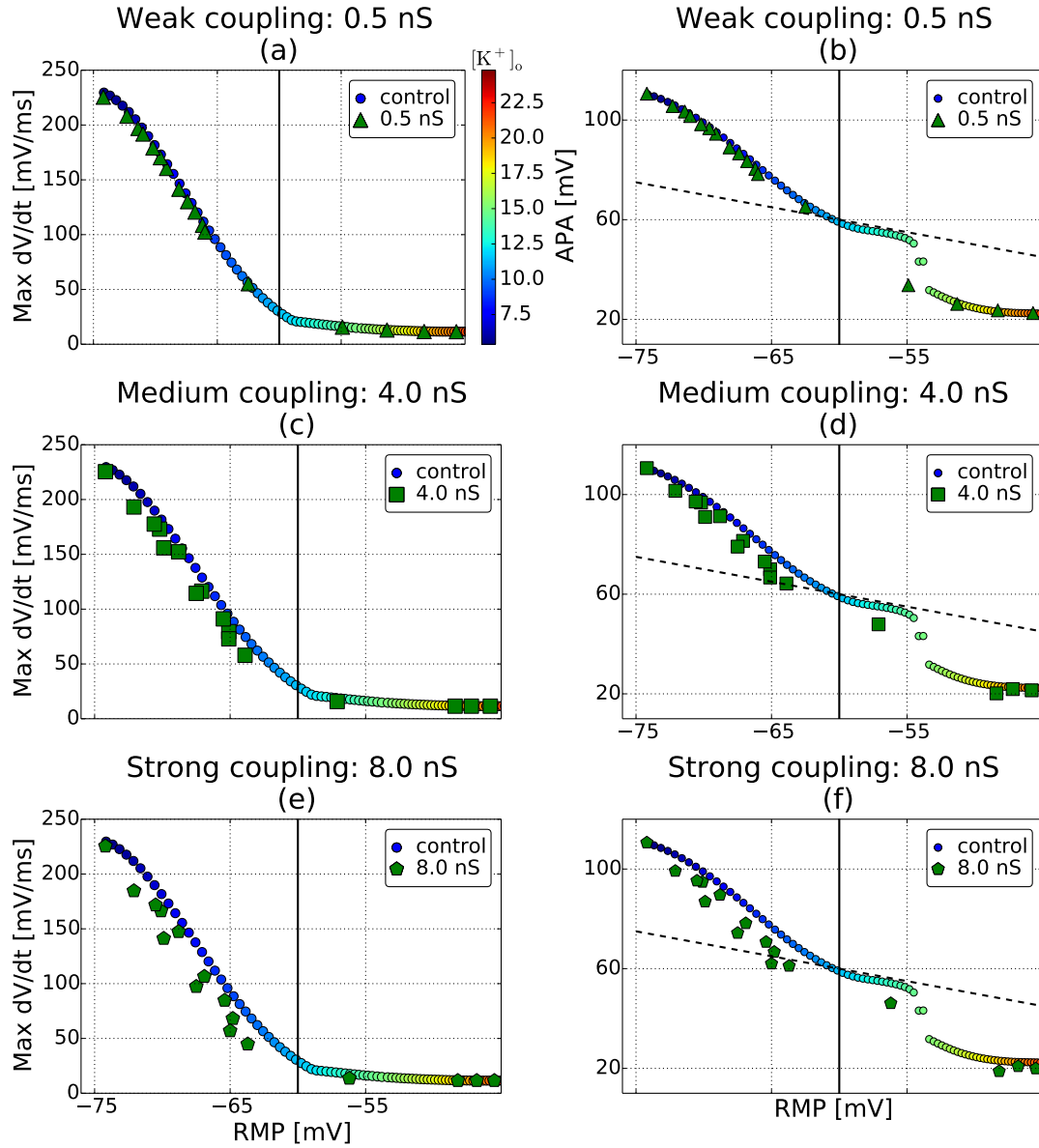


Figure 9.13: Measured APA and dV/dt_{\max} as functions of RMP myocyte-fibroblast systems (larger green markers) overlaid APA and dV/dt_{\max} as functions of RMP for a control myocyte (smaller circles with color indicating extracellular potassium concentration). The control myocyte data is similar for each of the three plots on the left, and for the three plots on the right. The FMC data has been divided by coupling strength. The solid black line indicates the -60 mV threshold used for linear regression of the FMC data (see Fig. 9.12), the dashed line indicates where the APA is large enough for the peak myocyte membrane potential to exceed 0 mV.

from -60 mV until about -55 mV, before suddenly dropping very rapidly before stabilizing at 22.5 mV as the RMP is increased further.

When the FMC data is overlaid with the measurements from the control myocyte driven to increased RMP via increased extracellular potassium concentration, we see the two agree quite well. The results measured on the FMC system are consistently below those from the increased potassium control case, with the disagreement growing in strength with increased strength of coupling.

Chapter 10

Discussion

10.1 Alternans Behavior of the Koivumäki Model

We have seen clear alternans behavior in both the 2014 and 2015 formulations of the Koivumäki model (Fig. 9.1). Compared to the findings of [Wilhelms et al., 2012], which we presented in Figure 4.3 on page 41, we see that the K2014 and K2015 features considerably more alternans than all the other models with exception of the Grandi model. It is especially interesting to note that the 2014 and 2015 formulations of the K model feature more alternans than the 2011 variant which was used for benchmarking by Wilhelms et al. We also found that the K2014 and K2015 models to have very different alternans behavior than that of the 2011 variant and from one another.

The three formulations of the K-model are by large very similar, with most expressions and parameters being the same or having only subtle differences. The largest differences between the three, especially in regards to alternans, is the formulation of the L-type calcium current, which we see has yielded three very different alternans behaviors.

10.1.1 Mechanisms of the K2015

The alternans found in the K2015 were both electromechanically concordant and discordant, depending on the pacing cycle length (PCL). In our review of the literature, we saw that restitution driven alternans could only be electromechanically concordant, while calcium-driven alternans could be both concordant and discordant. This indicates that the alternans must be at least partially calcium-driven.

The SR calcium release flux was found to alternate strongly, and can account for any other beat-to-beat variations through $\text{Ca}^{2+} \rightarrow V$ coupling. The release flux was seen to be caused by the activation gate of the RyR (See panel (g) in Fig. 9.2 and 9.3). The question is *why* the activation gate is fluctuating from beat to beat. The two main theoretical candidates for alternating release current are alternating diastolic SR calcium load and refractoriness of ryanodine receptor (RyR) release channel (see Section 3.8.2 on page 29).

The *diastolic* SR calcium load was found to be very close to constant in both region I (Fig. 9.2c) and region II (Fig. 9.4c), with only slight variation in the latter case following the largest release current. Although these diastolic SR fluctuations *seem* far too small to cause the variations seen in the release flux, it is easy to rule them out entirely by clamping the diastolic SR concentration. This is done by adjusting the SR concentration to a fixed value at the onset of every cardiac cycle. When we do this, we observe the exact same model behavior as when no clamp is present, showing that in this case the diastolic SR fluctuations are not the cause of the alternans.

Next we have RyR refractoriness. From the formulation of the RyR (see Section 5.3.2 on page 60), we see that the activation and inactivation gates only depend on the cytosolic calcium concentrations and the adaptation variable, which again only depend on the cytosolic calcium concentration. The cytosolic calcium concentration was found to have beat-to-beat variations (Fig. 9.2b, 9.3c), but the variations are mostly seen in the early part of the calcium transient, while the *diastolic* concentrations are identical every beat. The activation and inactivation gates are quite rapid ($\tau_a = 4.3\text{--}16$ ms and $\tau_c = 13\text{--}74$ ms), meaning the gates cannot ‘remember’ the peak of the previous calcium transient. The refractoriness of the activation gate cannot therefore be directly caused by different cytosolic calcium concentrations, but must instead rely on the adaptation variable. The adaptation variable changes much more slowly than the gates themselves ($\tau_a = 850$ ms), and can therefore be affected by the entire calcium transient and not only the diastolic concentration.

There now seem to be two possible explanations for the alternating release flux. Either it is caused by the steady state activation’s direct dependence on the $[\text{Ca}]_i$, or the dependence through adaptation, or a combination of the two. As the activation gate is so fast, the direct dependence can be thought of as an instantaneous cytosolic calcium dependence. The indirect dependence through the adaptation variables is much slower and so is instead a dependence on the history of the calcium transient, i.e., the preceding calcium transient.

The cytosolic calcium concentration is the same at the beginning of every cycle. A different $[\text{Ca}^{2+}]_i$ must therefore be caused by a larger LTCC flux. Although the observed difference in the LTCC flux is very small (Fig. 9.2d), it is feasible

that the slight difference is enough to either fail or succeed in triggering a self-driving calcium-induced calcium-release. To examine if this is the case, we rerun the simulation, this time clamping the LTCC current. To clamp the LTCC, we add a new calcium current to the model, $I_{\text{Ca,clamp}}$. During the first cycle, we let the clamp current be zero and record the L-type calcium current. The recorded current is the new ‘target’, $\hat{I}_{\text{Ca,L}}$. In the following cycles, the clamp current is set to compensate for the real L-type current

$$I_{\text{Ca,clamp}}(t) = \hat{I}_{\text{Ca,L}}(t \bmod \text{PCL}) - I_{\text{Ca,L}}, \quad (10.1)$$

where the modulus is used to map the current time to the first cycle, $t \bmod \text{PCL} \in [0, \text{PCL})$. The net result of this clamp current is that the sum of the LTCC and clamp current, $I_{\text{Ca,L}} + I_{\text{Ca,clamp}}$, is identical and equal to the target LTCC current every cycle.

When clamping the L-type current in region I (Fig. 9.2) the alternating release current is still present, but the differences in release flux are smaller. The smaller flux has increased 10–15 % and the larger flux has reduced 25–30 %. The results are roughly the same when clamping the weak and strong LTCC-cycle. From this, we conclude that the alternating L-type calcium channel increases the magnitude of the calcium transient alternans present, but are not the direct cause of them.

That leaves the activation gate’s dependence on the adaptation variable. Plotting the adaptation gate through the cardiac cycle reveals it to be slightly different at the onset of every cycle. To see if this difference is large enough to account for the beat-to-beat variations in the model, we adjust it to a fixed value at the start of every cycle. The result of this clamp is that all alternans disappear from the model. Adjusting the adaptation variable at the onset of every beat effectively wipes the RyRs memory of the preceding calcium transient and removes the refractoriness from the model. This effect can also be achieved by setting the time constant of the adaptation variable to be less than that of the activation gate $\tau_a < \tau_o$. To see if removing the RyR refractoriness we set $\tau_a = 10$ ms and produce a new restiution curve, shown in Figure 10.1. From the new restitution curve, we see that alternans completely dissapear from the K2015 when the time constant of the adaptation gate is reduced, meaning the alternans in both region I and II are driven by RyR refractoriness from the preceding calcium transient.

10.1.2 Mechanisms of the K2014

Looking at the restitution curves shown in Figure 10.1, we see that the alternans exhibited by the K2014 are not removed when the adaptation gate is sped up, thus it is not a higher peak calcium in the calcium transient that causes a larger release. To understand the mechanism in this case, we run through the same candidates as we did for the K2015.

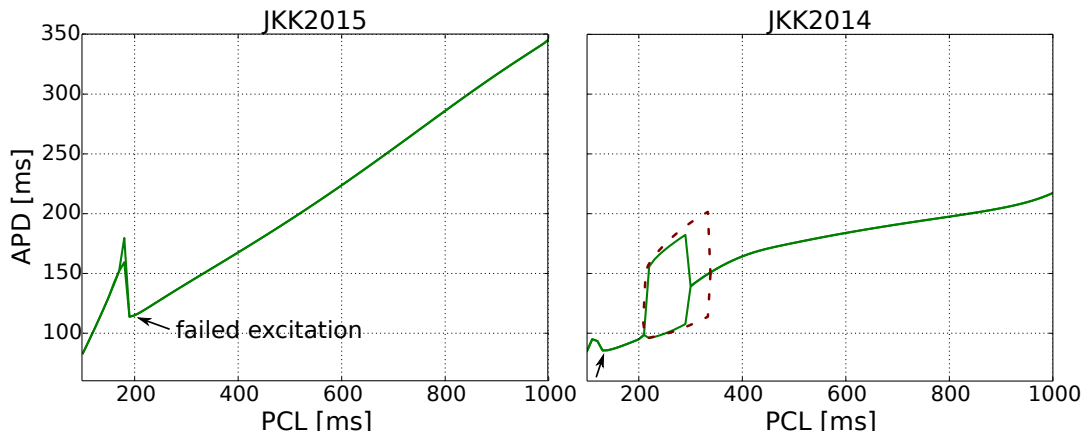


Figure 10.1: Restitution curves for the K2014 and K2015 when τ_{adapt} is set to 10 ms. Alternans completely disappear for the K2015 and are diminished for the K2014. The old alternans for the K2014 are shown in dashed red lines. **(K2015):** 2015 formulation of the model, alternans have completely disappeared. **(K2014):** Alternans have diminished, but are still present. The behavior for old results are shown in dashed red line and show that the area of alternans has reduced in width.

For the K2014 alternans, we only see electromechanical concordant alternans (Fig. 9.5a and b), meaning we have to consider the possibility of the alternans being voltage-driven. To see if they are voltage-driven, we clamp the membrane potential to follow the same action potential every cycle. This leads to a LTCC flux that is much more constant. The fluctuations in the release current are still present, though they move from a period-2 pattern to a period-3 pattern of no release ($\tilde{3}$ nmol), medium release ($\tilde{100}$ nmol), large release ($\tilde{220}$ nmol). From this we assume that intracellular calcium dynamics are also the root of alternans for the 2014 model variant.

Unlike for the K2015, the diastolic SR calcium load now fluctuates much from cycle to cycle (Fig. 9.5b). To see if alternating SR load is important for the alternans, we clamp the SR calcium concentration, which changes little in the behavior of the model. This leads us to conclude that RyR refractoriness is still the main root of alternans.

Looking at the RyR gating (Fig. 9.5g) shows the inactivation gate to be the main cause of the alternating release flux in this model variant. Inactivation of the RyR is caused by increased cytosolic calcium concentration, and so the alternating pattern is caused by the large cytosolic calcium each other beat. Adjusting the cytosolic calcium to be the same at the onset of every cycle does not remove the fluctuations in the inactivation, meaning it is not only the instantaneous dependence on $[\text{Ca}^{2+}]_i$ that is important, but also the history of the gate.

Adjusting the adaptation gate in addition to the cytosolic concentration does not affect this behavior, meaning it is the inactivation gate itself that is slow to adjust ($\tau_c = 13\text{--}74\text{ ms}$). Speeding up the inactivation gate in addition to the adaptation gate makes all alternans in the system disappear, even when nothing in the system is clamped. In summary: The alternans behavior of K2014 is also caused by RyR refractoriness. However, unlike the K2015, it is not the peak of the preceding calcium transient that is important, but rather the cytosolic calcium concentration the last 50 ms before the next cardiac cycle begins.

10.1.3 Model differences

From the comparisons of the calcium currents and transient of the two models shown in Figure 9.6 and 9.7, we observe that the K2014 generally has a larger L-type calcium current and subsequently a larger calcium release flux. In addition, both currents are shorter-lasting and have higher peaks in the K2014. The lower peak value of the L-type calcium channel in the K2015 means the action potential experiences a stronger early repolarization, leading to a clear notch in the action potential. To compensate for the lower peak, the L-type current typically lasts longer in the K2015, as seen best in 9.6a, where the total flux of the two models is about the same, even though the K2014 has almost double the peak current.

The difference between the calcium transients of the two variants is the smallest at a PCL of 1000 ms and only grows larger as the pacing rate grows faster. The K2014 doesn't change behavior considerably before reaching the very high pacing rate where alternans emerge. The L-type current has a very constant flux, reducing only a little as the PCL is lowered. For the K2015, the L-type calcium channel is reduced more continuously as the PCL is lowered, already seeing a considerable drop at a 700 ms PCL. This can be attributed to the low peak and long duration of the L-type current in the K2015 being more susceptible to a reduced APD. The large peak and short duration of the LTCC current of the K2014 means this model variant can create a large flux even for short APDs.

We have identified ryanodine refractoriness as the main mechanism of calcium-driven alternans in the models. Except for temperature scaling, the two formulations have the exact same implementation for the RyR. Recalling that the gating of the RyR is dependent solely on cytosolic calcium, the large differences in calcium behavior can be attributed to the hugely different calcium transients we have observed for the models.

From the ΔAPD_{90} heatmaps of the two model variants (Fig. 9.8a and b), we see the alternans behavior of the models is strongly dependent on the L-type calcium conductance. A higher L-type calcium conductance leads to a larger L-type current and thus higher cytosolic calcium concentration. Higher cytosolic

calcium concentration is expected to trigger largerer calcium release through graded release, but also to lead to increased refractoriness of the RyR. Different cytosolic calcium concentrations will also lead to changes in SR Ca^{2+} load. All of these changes, in combination, lead to the different alternans behavior observed.

Increasing the conductance of LTCC in the K2015 leads to a behavior more resembling the K2014, as does reducing the L-type conductance in the K2014. It is, however, clear from the Figures that the changes to the L-type conductance is not able to fully account for the different model behaviors. From the Hybrid model (Fig. 9.9), where the L-type formulation of the 2015 has been fully reverted, we see the behavior becomes a mixture of the K2014 and K2015 behaviors. By comparing Fig. 9.8a with 9.9 and then 9.9 to 9.8b we see the change in model behavior as all changes *except* for the L-type calcium is changed, and then how the L-type reformulation further changes the behavior. From this, we see that both the L-type reformulation and the remaining reformulations (see Section 8.1.3) both change the alternans behavior of the model. The change in alternans with the changing LTCC conductance of the hybrid model is closer to that found in the K2015, indicating that the reformulations other than the LTCC are important for alternans behavior in the models.

From our results, we conclude that the L-type reformulation is necessary, but not sufficient, to account for the differences in alternans behavior between the two model variants. We have seen that especially the L-type conductance is very impactful on the alternans behavior.

10.2 Fibroblast-Myocyte Coupling

From Figure 9.10, we see that fibroblast-myocyte coupling affects the virtual Koivumäki myocyte by increasing its resting membrane potential and reducing its action potential amplitude in all cases. This effect only gets stronger as the number of attached fibroblasts or coupling strength increase. In addition, the effects are pronounced for the active and passive II models. In addition to reduced APA, the early depolarization phase of the action potential has changed and the action potential therefore no longer displays a notch. We also observe that the myocyte fails to excite when it is coupled to three or four fibroblasts of type II, which was also reported by Maleckar et al, who observed failed excitation at three coupled fibroblasts. With the exception of the disappearance of the notch, these findings agree with the findings of [Maleckar et al., 2009a], where they looked at FMC using the Maleckar human atrial myocyte and fibroblast models. The M model for the hAM does not feature a notch, even when not coupled to fibroblasts.

Looking at the changes in resting membrane potential as a result of FMC (Fig 9.11(a)–(c)) revealed it to be mostly independent of coupling strength. The RMP increases monotonically with the number of fibroblasts. For the type-I fibroblasts, the RMP increases close to linearly, while for the type-II models there was a significant jump when the RMP became close to -60 mV and moving for two to three fibroblasts. Looking at the action potentials corresponding to these data points (Fig. 9.10(e)–(h), p. 118) reveals that this is the point where the myocyte fails to excite and indicates a significant change in the myocyte electrophysiology. To understand why the failure to excite occurs at roughly -60 mV, recall the steady-state values of the activation of the sodium current (Fig 8.3 on page 102), where we see that the sodium current has become close to completely unavailable at such high membrane potentials. This is seen in the measured sodium currents (Fig 9.11(c)–(k)), where availability of the sodium channels decreases significantly as the RMP approaches and crosses -60 mV.

Comparing the changes in RMP to values reported in computational studies of FMC in the literature we find these are comparable for atrial myocytes, while those reported for ventricular myocytes are much lower. For example both [Xie et al., 2009] and [MacCannell et al., 2007], who looked at ventricular myocytes, report that FMC has little impact on the myocyte RMP. This can be explained by the ventricular myocytes being larger and therefore having a larger capacitance. MacCannell et al looks at myocytes with a membrane capacitance of 185 pF, while the atrial myocytes in our study are only 50 pF. In both cases, the fibroblast capacitance is 6.3 pF.

The depolarized RMP leads to reduced sodium current in the model (Fig. 9.11) which we find has a strong impact on the myocyte excitability in the terms of maximum upstroke velocity and action potential amplitude, both of which are important for conduction velocity in tissue. We found the maximum upstroke velocity and APA could both be predicted with high accuracy from the measured myocyte RMP alone when under a critical threshold (Fig. 9.12). For RMP below -60 mV, linear regression had $R^2 > 0.95$ for all cases. Above this threshold the behavior changes drastically as the myocyte fails to excite, and so both the upstroke velocity and APA are only dependent on the external stimulus current.

In addition to the effects of depolarized RMP, we expect the fibroblasts to act as current sinks and thus represent an additional electrotonic load during the upstroke of the myocyte. This effect is seen when we compare the results to the control case where RMP is depolarized through increased extracellular potassium concentration (Fig. 9.13). In all six panels, the measured values lie close, but slightly below, those predicted from the control myocyte. This discrepancy can be attributed to the electrotonic load from the coupled fibroblasts, which will also lower upstroke velocity and APA due to an outward gap junction in the myocyte during the upstroke of the AP. We have found that the magnitude

of depolarization of the RMP is independent of the coupling strength, but comparing (a), (c) and (e), reveals that the electrotonic load increases with coupling strength. However, the differences moving from weak to medium coupling are larger than moving from medium to strong coupling, indicating that the coupling is becoming “saturated” and further increasing the coupling strength has little impact. The same behavior of increased discrepancy from the control myocyte is seen when looking at panels (b), (d) and (e).

10.3 Limitations of the Work

The goal of this work was to implement the Koivumäki model and use it for *in silico* electrophysiology experiments, and this has been carried out. The experiments performed do, however, have several limitations.

For our studies of cardiac alternans, we explored how the Koivumäki model behaved under different pacing regimes and when alternans were exhibited. However, the Koivumäki model was not designed to study cardiac alternans and the behavior of the model with regards to alternans have not been constrained to experiment. This means the alternans behavior we found the model to exhibited was purely a feature of the model itself, and not necessarily physiologically accurate or meaningful. This study should therefore be seen only as an exploration into the model behavior itself, and not necessarily indicative of how a real myocyte behaves.

We have also only studied cardiac alternans in a single myocyte, not in tissue. It is not immediately clear how the single myocyte behavior affects the tendency of the Koivumäki model to produce spatially concordant or discordant alternans.

When extending the Koivumäki model to include myocyte-fibroblast coupling, we only look at the systems of a single myocyte coupled to a number of identical fibroblasts. While we used several differing fibroblast models and different coupling strengths to account for some of the variety reported in the literature, we did not account for the possibility of the connected fibroblasts being different in a single simulation. Real FMC, if present *in situ*, might also include more complex situations such as: two-sided connections, expanded ECM, different myocyte-myocyte coupling, and so forth, none of which we have included in our simulations.

We also studied the effects of FMC only at a cycle length of 1000 ms, and it is not given that the results will be similar at faster pacing rates. This was not looked into due to time constraints.

10.4 Possibilities of Further Work

There are mainly three major directions of further work we might have pursued given more time.

The first is to see how the alternans behavior of the Koivumäki model could be manipulated by adjusting the parameters of the model. The goal of this work would be to produce a model of the human atrial myocyte that reliably produces stable alternans in a physiologically accurate manner. From our results, this seems to be possible through fine-tuning of the L-type calcium conductance and RyR parameters. An interesting use for such a model would be to study the effects of atrial fibrillation remodeling on alternans behavior, and see if the model could reproduce results such as [Narayan et al., 2011], where patients with chronic atrial fibrillation more easily exhibit alternans in response to rapid pacing.

The second is to go deeper into the effects of the FMC. A limitation of our work was only looking at the effects at cycle lengths of 1000 ms, and it would be interesting to note how that effects change at different pacing rates.

The third is to move to tissue-level simulations. It would be interesting to see how the inducibility of spatially discordant alternans in the Koivumäki model is affected by different pacing regimes and if there are big differences in the behavior between the 2014 and 2015 models. Moving from a single cell to a tissue model could be done using the monodomain equations, a continuum approach that can be solved using finite element methods. It would also be interesting to see the effects of FMC in tissue, as we could measure the effects of FMC on conduction velocity, ease of spiral wave induction and breakup and the effects of FMC on introducing spatially discordant alternans.

Chapter 11

Concluding Remarks

Much effort has been devoted to understanding the underlying mechanisms of atrial fibrillation, and it is still a very active area of research today. An important goal of atrial fibrillation research is to improve existing, and develop novel, treatment options. An crucial tool in this research are computational models. In this thesis we have looked at how atrial fibrillation is modeled today, with focus on models of a single atrial myocyte. While a mathematical model for a single cardiomyocyte is only a small piece of atrial fibrillation research, it is a very important piece, as it is the cardiomyocyte that is the functional unit of the cardiac tissue.

The main focus of this thesis has been on a specific model for the human atrial myocyte, formulated by Koivumäki et al. We have explored this model's ability to produce cardiac alternans, which are strongly linked to atrial fibrillation, as detailed in the literature review presented in Chapter 3. We also extended the model to include fibroblast-myocyte coupling, by combining it with the model for the human atrial fibroblast proposed by Maleckar et al. The long-term goal of this work is to help the further development and use of the Koivumäki atrial cell model.

An additional goal of this thesis was to provide an introduction to the topic of atrial fibrillation modeling for readers with no background in the field. A fairly lengthy introduction to cardiac electrophysiology, and a short review of our current understanding of atrial fibrillation, is therefore included. In addition we provide a detailed mathematical description of the Koivumäki cell model, as well as review of proposed fibroblast models found in the literature.

Our Contribution

We implemented the Koivumäki model in gotran, and solved it using computer-generated C-code interfaced through Python. After the implemented model was verified through test cases and comparisons to existing implementations, it was used to run *in silico* experiments.

We used our implementations of the Koivumäki model to see how both the 2014 and 2015 formulations of the model exhibit alternans. We observed large differences in the behavior of the two variants, who were both different from the alternans behavior of the 2011 variant as reported by Wilhelms et al. Both model variants exhibited alternans, with the K2015 showing alternans at longer cycle lengths than the K2014. For both model variants, we found the alternans to be calcium driven and caused by refractoriness of the ryanodine receptor release channel. We show the behavior results from the novel RyR formulation of the Koivumäki model.

We observe that the significant differences in alternans behavior between the 2014 and 2015 variants of the Koivumäki model can be attributed to different L-type formulations and a different maximal L-type calcium conductance. However, even when accounting for the L-type current reformulation, we observed clear differences between the models, indicating the other reformulations done to the 2015 model variant are also functionally impactful on alternans behavior.

We gave a review of four proposed fibroblast models in the literature. Using the Maleckar human atrial fibroblast model, we extended the Koivumäki model to include fibroblast-myocyte coupling. The extended model was used to study the effects of coupling 1–4 fibroblasts to a single Koivumäki myocyte.

We observed that FMC depolarized the myocyte resting potential leading to decreases availability of the sodium current. FMC reduced myocyte excitability by decreasing the upstroke velocity and amplitude of the action potential. These effects were seen to scale with the number of coupled fibroblasts and were more pronounced for the fibroblasts with the highest resting membrane potential. The decrease in upstroke velocity and action potential amplitude was found to scale linearly with the myocyte resting potential up until the point where the myocyte became unexcitable. We observed the depolarization of the RMP to be mostly independent of the coupling strength between the myocyte and fibroblasts. The effects of the FMC on upstroke velocity and APA could not be completely accounted for by the depolarized RMP and is instead attributed to the additional electrotonic load introduced by the fibroblasts. This effect was seen to scale with the coupling strength up until the point where the coupling strength became saturated.

Chapter 12

Bibliography

[American Heart Association, 2016] American Heart Association (2016). What are the symptoms of atrial fibrillation? <https://goo.gl/KXHs8l>. Accessed: 2016-02-19.

[Anderson et al., 1967] Anderson, R. M., Fritz, J. M., and O'Hare, J. E. (1967). The mechanical nature of the heart as a pump. *American heart journal*, 73:92–105.

[Beeler and Reuter, 1977] Beeler, G. W. and Reuter, H. (1977). Reconstruction of the action potential of ventricular myocardial fibres. *The Journal of Physiology*, 268:177–210.

[Camelliti et al., 2004] Camelliti, P., Green, C. R., LeGrice, I., and Kohl, P. (2004). Fibroblast network in rabbit sinoatrial node structural and functional identification of homogeneous and heterogeneous cell coupling. *Circulation Research*, 94:828–835.

[Campbell et al., 1988] Campbell, D., Giles, W., Hume, J., Noble, D., and Shiba, E. (1988). Reversal potential of the calcium current in bull-frog atrial myocytes. *The Journal of Physiology*, 403:267–286.

[Chudin et al., 1999] Chudin, E., Goldhaber, J., Garfinkel, A., Weiss, J., and Kogan, B. (1999). Intracellular Ca^{2+} dynamics and the stability of ventricular tachycardia. *Biophysical Journal*, 77:2930–2941.

[Courtemanche et al., 1998] Courtemanche, M., Ramirez, R. J., and Nattel, S. (1998). Ionic mechanisms underlying human atrial action potential properties: insights from a mathematical model. *American Journal of Physiology-Heart and Circulatory Physiology*, 275:H301–H321.

[Cox et al., 1991] Cox, J. L., Schuessler, R., D'Agostino Jr, H., Stone, C., Chang, B.-C., Cain, M., Corr, P., and Boineau, J. (1991). The surgical treatment of

- atrial fibrillation. III. Development of a definitive surgical procedure. *The Journal of Thoracic and Cardiovascular Surgery*, 101:569–583.
- [Creative Commons, 2007] Creative Commons (2007). Creative commons 3.0 unreported. <http://creativecommons.org/licenses/by/3.0/>. Last retrieved 2016-04-25.
- [Dössel et al., 2012] Dössel, O., Krueger, M. W., Weber, F. M., Wilhelms, M., and Seemann, G. (2012). Computational modeling of the human atrial anatomy and electrophysiology. *Medical & Biological Engineering & Computing*, 50:773–799.
- [Fenton et al., 2008] Fenton, F. H., Cherry, E. M., and Glass, L. (2008). Cardiac arrhythmia. *Scholarpedia*, 3:1665.
- [Frisk et al., 2014] Frisk, M., Koivumäki, J. T., Norseng, P. A., Maleckar, M. M., Sejersted, O. M., and Louch, W. E. (2014). Variable t-tubule organization and Ca^{2+} homeostasis across the atria. *American Journal of Physiology-Heart and Circulatory Physiology*, 307:H609–H620.
- [Gaeta and Christini, 2012] Gaeta, S. A. and Christini, D. J. (2012). Non-linear dynamics of cardiac alternans: subcellular to tissue-level mechanisms of arrhythmia. *Frontiers in Physiology*, 3.
- [Goldsmith et al., 2004] Goldsmith, E. C., Hoffman, A., Morales, M. O., Potts, J. D., Price, R. L., McFadden, A., Rice, M., and Borg, T. K. (2004). Organization of fibroblasts in the heart. *Developmental Dynamics*, 230:787–794.
- [Grandi et al., 2011] Grandi, E., Pandit, S. V., Voigt, N., Workman, A. J., Dobrev, D., Jalife, J., and Bers, D. M. (2011). Human atrial action potential and Ca^{2+} model sinus rhythm and chronic atrial fibrillation. *Circulation Research*, 109:1055–1066.
- [Hodgkin and Huxley, 1952] Hodgkin, A. L. and Huxley, A. F. (1952). A quantitative description of membrane current and its application to conduction and excitation in nerve. *The Journal of Physiology*, 117:500–544.
- [Hund et al., 2001] Hund, T. J., Kucera, J. P., Otani, N. F., and Rudy, Y. (2001). Ionic charge conservation and long-term steady state in the Luo–Rudy dynamic cell model. *Biophysical Journal*, 81:3324–3331.
- [Jacquemet and Henriquez, 2007] Jacquemet, V. and Henriquez, C. S. (2007). Modelling cardiac fibroblasts: interactions with myocytes and their impact on impulse propagation. *Europace*, 9:vi29–vi37.
- [Katz, 2010] Katz, A. M. (2010). *Physiology of the Heart*. Lippincott Williams & Wilkins.

- [Kohl and Camelliti, 2007] Kohl, P. and Camelliti, P. (2007). Cardiac myocyte–nonmyocyte electrotonic coupling: implications for ventricular arrhythmogenesis. *Heart Rhythm*, 4:233–235.
- [Koivumäki et al., 2011] Koivumäki, J. T., Korhonen, T., and Tavi, P. (2011). Impact of sarcoplasmic reticulum calcium release on calcium dynamics and action potential morphology in human atrial myocytes: A computational study. *PLOS Computational Biology*, 7:e1001067.
- [Koivumäki et al., 2014] Koivumäki, J. T., Seemann, G., Maleckar, M. M., and Tavi, P. (2014). In silico screening of the key cellular remodeling targets in chronic atrial fibrillation. *PLOS Computational Biology*, 10:e1003620.
- [MacCannell et al., 2007] MacCannell, K. A., Bazzazi, H., Chilton, L., Shibukawa, Y., Clark, R. B., and Giles, W. R. (2007). A mathematical model of electrotonic interactions between ventricular myocytes and fibroblasts. *Bioophysical Journal*, 92:4121–4132.
- [Maleckar et al., 2009a] Maleckar, M. M., Greenstein, J. L., Giles, W. R., and Trayanova, N. A. (2009a). Electrotonic coupling between human atrial myocytes and fibroblasts alters myocyte excitability and repolarization. *Biophysical Journal*, 97:2179–2190.
- [Maleckar et al., 2009b] Maleckar, M. M., Greenstein, J. L., Giles, W. R., and Trayanova, N. A. (2009b). K⁺ current changes account for the rate dependence of the action potential in the human atrial myocyte. *American Journal of Physiology-Heart and Circulatory Physiology*, 297:H1398–H1410.
- [Naghavi et al., 2015] Naghavi, M., Wang, H., Lozano, R., Davis, A., Liang, X., Zhou, M., Vollset, S. E., Ozgoren, A. A., Abdalla, S., Abd-Allah, F., et al. (2015). Global, regional, and national age-sex specific all-cause and cause-specific mortality for 240 causes of death, 1990–2013: a systematic analysis for the global burden of disease study 2013. *Lancet*, 385:117–171.
- [Narayan et al., 2011] Narayan, S. M., Franz, M. R., Clopton, P., Pruvot, E. J., and Krummen, D. E. (2011). Repolarization alternans reveals vulnerability to human atrial fibrillation. *Circulation*, 123:2922–2930.
- [Nguyen et al., 2014] Nguyen, T. P., Qu, Z., and Weiss, J. N. (2014). Cardiac fibrosis and arrhythmogenesis: The road to repair is paved with perils. *Journal of Molecular and Cellular Cardiology*, 70:83 – 91.
- [Noble, 1962] Noble, D. (1962). A modification of the Hodgkin-Huxley equations applicable to Purkinje fibre action and pacemaker potentials. *The Journal of Physiology*, 160:317–352.

- [Nolasco and Dahlen, 1968] Nolasco, J. and Dahlen, R. W. (1968). A graphic method for the study of alternation in cardiac action potentials. *Journal of Applied Physiology*, 25:191–196.
- [Nygren et al., 1998] Nygren, A., Fiset, C., Firek, L., Clark, J., Lindblad, D., Clark, R., and Giles, W. (1998). Mathematical model of an adult human atrial cell the role of K^+ currents in repolarization. *Circulation Research*, 82:63–81.
- [Picht et al., 2006] Picht, E., DeSantiago, J., Blatter, L. A., and Bers, D. M. (2006). Cardiac alternans do not rely on diastolic sarcoplasmic reticulum calcium content fluctuations. *Circulation Research*, 99:740–748.
- [Prasad et al., 2003] Prasad, S. M., Maniar, H. S., Camillo, C. J., Schuessler, R. B., Boineau, J. P., Sundt, T. M., Cox, J. L., and Damiano, R. J. (2003). The Cox maze III procedure for atrial fibrillation: long-term efficacy in patients undergoing lone versus concomitant procedures. *The Journal of Thoracic and Cardiovascular Surgery*, 126:1822–1827.
- [Priebe and Beuckelmann, 1998] Priebe, L. and Beuckelmann, D. J. (1998). Simulation study of cellular electric properties in heart failure. *Circulation Research*, 82:1206–1223.
- [Qu et al., 2000] Qu, Z., Garfinkel, A., Chen, P.-S., and Weiss, J. N. (2000). Mechanisms of discordant alternans and induction of reentry in simulated cardiac tissue. *Circulation*, 102:1664–1670.
- [Qu et al., 2013] Qu, Z., Nivala, M., and Weiss, J. N. (2013). Calcium alternans in cardiac myocytes: Order from disorder. *Journal of molecular and cellular cardiology*, 58:100–109.
- [Richards et al., 2011] Richards, M. A., Clarke, J. D., Saravanan, P., Voigt, N., Dobrev, D., Eisner, D. A., Trafford, A. W., and Dibb, K. M. (2011). Transverse tubules are a common feature in large mammalian atrial myocytes including human. *American Journal of Physiology-Heart and Circulatory Physiology*, 301:H1996–H2005.
- [Rook et al., 1992] Rook, M., Van Ginneken, A., de Jonge, B., El Aoumari, A., Gros, D., and Jongsma, H. (1992). Differences in gap junction channels between cardiac myocytes, fibroblasts, and heterologous pairs. *American Journal of Physiology-Cell Physiology*, 263:C959–C977.
- [Rush and Larsen, 1978] Rush, S. and Larsen, H. (1978). A practical algorithm for solving dynamic membrane equations. *IEEE Transactions on Biomedical Engineering*, 25:389–392.

- [Sachse et al., 2008] Sachse, F., Moreno, A., and Abildskov, J. A. (2008). Electrophysiological modeling of fibroblasts and their interaction with myocytes. *Annals of Biomedical Engineering*, 36:41–56.
- [Shuster, 1997] Shuster, E. (1997). Fifty years later: the significance of the nuremberg code. *New England Journal of Medicine*, 337:1436–1440.
- [Sterratt et al., 2011] Sterratt, D., Graham, B., Gillies, A., and Willshaw, D. (2011). *Principles of computational modelling in neuroscience*. Cambridge University Press.
- [Süli and Mayers, 2003] Süli, E. and Mayers, D. F. (2003). *An introduction to numerical analysis*. Cambridge University Press.
- [ten Tusscher et al., 2004] ten Tusscher, K., Noble, D., Noble, P., and Panfilov, A. (2004). A model for human ventricular tissue. *American Journal of Physiology-Heart and Circulatory Physiology*, 286:H1573–H1589.
- [ten Tusscher and Panfilov, 2006] ten Tusscher, K. H. and Panfilov, A. V. (2006). Alternans and spiral breakup in a human ventricular tissue model. *American Journal of Physiology-Heart and Circulatory Physiology*, 291:H1088–H1100.
- [Trayanova, 2014] Trayanova, N. A. (2014). Mathematical approaches to understanding and imaging atrial fibrillation significance for mechanisms and management. *Circulation Research*, 114:1516–1531.
- [Valdivia, 2015] Valdivia, H. H. (2015). Mechanisms of cardiac alternans in atrial cells intracellular Ca^{2+} disturbances lead the way. *Circulation Research*, 116:778–780.
- [Vasquez et al., 2009] Vasquez, C., Feig, J. E., Mohandas, P., Fisher, E. A., and Morley, G. E. (2009). Arrhythmogenic potential of activated fibroblasts. *Biophysical Journal*, 96:562a–563a.
- [Wagner and Keizer, 1994] Wagner, J. and Keizer, J. (1994). Effects of rapid buffers on Ca^{2+} diffusion and Ca^{2+} oscillations. *Biophysical Journal*, 67:447.
- [Weerasooriya et al., 2011] Weerasooriya, R., Khairy, P., Litalien, J., Macle, L., Hocini, M., Sacher, F., Lellouche, N., Knecht, S., Wright, M., Nault, I., et al. (2011). Catheter ablation for atrial fibrillation: are results maintained at 5 years of follow-up? *Journal of the American College of Cardiology*, 57:160–166.
- [Weiss et al., 2006] Weiss, J. N., Karma, A., Shiferaw, Y., Chen, P.-S., Garfinkel, A., and Qu, Z. (2006). From pulsus to pulseless the saga of cardiac alternans. *Circulation Research*, 98:1244–1253.

- [Wijffels et al., 1995] Wijffels, M. C., Kirchhof, C. J., Dorland, R., and Allessie, M. A. (1995). Atrial fibrillation begets atrial fibrillation a study in awake chronically instrumented goats. *Circulation*, 92:1954–1968.
- [Wilhelms et al., 2012] Wilhelms, M., Hettmann, H., Maleckar, M. M., Koivumäki, J. T., Dössel, O., and Seemann, G. (2012). Benchmarking electrophysiological models of human atrial myocytes. *Frontiers in Physiology*, 3.
- [Xie et al., 2009] Xie, Y., Garfinkel, A., Weiss, J. N., and Qu, Z. (2009). Cardiac alternans induced by fibroblast-myocyte coupling: mechanistic insights from computational models. *American Journal of Physiology - Heart and Circulatory Physiology*, 297:H775–H784.
- [Zipes and Jalife, 2000] Zipes, D. P. and Jalife, J. (2000). *Cardiac electrophysiology: from cell to bedside*. Philadelphia: WB Saunders Co.
- [Zoni-Berisso et al., 2014] Zoni-Berisso, M., Lercari, F., Carazza, T., Domenicucci, S., et al. (2014). Epidemiology of atrial fibrillation: European perspective. *Journal of Clinical Epidemiology*, 6:e220.
- [Zorn-Pauly et al., 2004] Zorn-Pauly, K., Schaffer, P., Pelzmann, B., Lang, P., Mächler, H., Rigler, B., and Koidl, B. (2004). I_f in left human atrium: a potential contributor to atrial ectopy. *Cardiovascular Research*, 64:250–259.